DEVELOPMENT OF SURFACE-SPECIFIC TWO DIMENSIONAL VIBRATIONAL SPECTROSCOPY AND ITS APPLICATION TO HETEROGENEOUS CATALYSIS

A Dissertation

Presented to the Faculty of the Graduate School

of Cornell University

In Partial Fulfillment of the Requirements for the Degree of

Doctor of Philosophy

by

Heather Vanselous

August 2017

DEVELOPMENT OF SURFACE-SPECIFIC TWO DIMENSIONAL VIBRATIONAL SPECTROSCOPY AND ITS APPLICATION TO HETEROGENEOUS CATALYSIS

Heather Vanselous, Ph. D.

Cornell University 2017

Liquid-solid and liquid-gas interfaces play a key role in numerous biological, chemical, and physical processes. Understanding the molecular environment and behavior in these systems is particularly challenging due to the few molecules involved. Vibrational sum-frequency generation (SFG) spectroscopy is a unique tool used to examine the structure and ultrafast dynamics of molecules at interfaces by capturing their vibrational motions. Additional information on the interfacial matrix can be obtained through more complex experiments- namely, the average molecular orientation can be determined via heterodyne detection, and inter and intramolecular coupling and spectral diffusion dynamics can be obtained by interferometric 2D SFG. This dissertation describes the development of these techniques and their application to a metal carbonyl based CO_2 reduction catalyst on nanocrystalline and single crystal TiO_2 to study the impact that immobilization has on the molecular structure and vibrational properties which influence the catalytic process.

BIOGRAPHICAL SKETCH

Heather Vanselous earned a Bachelor of Science degree in Chemistry from Temple University is 2011 where she began a project on in situ vibrational sum frequency generation (SFG) spectroscopy of electrolyte/electrode interfaces for modeling fuel cells in the group of Professor Eric Borguet. Meanwhile, as part of the Student Career Experience program at the US Department of Agriculture, she optimized catalyst and reaction conditions for converting waste greases to high value added products such as biodiesel. After joining the Petersen group for her PhD program, she worked on expanding the capabilities of SFG experiments while gaining fundamental molecular insight on the structure-property relationship of catalytic CO_2 reduction systems.

ACKNOWLEDGMENTS

Thank you to my colleagues in the Petersen group, both past and present, for all of their support both in the lab and at the Dairy Bar. To my committee members, Dr. John Marohn and Dr. Nandini Ananth, thank you for your time and insight. To my advisor, Dr. Poul Petersen, for always being an optimist and a constant source of support and guidance. And finally to my friends and family, for their love and support even in my decision to remain in the Finger Lakes region. This dissertation would not have been possible without the loyalty, support, and encouragement whenever I needed it most from my husband, Stephen Barrett, and also from my cats.

The research presented in this dissertation was supported by the Young Investigator Award from the Arnold and Mabel Beckman Foundation and the NSF CAREER grant: CHE-1151079.

TABLE OF CONTENTS

LIST OF FIGURES

LIST OF TABLES

CHAPTER 1

INTRODUCTION AND BACKGROUND

1.1 Motivation

1.1.1 CO_2 Reduction Catalysis – Closing the Carbon Cycle

Subtle changes in Earth's atmospheric composition, sea level, and surface temperature could alter the ecosystem to be uninhabitable for the diversity of life currently existing here. Global warming has the potential to alter every aspect of the climate. A major contributor to global warming is an increased atmospheric concentration of the greenhouse gas CO_2, which has a long-term impact on the climate.[1-6] Carbon and oxygen, sequestered over millions of years in the earth's crust, have been released into the atmosphere as CO_2 by humans over the last 150 years. Gas trapped in ice sheets provides a window into the Earth's past atmospheric composition. Throughout the last 800,000 years, CO_2 concentrations have remained between 150 and 300 parts per million by volume (ppmv).[7] However, since the industrial revolution in the mid 1700's, humans have extracted and burned fossil fuels, generating an unprecedented growth in the atmospheric CO_2 content (Figure 1.1). As a result of the extensive use of fossil fuels to power our homes, cars, businesses, and manufacturing processes, the atmospheric CO_2 concentration is still on the rise and is currently over 400 ppmv.

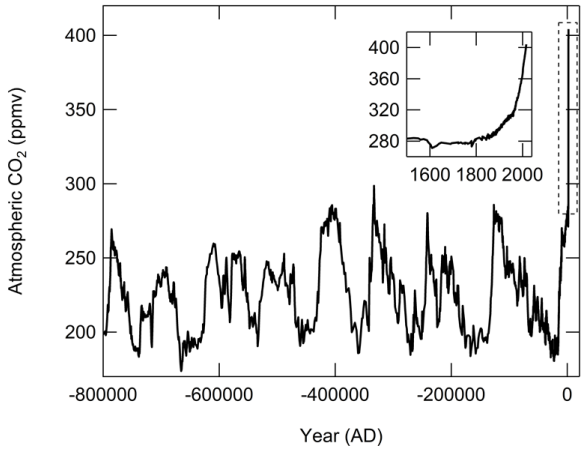

Figure 1.1 Atmospheric CO_2 concentrations measured through ice cores. Inset shows recent history. Data obtained from Ref. 7.

The plight of rising atmospheric CO_2 concentrations and subsequent global climate change could be solved by closing the carbon cycle, forming a perpetual loop where CO_2 in the atmosphere is collected and converted into fuel before it is burned and released again. Since this chemical reaction requires an input of energy, sustainable solutions would involve the use of renewable alternative energy technologies. Of the various types of renewable energy sources currently in use – including solar, wind, geothermal, biofuels, and hydropower – solar energy is far and above the most abundant, with enough energy reaching the Earth's surface in one hour to satisfy the world's energy needs for a year.[8,9] Solar energy can be used to reduce CO_2 either photocatalytically (using solar photons directly) or electrocatalytically (using electricity generated from photons with solar cells). Potential products of this reduction reaction include carbon monoxide, formic acid, methanol, and methane, each with progressively higher energy barriers.[10]

1.1.2 Heterogeneous Photocatalysis

One example of a CO_2 reduction reaction that has been studied is the reduction of CO_2 to CO and water:

$$CO_2 + 2H^+ + 2e^- \rightleftharpoons CO + H_2O$$

The "gold standard" homogeneous catalyst for this reaction has been a rhenium based catalyst, Re(bipyridine)$(CO)_3Cl$ (abbreviated $Re(CO)_3$), which has strong visible-light absorption and high selectivity for CO as a product.[10,11] This complex offers tunablility through changes to the ligand structure and acts as both photosensitizer and catalyst. The general proposed mechanism for this reaction involves light absorption by the catalyst, generating a metal-to-ligand charge transfer (MLCT) excited state.[11] A sacrificial donor, such as triethanolamine, reduces the catalyst which can then release a labile halogen ligand. CO_2 then coordinates at the empty ligand site and is released as CO and H_2O as the halogen re-coordinates and regenerates the initial catalyst.

As a homogeneous catalyst, $Re(CO)_3$ has limited solubility, and catalyst recovery and re-use is a concern. Immobilization through covalent binding to a high surface area support increases the number of active sites in solution and allows the catalyst to be removed via filtration or centrifugation and reused, thereby greatly increasing the economics of the reaction.

To create a heterogeneous catalyst, this complex has been immobilized in a number of different ways, including electropolymerization onto mesoporous TiO_2,[12] covalent attachment to mesoporous silica through sulfur linkers,[13] and covalent

binding to silica nanoparticles through amide groups.[14] All of these systems exhibited increased overall device performance as a result of the increased number of catalysts per unit volume as compared to in solution.

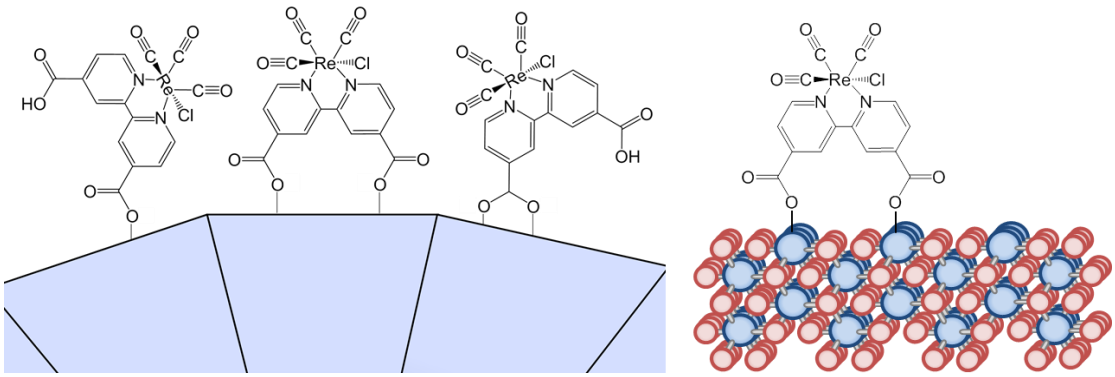

Figure 1.2 Schematic representations of $Re(CO)_3$ catalyst bound to different forms of TiO_2: a nanoparticle, left, and a single crystal surface, right.

Covalent binding to a surface can change the chemical reactivity of the catalyst. One particularly interesting study found that immobilizing these rhenium complexes on high surface area metal oxide nanoparticles, shown schematically in Figure 1.2, increases the molecular efficiency of the reaction.[15] Moreover, the particular choice of metal oxide made a large difference in the overall turnover number (TON_{CO}), given by the number of molecules of CO generated per molecule of catalyst once the system stops generating CO. The interaction with TiO_2 was especially favorable, with an overall enhancement of a factor of 8 (Figure 1.3). These measurements were performed with a constant catalyst loading as measured by UV-Vis absorption, which indicates that the enhanced efficiency observed on TiO_2 is not only from an increase in catalyst per unit volume, but also a result of some other

change in the catalyst upon immobilization. One such change is the catalyst is stabilized through binding to TiO_2 as the lifetime of the catalytically active reduced state is increased.[15]

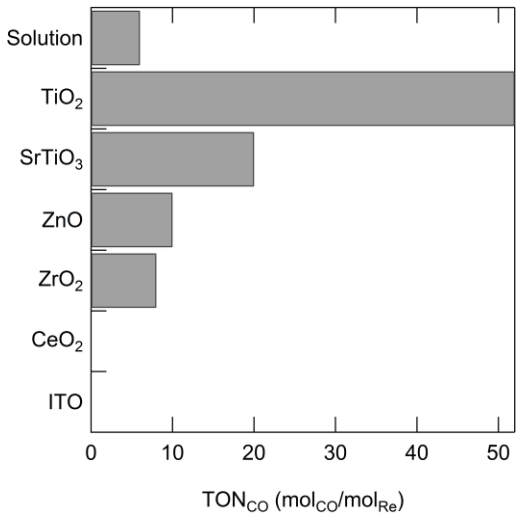

Figure 1.3 TON_{CO} for rhenium based catalyst in solution compared to the solvated catalyst immobilized on various metal oxide nanoparticles. Data is from Ref. 15.

Time-resolved IR spectroscopic studies have been performed to examine the role of TiO_2 in the reaction mechanism.[16] Transient mid-infrared spectroscopy was used to monitor the metal carbonyl vibrational modes, which report on the oxidation state of the rhenium center, and the electrons entering and exiting the conduction band of TiO_2, which display a broad absorption in the IR. The TiO_2 nanoparticles were found to act as an electron sink, holding electrons while the rhenium center binds and reduces CO_2, then act as the electron source to regenerate the catalyst.[16] Since the interaction between the catalyst and TiO_2 influences the CO_2 reduction reaction, a thorough understanding of that interaction is needed in order to predict and optimize

the CO_2 reduction system. The degree of electronic coupling between the catalyst and TiO_2 and the binding geometry and intermolecular coupling of the catalyst can influence the reaction and can be better understood through vibrational spectroscopy.

1.1.3 Advanced Materials – Single Crystal TiO_2

It is now well known that chemical reactions, including photodegradation and photoelectrochemistry, are facet-dependent on TiO_2 surfaces.[17-21] Moreover, high-surface-area TiO_2 substrates, such as nanotubes, are now being synthesized with controlled single-crystal facets, which could lead to significantly improved device performance.[22-30] To obtain a detailed understanding of the TiO_2-catalyst interaction, it is beneficial to simplify this highly complex and heterogeneous system by first studying single crystal TiO_2 surfaces. A schematic comparison of potentially different binding geometries is shown in Figure 1.2. However, understanding the molecular interaction at single crystal TiO_2 surfaces presents a challenge due to the small number of adsorbates in a monolayer.

1.2 Experimental Approach – Sum Frequency Generation Spectroscopy

Understanding the sensitized single-crystal system requires a method which has sub-monolayer sensitivity and can probe molecular properties that would change as a function of the subtle surface variations between different single crystal TiO_2 facets. The metal CO vibrational modes on the catalysts are very sensitive to the local

electronic environment (including the oxidation state of the metal center), are spectrally separated from most other vibrational modes, and tend to have high molar absorptivities.[31-37] However, conventional vibrational methods, such as Fourier Transform IR and Raman spectroscopies, are typically not sensitive enough to detect single monolayers. Additionally, in order to study the dynamics at the surface, a technique which has the time resolution on the order of the vibrational motion (femtosecond and picosecond timescales) is required. Therefore, one would need a surface-specific and ultrafast vibrational spectroscopic technique. As described in Chapter 2, Sum-Frequency Generation (SFG) spectroscopy satisfies both of these requirements. While this technique probes the surface vibrational spectrum, in order to gain insight into the molecular orientation, vibrational dynamics, heterogeneity, and inter and intramolecular vibrational coupling, experimental advancements must be made in the field of SFG. This dissertation focuses on the development and incorporation of these experimental advances and the information gained on the heterogeneous CO_2 reduction system.

1.3 General Outline of Dissertation

Conventional homodyne-detected SFG spectroscopy has proven invaluable in studying both the structure and dynamics of molecules at interfaces in biological, electrochemical, and atmospheric environments. The technique's interface specificity is a defining quality, allowing for condensed phase measurements which probe only the first few molecular layers. The theory of SFG spectroscopy is presented in Chapter

2 in addition to experimental details relating to the advanced forms of SFG developed through this dissertation.

There is still a great deal of information that can be gained regarding, and is indeed critical for the understanding of, interfacial chemistry. For instance, interfacial molecular orientation plays a role in the steric effects which influence chemical reactions that occur at a given interface. In order to extract orientational information from conventional SFG measurements, a spectral lineshape is used, often in the form of a Lorentzian. Lorentzian lineshapes work well in cases of individual discrete vibrational modes but not for broad inhomogeneous vibrational bands such as the OH stretch region of water. In principle, inhomogeneous broadening can be fit to a sum of a distribution of many Lorentzian peaks, but it is not well described by a few discrete Lorentzian features. Particularly in the condensed phase, this is an unlikely scenario. Heterodyne-detection (HD), which was first developed for two-dimensional infrared (2D IR) experiments, has been used by a select few research groups to extract the pure absorptive spectrum through interference with an external field. Chapter 3 describes our experimental advances in this field which allow HD SFG at any interface, in any polarization combination, and in an experimental geometry that is robust, easy to implement, and phase stable for days.

Additional information on homogeneous and inhomogeneous broadening and inter and intramolecular couplings can be obtained in the bulk with 2D IR spectroscopy. Modern versions of this technique rely on heterodyne detection and two interfering excitation pulses. SFG experiments performed to gain this level of

understanding for molecules at interfaces have either involved external HD with non-interfering excitation pulses (scanning narrowband IR pump) that have inferior temporal resolution or internal HD (molecules tethered to a gold substrate) with interfering excitation pulses which limits the systems which can be studies to dry molecules that bind to a gold surface. Chapter 4 builds on the experimental advances in Chapter 3 to describe the first 2D SFG experiment performed with external HD and interfering excitation pulses. Studying $Re(CO)_3$ on TiO_2 nanoparticles reveal a large static structural heterogeneity at the interface.

Chapter 5 describes 2D SFG experiments of $Re(CO)_3$ on single crystal rutile and anatase TiO_2 surfaces and compares the results to the nanocrystalline experiments. A striking difference in the vibrational relaxation dynamics and intermolecular vibrational coupling in the two types of environments is observed, and the potential relevance of these differences on the photocatalytic $Re(CO)_3$-TiO_2 system is discussed.

While 2D IR experiments may have the sensitivity to study single monolayers with very large oscillator strengths,[35] such as metal carbonyls, 2D IR cannot differentiate bulk condensed phase molecules from those at the surface. Rather, surface-specific 2D SFG must be used to probe only the interfacial molecules. An exemplary system for this technique is water at an interface. Chapter 6 presents interferometric 2D SFG spectra of water in contact with a hydrophobic self-assembled monolayer. This study reveals a significant difference between interfacial water structure and vibrational dynamics at a solid hydrophobic interface compared to the

water-air interface. Previous scanning IR pump – SFG probe experiments and theoretical work described water at the hydrophobic air-water surface as having significantly slower vibrational dynamics when compared to bulk water. Our interferometric 2D SFG results show that the vibrational dynamics of water at a condensed phase hydrophobic surface are faster than in the bulk.

The experimental advances presented in this dissertation open up the SFG technique to a wider range of experimental information and systems that can be studied. Now, interfacial molecular orientation, vibrational relaxation dynamics, inter and intramolecular vibrational coupling, and vibrational heterogeneity can be studied at buried solvated interfaces in any polarization combination. Chapter 7 summarizes the findings of this dissertation and outlines potential future extensions.

1.4 References

(1) Solomon, S.; Plattner, G.-K.; Knutti, R.; Friedlingstein, P. Irreversible Climate Change due to Carbon Dioxide Emissions. *Proc. Natl. Acad. Sci. U.S.A.* **2009**, *106*, 1704–1709.

(2) Rosenzweig, C.; Parry, M. L. Potential Impact of Climate Change on World Food Supply. *Nature* **1994**, *367*, 133–138.

(3) Feely, R. A.; Sabine, C. L.; Lee, K.; Berelson, W.; Kleypas, J.; Fabry, V. J.; Millero, F. J. Impact of Anthropogenic CO_2 on the $CaCO_3$ System in the Oceans. *Science.* **2004**, *305*, 362–366.

(4) Orr, J. C.; Fabry, V. J.; Aumont, O.; Bopp, L.; Doney, S. C.; Feely, R. A.;

Gnanadesikan, A.; Gruber, N.; Ishida, A.; Joos, F.; et al. Anthropogenic Ocean Acidification over the Twenty-First Century and Its Impact on Calcifying Organisms. *Nature* **2005**, *437*, 681–686.

(5) Reddy, A. R.; Rasineni, G. K.; Raghavendra, A. S. The Impact of Global Elevated CO_2 Concentration on Photosynthesis and Plant Productivity. *Curr. Sci.* **2010**, *99*, 46–57.

(6) Kerr, R. A. Global Warming. How Urgent Is Climate Change? *Science.* **2007**, *318*, 1230–1231.

(7) Bereiter, B.; Eggleston, S.; Schmitt, J.; Nehrbass-Ahles, C.; Stocker, T. F.; Fischer, H.; Kipfstuhl, S.; Chappellaz, J. Antarctic Ice Cores Revised 800KYr CO_2 Data http://ncdc.noaa.gov/paleo/study/17975 (accessed Jan 1, 2015).

(8) Service, R. F. Is It Time to Shoot for the Sun? *Science.* **2005**, *309*, 548–551.

(9) Lewis, N. S.; Nocera, D. G. Powering the Planet: Chemical Challenges in Solar Energy Utilization. *Proc. Natl. Acad. Sci. U.S.A.* **2006**, *103*, 15729–15735.

(10) Kumar, B.; Llorente, M.; Froehlich, J.; Dang, T.; Sathrum, A.; Kubiak, C. P. Photochemical and Photoelectrochemical Reduction of CO_2. *Annu. Rev. Phys. Chem.* **2012**, *63*, 541–569.

(11) Lehn, J.-M.; Ziessel, R. Photochemical Generation of Carbon Monoxide and Hydrogen by Reduction of Carbon Dioxide and Water under Visible Light Irradiation. *Proc. Natl. Acad. Sci. U.S.A.* **1982**, *79*, 701–704.

(12) Cecchet, F.; Alebbi, M.; Bignozzi, C. A.; Paolucci, F. Efficiency Enhancement of the Electrocatalytic Reduction of CO_2: Fac-[Re(v-bpy)$(CO)_3$Cl]

Electropolymerized onto Mesoporous TiO_2 Electrodes. *Inorganica Chim. Acta* **2006**, *359*, 3871–3874.

(13) Takeda, H.; Ohashi, M.; Tani, T.; Ishitani, O.; Inagaki, S. Enhanced Photocatalysis of Rhenium(I) Complex by Light-Harvesting Periodic Mesoporous Organosilica. *Inorg. Chem.* **2010**, *49*, 4554–4559.

(14) Liu, C.; Dubois, K.; Louis, M.; Vorushilov, A.; Li, G. Photocatalytic CO_2 Reduction and Surface Immobilization of a Tricarbonyl Re (I) Compound Modified with Amide Groups. *ACS Catal.* **2013**, *3*, 655-662.

(15) Windle, C. D.; Pastor, E.; Reynal, A.; Whitwood, A. C.; Vaynzof, Y.; Durrant, J. R.; Perutz, R. N.; Reisner, E. Improving the Photocatalytic Reduction of CO_2 to CO through Immobilisation of a Molecular Re Catalyst on TiO_2. *Chemistry* **2015**, *21*, 3746–3754.

(16) Abdellah, M.; El-Zohry, A. M.; Antila, L. J.; Windle, C. D.; Reisner, E.; Hammarström, L. Time-Resolved IR Spectroscopy Reveals a Mechanism with TiO_2 as a Reversible Electron Acceptor in a TiO_2 −Re Catalyst System for CO_2 Photoreduction. *J. Am. Chem. Soc.* **2017**, *139*, 1226–1232.

(17) Fujishima, A.; Zhang, X.; Tryk, D. A. TiO_2 Photocatalysis and Related Surface Phenomena. *Surf. Sci. Rep.* **2008**, *63*, 515–582.

(18) Spitler, M. T.; Parkinson, B. A. Dye Sensitization of Single Crystal Semiconductor Electrodes. *Acc. Chem. Res.* **2009**, *42*, 2017–2029.

(19) Liu, G.; Yu, J. C.; Lu, G. Q.; Cheng, H.-M. Crystal Facet Engineering of Semiconductor Photocatalysts: Motivations, Advances and Unique Properties.

Chem. Commun. **2011**, *47*, 6763–6783.

(20) Luttrell, T.; Halpegamage, S.; Tao, J.; Kramer, A.; Sutter, E.; Batzill, M. Why Is Anatase a Better Photocatalyst than Rutile? - Model Studies on Epitaxial TiO_2 Films. *Sci. Rep.* **2014**, *4*, 4043.

(21) Li, C.; Koenigsmann, C.; Ding, W.; Rudshteyn, B.; Yang, K. R.; Regan, K. P.; Konezny, S. J.; Batista, V. S.; Brudvig, G. W.; Schmuttenmaer, C. A.; et al. Facet-Dependent Photoelectrochemical Performance of TiO_2 Nanostructures: An Experimental and Computational Study. *J. Am. Chem. Soc.* **2015**, *137*, 1520–1529.

(22) Miao, L.; Tanemura, S.; Toh, S.; Kaneko, K.; Tanemura, M. Preparation and Characterization of Rutile-TiO_2 Nanorods. *J. Mater. Sci. Technol.* **2004**, *20*, 59–62.

(23) Liu, B.; Aydil, E. S. Growth of Oriented Single-Crystalline Rutile TiO_2 Nanorods on Transparent Conducting Substrates for Dye-Sensitized Solar Cells. *J. Am. Chem. Soc.* **2009**, *131*, 3985–3990.

(24) Li, Y.; Guo, M.; Zhang, M.; Wang, X. Hydrothermal Synthesis and Characterization of TiO_2 Nanorod Arrays on Glass Substrates. *Mater. Res. Bull.* **2009**, *44*, 1232–1237.

(25) Wang, S.-M.; Dong, W.-W.; Tao, R.-H.; Deng, Z.-H.; Shao, J.-Z.; Hu, L.-H.; Zhu, J.; Fang, X.-D. Optimization of Single-Crystal Rutile TiO_2 Nanorod Arrays Based Dye-Sensitized Solar Cells and Their Electron Transport Properties. *J. Power Sources* **2013**, *235*, 193–201.

(26) Huang, H.; Pan, L.; Lim, C. K.; Gong, H.; Guo, J.; Tse, M. S.; Tan, O. K. Hydrothermal Growth of TiO_2 Nanorod Arrays and in Situ Conversion to Nanotube Arrays for Highly Efficient Quantum Dot-Sensitized Solar Cells. *Small* **2013**, *9*, 3153–3160.

(27) Zhang, W.; Xie, Y.; Xiong, D.; Zeng, X.; Li, Z.; Wang, M.; Cheng, Y.-B.; Chen, W.; Yan, K.; Yang, S. TiO_2 Nanorods: A Facile Size- and Shape-Tunable Synthesis and Effective Improvement of Charge Collection Kinetics for Dye-Sensitized Solar Cells. *ACS Appl. Mater. Interfaces* **2014**, *6*, 9698–9704.

(28) Jarosz, M.; Syrek, K.; Kapusta-Kołodziej, J.; Mech, J.; Małek, K.; Hnida, K.; Łojewski, T.; Jaskuła, M.; Sulka, G. D. Heat Treatment Effect on Crystalline Structure and Photoelectrochemical Properties of Anodic TiO_2 Nanotube Arrays Formed in Ethylene Glycol and Glycerol Based Electrolytes. *J. Phys. Chem. C* **2015**, *119*, 24182–24191.

(29) Fakharuddin, A.; Di Giacomo, F.; Palma, A. L.; Matteocci, F.; Ahmed, I.; Razza, S.; D'Epifanio, A.; Licoccia, S.; Ismail, J.; Di Carlo, A.; et al. Vertical TiO_2 Nanorods as a Medium for Stable and High-Efficiency Perovskite Solar Modules. *ACS Nano* **2015**, *9*, 8420–8429.

(30) Guo, W.; Xu, C.; Wang, X.; Wang, S.; Pan, C.; Lin, C.; Wang, Z. L. Rectangular Bunched Rutile TiO_2 Nanorod Arrays Grown on Carbon Fiber for Dye-Sensitized Solar Cells. *J. Am. Chem. Soc.* **2012**, *134*, 4437–4441.

(31) Khalil, M.; Demirdöven, N.; Tokmakoff, A. Coherent 2D IR Spectroscopy: Molecular Structure and Dynamics in Solution. *J. Phys. Chem. A* **2003**, *107*,

5258–5279.

(32) Anderson, N. A.; Lian, T. Ultrafast Electron Transfer at the Molecule-Semiconductor Nanoparticle Interface. *Annu. Rev. Phys. Chem.* **2005**, *56*, 491–519.

(33) Baiz, C. R.; Kubarych, K. J.; Geva, E.; Sibert, E. L. Local-Mode Approach to Modeling Multidimensional Infrared Spectra of Metal Carbonyls. *J. Phys. Chem. A* **2011**, *115*, 5354–5363.

(34) El Nahhas, A.; Consani, C.; Blanco-Rodríguez, A. M.; Lancaster, K. M.; Braem, O.; Cannizzo, A.; Towrie, M.; Clark, I. P.; Záliš, S.; Chergui, M.; et al. Ultrafast Excited-State Dynamics of Rhenium(I) Photosensitizers [Re(Cl)$(CO)_3$(N,N)] and [Re(imidazole)$(CO)_3$(N,N)]$^+$: Diimine Effects. *Inorg. Chem.* **2011**, *50*, 2932–2943.

(35) Rosenfeld, D. E.; Gengeliczki, Z.; Smith, B. J.; Stack, T. D. P.; Fayer, M. D. Structural Dynamics of a Catalytic Monolayer Probed by Ultrafast 2D IR Vibrational Echoes. *Science* **2011**, *334*, 634–639.

(36) King, J. T.; Ross, M. R.; Kubarych, K. J. Water-Assisted Vibrational Relaxation of a Metal Carbonyl Complex Studied with Ultrafast 2D-IR. *J. Phys. Chem. B* **2012**, *116*, 3754–3759.

(37) Kiefer, L. M.; Kubarych, K. J. Solvent-Dependent Dynamics of a Series of Rhenium Photoactivated Catalysts Measured with Ultrafast 2DIR. *J. Phys. Chem. A* **2015**, *119*, 959–965.

CHAPTER 2

SUM FREQUENCY GENERATION SPECTROSCOPY

2.1 Theoretical Framework

The following framework parallels excellent in-depth discussions by the Simpson group and the Yan group.[1,2] Sum-frequency generation (SFG) is a nonlinear process that interrogates the optical and vibrational properties of a material.[3] The polarization, $\boldsymbol{P}$, i.e. the dipole moment per unit volume induced by external light fields, of any material is given generally as

$$\boldsymbol{P} = \epsilon_0 \boldsymbol{\chi}^{(1)} \cdot \boldsymbol{E} \tag{2.1}$$

where ϵ_0 is the permittivity of free space constant, $\boldsymbol{\chi}^{(1)}$ is the linear susceptibility which is a second-rank tensor, and $\boldsymbol{E}$ is the incident electric field which is a vector. When multiple interactions occur under the condition of high intensities, the polarization can be expanded as a power series

$$\begin{aligned} \boldsymbol{P} &= \epsilon_0 [\boldsymbol{\chi}^{(1)} \cdot \boldsymbol{E} + \boldsymbol{\chi}^{(2)} : \boldsymbol{EE} + \boldsymbol{\chi}^{(3)} \vdots \boldsymbol{EEE} + \cdots] \\ &\equiv \boldsymbol{P}^{(1)} + \boldsymbol{P}^{(2)} + \boldsymbol{P}^{(3)} + \cdots \end{aligned} \tag{2.2}$$

where $\boldsymbol{\chi}^{(2)}$ and $\boldsymbol{\chi}^{(3)}$ are the second- and third-order nonlinear susceptibilities which are third- and fourth-rank tensors, respectively. Second-, third-, and fourth-rank tensor multiplication operations are represented with "$\cdot$", "$:$", and "$\vdots$", respectively. Thus, $\boldsymbol{P}^{(1)}$ is the linear response, $\boldsymbol{P}^{(2)}$ is the second order (nonlinear) response, and so on. Since SFG is a two-photon process, it reports on the macroscopic polarization through

the second order nonlinear susceptibility, which contains the transition dipole and Raman polarizability strengths and orientations of the vibrational modes in the system, and can be written as follows

$$\boldsymbol{P}^{(2)} = \epsilon_0 \boldsymbol{\chi}^{(2)} : \boldsymbol{E}_1 \boldsymbol{E}_2 \tag{2.3}$$

where $\boldsymbol{E}_1$ and $\boldsymbol{E}_2$ are two different electric fields. Under the electric dipole approximation, $\boldsymbol{\chi}^{(2)}$ is nonzero only when the system exhibits a lack of inversion symmetry, an example of which would be an interface.

The SFG emission process is enhanced when one of the fields is on-resonance with a difference between two energy levels of the system. Often, these are vibrational energy levels: an infrared photon excites a vibrational mode and a visible photon upconverts the system into a virtual state at an energy equal to the sum of the incident photon energies, resulting in the emission of a photon at the sum of the frequencies. The energy level diagram for this process is shown in Figure 2.1.

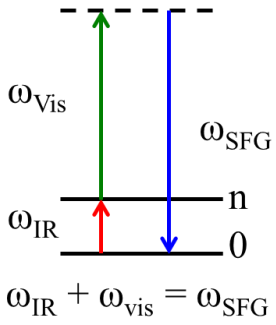

Figure 2.1 Energy level diagram for the nonlinear sum-frequency generation process.

The measured SFG intensity is related to $\chi^{(2)}$ through the following:

$$I_{SFG} = \left|\chi^{(2)}\right|^2 I_{vis} I_{IR} \tag{2.4}$$

The experimental observables are the frequency and the intensity of the emitted SFG field. The resonantly enhanced frequencies of the incident IR can be calculated based on the measured SFG spectrum and the known frequency of the upconversion field. Then, the measured surface vibrational spectrum is typically fit to a particular functional form. Each vibrational feature is assumed to have homogeneous broadening and is fit to a Lorentzian function in SFG experiments, however, this imposes purely homogeneous broadening in the system. Particularly in the condensed phase, this may not be applicable. Regardless, a Lorentizan of the following form is used:[1,2]

$$\chi^{(2)} = \chi_{NR}^{(2)} + \sum_{n} \frac{A_n}{\omega_n - \omega_{IR} - i\Gamma_n} \tag{2.5}$$

Where $\chi_{NR}^{(2)}$ is the nonresonant contribution from other processes, n is the resonant vibrational mode, A_n is the amplitude that contains the dipole and Raman transition strengths, ω_n is the frequency of the n^{th} vibrational mode, ω_{IR} is the frequency of the incident IR beam, and Γ_n is the damping coefficient of the n^{th} vibrational mode.

An alternative method of measuring SFG spectra is through interference with an external electric field. This technique, referred to as heterodyne-detection, is described in more detail in Chapter 3. Here, rather than measuring $\left|\chi^{(2)}\right|^2$, an interference term linear in $\chi^{(2)}$ is measured, which directly provides the absorptive (imaginary) and dispersive (real) lineshapes. Therefore, a Lorentzian functional form does not need to be assumed; rather, the absorptive spectrum can be fit to any lineshape function or analyzed as is.

2.2 Technical Experimental Details

The experiments described in this dissertation are far from black boxes working through the push a button. Therefore, it would be beneficial for future users to understand the appropriate alignment and optimization procedures. This section attempts to provide a thorough overview of the operations of these experiments, including some details regarding expected signal strengths and resolutions to some common issues.

2.2.1 Homodyne-Detected SFG Alignment

Two major requirements must be satisfied to effectively measure a SFG signal: the two beams (visible and IR) must be overlapped in space and in time. This section will detail the optics in place to make this process as reproducible as possible. To overlap the beams in space, the visible beam is aligned through the irises placed around the table, shown in Figure 2.2, using the mirror two mirrors before each iris.

For the IR alignment, a HeNe tracer beam is set to co-propagate with the infrared beam. This tracer beam is first aligned. Only two mirrors are needed to align the HeNe. A removable HeNe mirror is added between F3 and IRM2 (infrared-reflecting mirror). The HeNe mirror before the removable mirror centers the beam on the first iris, then the removable mirror centers it on the last iris after the sample position with the sample removed (not shown). Then, to align the IR, heat paper is used at these same two irises. Here, IRM1 centers the IR on the first iris, and IRM2 centers it on the last iris.

To ensure the two beams are overlapped in space at the sample, a 200 μm pinhole is placed at the focus of the IR beam (optimum power measured after the pinhole). The visible light is also directed through the pinhole. The spot sizes can be determined by measuring the power before and after the pinhole. Typical spot sizes are 300 μm diameter for the IR and 500 μm for the visible. In order to upconvert all of the IR, the visible should be slightly bigger.

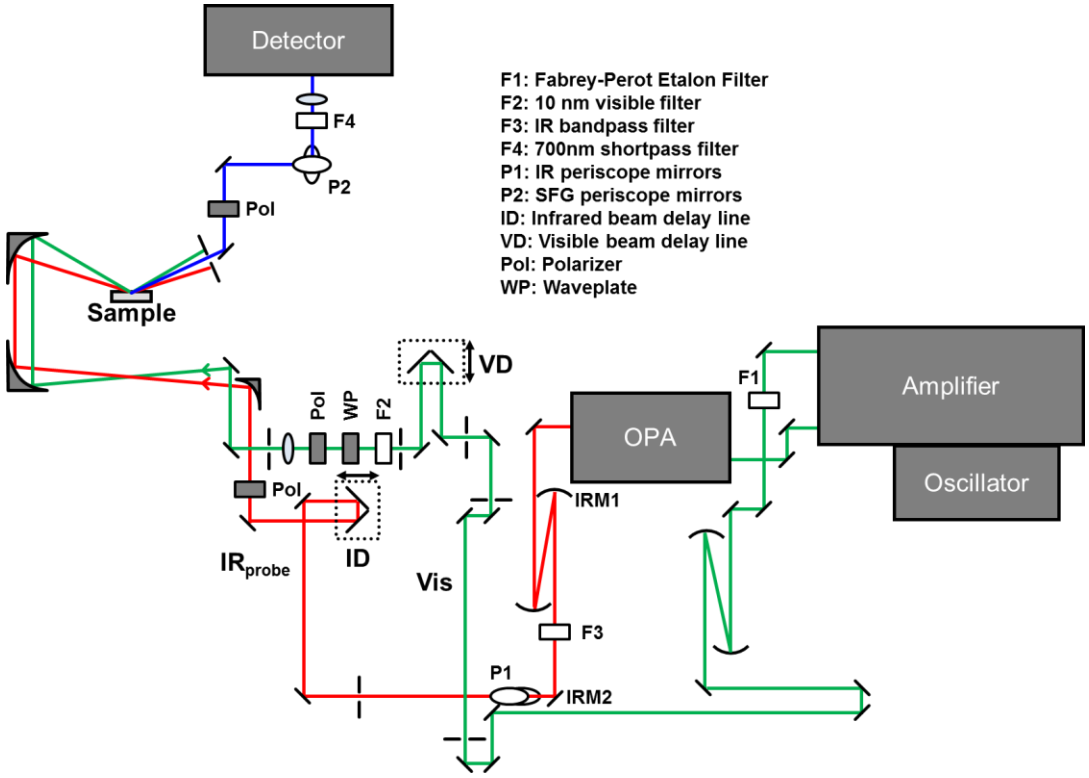

Figure 2.2 Overall experimental setup for homodyne-detected SFG experiments. The visible beam is shown in green, the IR_{probe} beam is red, and the generated SFG beam is blue.

With both beams overlapped in space, they need to be overlapped in time. To accomplish this, a nonlinear crystal such as $LiNbO_3$ is used which produces a bulk

SFG signal that can be seen by eye. After placing this reference crystal at the sample with the beams approximately perpendicular to the face of the crystal, and setting the IR delay line to the position used in the last experiment, the beams should be aligned well-enough that only the visible delay line needs to be moved by hand to see the SFG signal in transmission.

Once overlapped in space and time, the SFG response generated needs to be detected. By changing the $LiNbO_3$ crystal to be in reflection (beams are approximately 60° from the surface normal), the SFG signal is collimated and centered at the slit of the CCD detector.

Once the beams are aligned through the $LiNbO_3$ crystal, which has a bulk response, a sample with only a surface response needs to be used to fine-tune the beam optimization. With careful alignment, and the polarization set to *ppp* (in order of decreasing energy: polarization of the SFG, visible, and IR beams, respectively), a signal from the surface of a gold substrate should be visible on the CCD with 0.2 second integration time. This signal intensity is optimized by adjusting the spatial IR pointing before the sample to fine-tune the IR and visible beam overlap and by adjusting the motors in the grating compressor to minimize the temporal chirp of the IR beam before entering the optical parametric amplifier (OPA). Additionally, since timing was only set by hand, the visible delay line was scanned to obtain a cross-correlation, shown in Figure 2.3. A time delay of zero is defined as the IR stage time where the SFG signal in maximized. As the IR timing is scanned across the visible pulse, the signal outlines the intensity profile of the visible pulse, which displays a tail

with decreasing intensity, shown in the lower right inset of Figure 2.3. This visible temporal profile is due to interference in the Fabrey-Perot etalon filter.

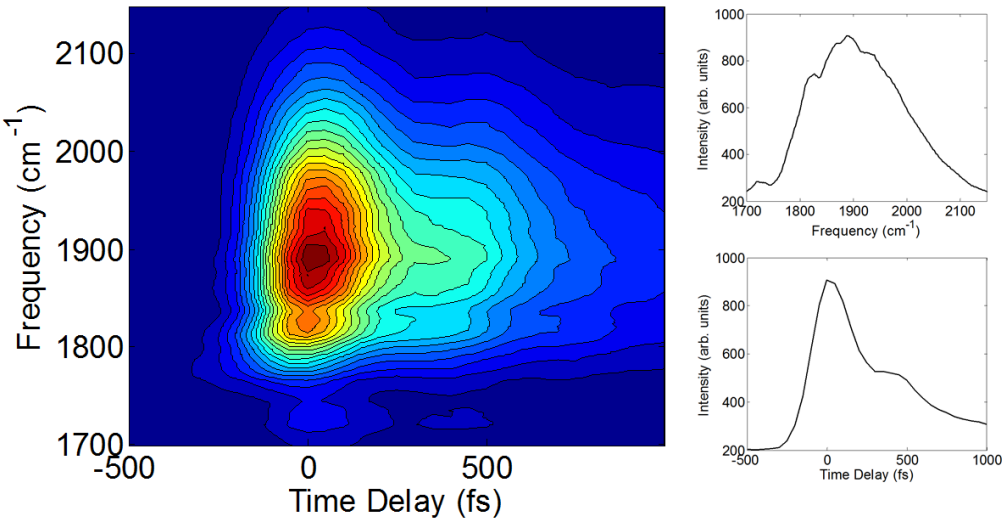

Figure 2.3 Left: Cross-correlation between visible and infrared beams collected on gold in *ppp* polarization. Top right: slice taken at zero time delay. Bottom right: slice taken at 1900 cm^{-1}.

2.2.2 Heterodyne-Detected SFG

If the precise alignment procedure detailed in the previous section is followed, the additional steps needed to set up heterodyne-detection are relatively straightforward. The Heterodyne-Detected (HD) SFG technique uses an additional SFG field to interfere with the field generated at the sample. Another nonlinear crystal, such as ZnO-coated CaF_2 or y-cut quartz, is placed in the focus of the visible and IR before the sample to generate an additional field called the local oscillator (LO).[4,5] The SFG_{LO} field is delayed with respect to the SFG_{sample} field by passing it through a delay plate.

The thickness of the delay plate has an influence of the data collected; this influence is described in detail in Chapter 3.

The signals of the SFG_{sample} and SFG_{LO} are monitored on the CCD detector after being dispersed in a polychromator. The intensity of the LO field can be changed by translating the LO in space through the focus and overlap of the visible and IR beams. The LO-generating crystal position is set so that the intensity matches that of gold. The spectral envelope should also match gold- this can be tuned by rotating the ZnO in the plane of the table. The position of the LO with respect to the beams should mirror the sample so that the overlapped region of the beams is consistent at the two positions. Finally, the two fields should overlap with each other on the CCD. The CCD software imaging mode displays the intensity at each of the 1340 by 400 pixels. While the x-axis corresponds to the wavelength being detected, the position on the y-axis is determined by where the beam physically hits the detector. The SFG beams typically span a few y-pixels, which is called the beams' y-strip. The y-strip of the LO seen in imaging mode can be adjusted by rotating the delay plate, thereby translating the SFG_{LO} with respect to the IR and visible at the sample. It is also important, especially when studying samples on prisms, that the beams are focused onto the detector well. With these procedures performed, deep vertical interference fringes should be observed on the CCD (see Figure 3.1 and 3.2 in Chapter 3).

2.2.3 Time-Resolved SFG

In order to obtain vibrational-lifetime information, an additional infrared excitation is

needed. The required pump beam is created by splitting off a portion from the original infrared probe with a KBr beam splitter. By ensuring that the probe is well aligned, the pump is by default passively aligned with respect to the sample and only small adjustments in the pointing of the IR beam need to be done to overlap the pump with the IR probe and visible beams in space on the pinhole placed at the sample position. As previously mentioned, the visible beam diameter should be slightly larger than the IR probe beam so all of the IR is upconverted. Similarly, the IR pump should be slightly larger than the probe to ensure the entire probe spot is excited.

To overlap the three beams in time, initial coarse adjustments of the pump translation stage are done while optimizing on $LiNbO_3$. A precise temporal overlap is important since both the IR pump and probe pulses are very short in time (~100 fs for experiments in the 2100 cm^{-1} region and 80 fs for experiments described in Chapter 6). To accomplish this alignment, a third order cross-correlation between the visible, IR probe, and IR pump beams, shown in Figure 2.4, is measured when looking at the SFG signal from gold on the CCD camera. The pump stage is scanned, while the probe and visible stages are stationary.

Since this is a third order, i.e. bulk, process the visible power should be attenuated and the grating position will need to be adjusted. For example, when studying metal-C≡O stretches centered at 2100 cm^{-1} (~4760 nm), the SFG signal emitted will have a wavelength of

$$\lambda_{\mathrm{SFG}} = \frac{1}{\frac{1}{\lambda_{\mathrm{Vis}}} + \frac{1}{\lambda_{\mathrm{IR,probe}}}} = \frac{1}{\frac{1}{793\mathrm{nm}} + \frac{1}{4760\mathrm{nm}}} \approx 680 \text{ nm}$$

While the third order IR+IR+Visible (IIV) signal will have a wavelength of

$$\lambda_{\mathrm{IIV}} = \frac{1}{\frac{1}{\lambda_{\mathrm{Vis}}} + \frac{1}{\lambda_{\mathrm{IR,probe}}} + \frac{1}{\lambda_{\mathrm{IR,pump}}}} = \frac{1}{\frac{1}{793\mathrm{nm}} + \frac{1}{4760\mathrm{nm}} + \frac{1}{4760\mathrm{nm}}} \approx 590\ \mathrm{nm}$$

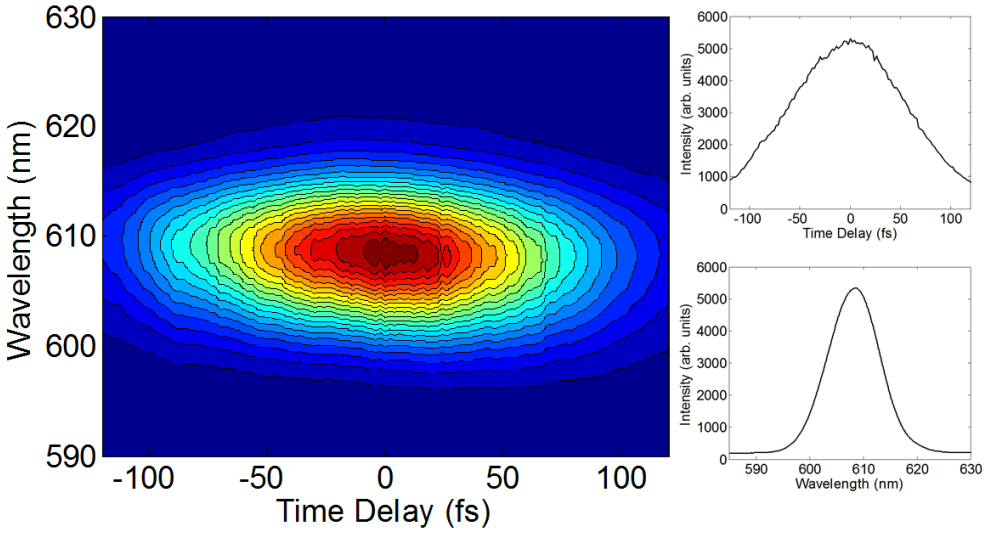

Figure 2.4 Left: Cross-correlation between IR pump, IR probe, and visible beams collected on gold in ppp polarization. Top right: slice taken at zero time delay. Bottom right: slice taken at 608 nm. FWHM of 146 fs from a Gaussian fit corresponds to an IR pulse duration of 103 fs assuming an infinitely long visible pulse which essentially up-converts the two pulse IR + IR autocorrelation.

Since time-resolved experiments can involve acquisition times on the order of hours, laser fluctuations need to be taken into account when monitoring the vibrational relaxation. To account for these fluctuations, we have adapted a solution first described by the Bonn group.[6] An optical chopper is placed in the pump beam path and is driven with a 500 Hz sine wave from a function generator. Because the laser output is modulated at 1 kHz, every other pump pulse is blocked. The 500 Hz sine

wave is also sent to a galvanometric mirror (Thorlabs, GVS011), which vertically displaces the SFG spectrum generated from every other pulse. Therefore, the SFG_{static} signal arising from IR_{probe}+Visible beams appears in one region of the CCD camera, while the SFG_{pumped} signal from IR_{probe}+Visible beams with the additional pump interaction appears in a different region on the CCD camera (Figure 2.5).

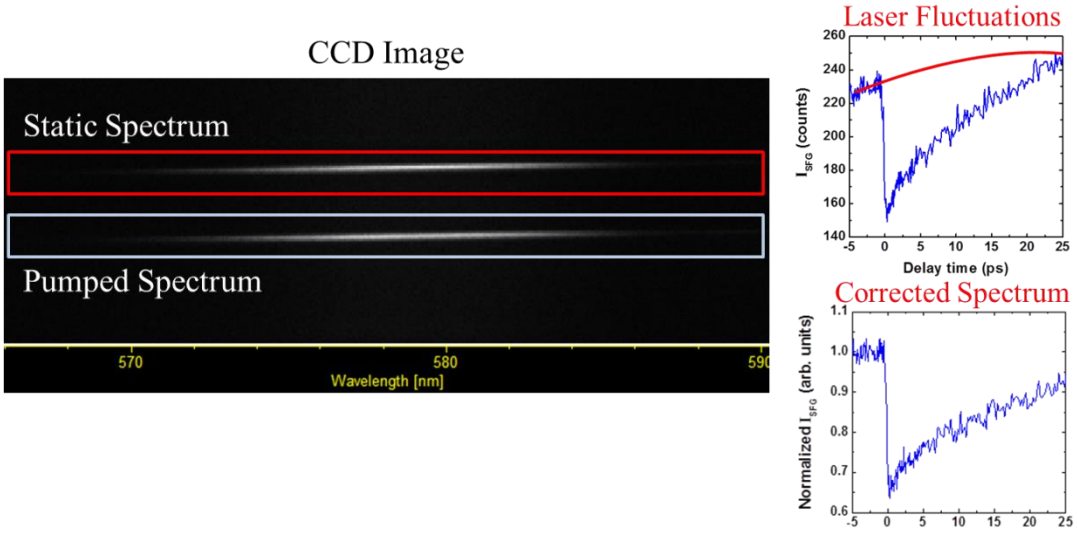

Figure 2.5 Binning two different regions of interest on the CCD to separate out the static spectrum and the pumped spectrum to correct for laser fluctuations. The stages are translated such that the scan begins at longer waiting times.

The static spectrum provides the intensity normalization. If there is sample degradation over the course of a scan or during signal averaging, a motorized linear actuator can be added to the horizontal and/or vertical dimensions of the sample stage (Figure 2.6). The actuators translate the sample to that the beams repeatedly hit a different spot on the sample.

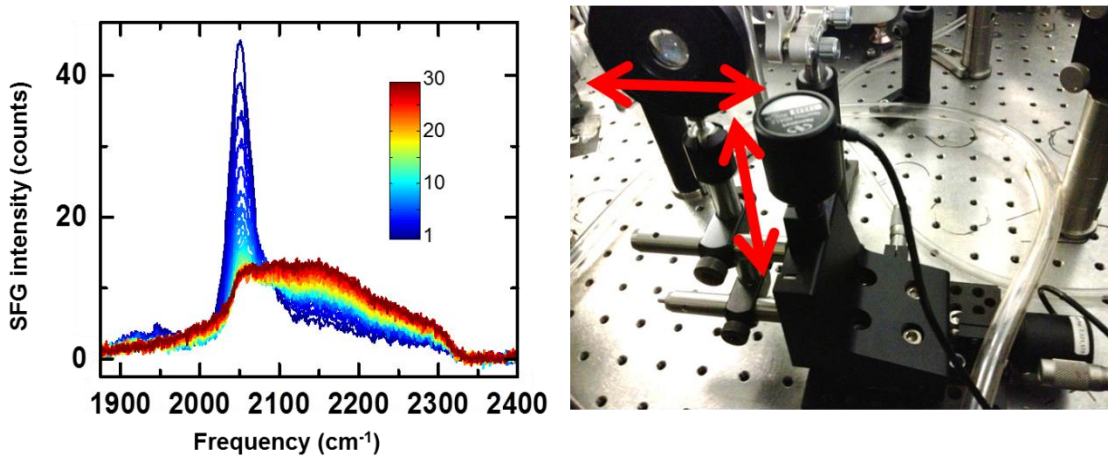

Figure 2.6 Significant sample degradation occurred over the course of 30 scans for a $Re(CO)_3$ sample. By translating the sample in the horizontal and vertical dimensions with linear actuators, the photodamage is minimized.

2.2.4 Two-Dimensional SFG

When performing two-dimensional SFG experiments, an additional interaction is involved. The excitation pulse described for time-resolved SFG is split again with another KBr beamsplitter, with the second portion directed into a stationary stage, shown in Figure 2.7.

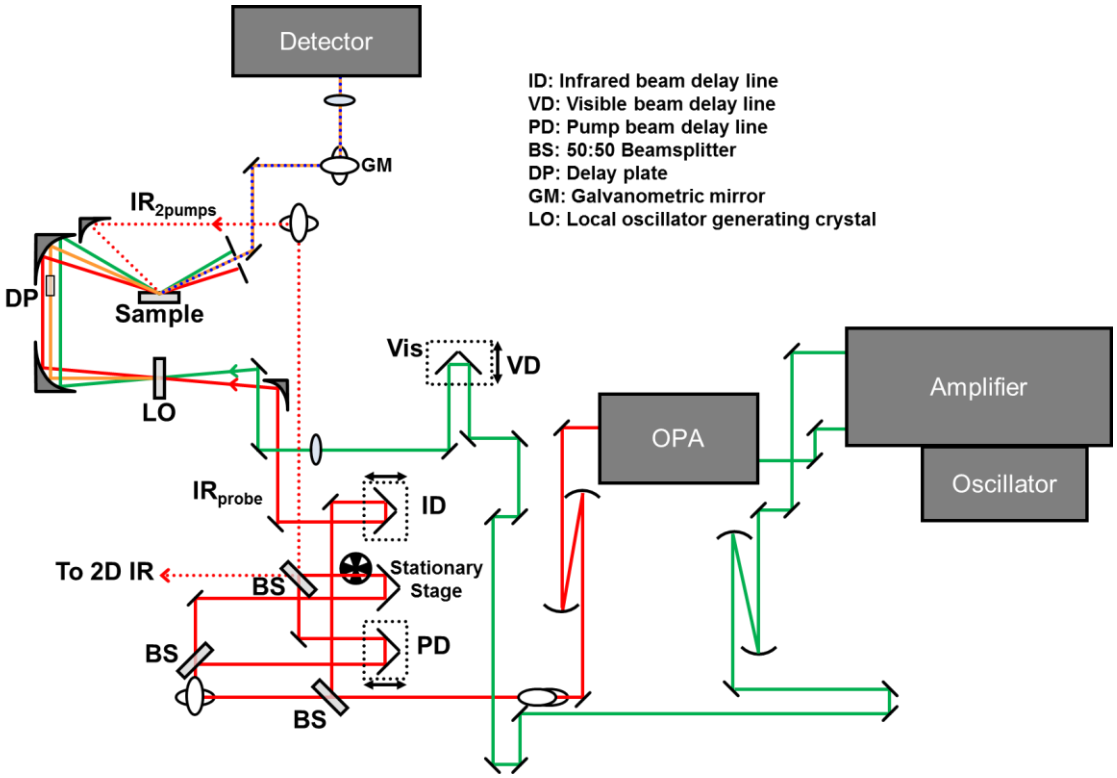

Figure 2.7 Experimental setup for two-dimensional SFG experiments. The visible beam is shown in green, the IR_{probe} beam is red, the generated SFG beam from the local oscillator is yellow, and the generated SFG beam from the sample is blue.

To determine the zero timing between the two pump pulses, the intensity of the IR beam at the output of the interferometer is measured on a room temperature MCT detection as a function the delay line in the interferometer. This autocorrelation is shown in Figure 2.8.

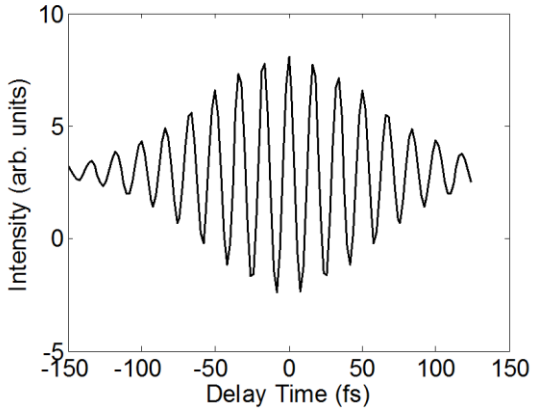

Figure 2.8 Autocorrelation measured for the two pumps in the interferogram. Zero time is determined to be the center of the interference.

This procedure relies on lock-in detection and amplification. The electronics are set according to Figure 2.9.

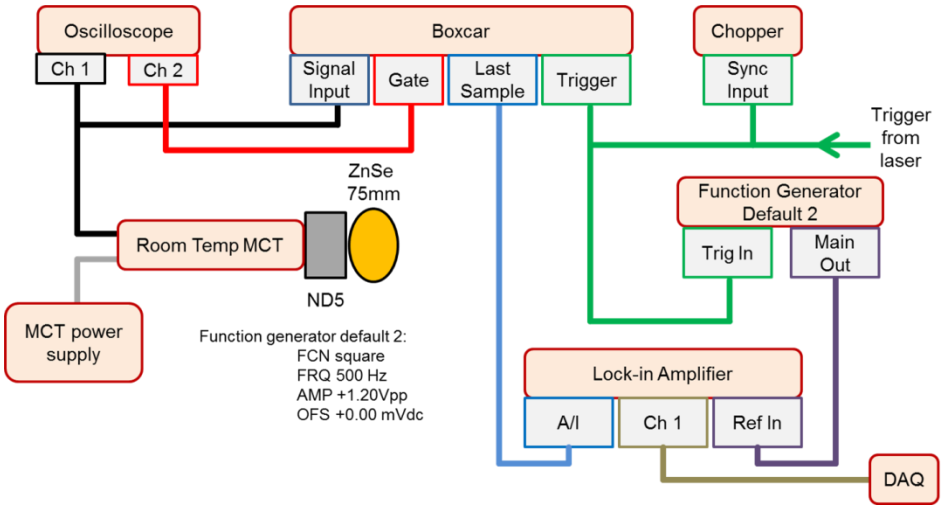

Figure 2.9 Diagram of electronics needed for IR pump autocorrelation. ND5 is a neutral density filter with an optical density of 5 to prevent any damage to the HgCdTe (MCT) detector, which is before a lens (ZnSe 75mm focal length) to focus the IR into the MCT.

It is necessary to set the relative timing of the beams in the correct order, since one of the translation stages is stationary. To accomplish this, first measure the autocorrelation to set the moving pump stage relative to the stationary pump stage. Then,

1. Align visible, IR_{probe}, and IR_{pump} through pinhole at sample following procedure from section 2.2.1.
2. Add the LO-generating crystal (doing so will delay the Vis and IR probe with respect to the IR pump so the visible and IR timings will need to be adjusted)
3. Roughly find timing in the $LiNbO_3$ crystal with the three beams, using the stationary pump stage (block the moving pump stage). When all three are timed up in $LiNbO_3$, multiple-order signals can be seen, as in Figure 2.10
4. Align $LiNbO_3$ in reflection and direct SFG_{pump} and SFG_{probe} into the CCD simultaneously
5. Roughly optimize IR_{probe} pointing and timing on the gold SFG signal
6. Optimize IR pump pointing and timing on the SFG_{pump} signal, changing the Vis translation stage
7. Optimize IR probe pointing and timing on SFG_{probe}, changing probe translation stage
8. Fine-tune IR pump pointing and IR probe timing on IIV signal, described in section 2.2.3.

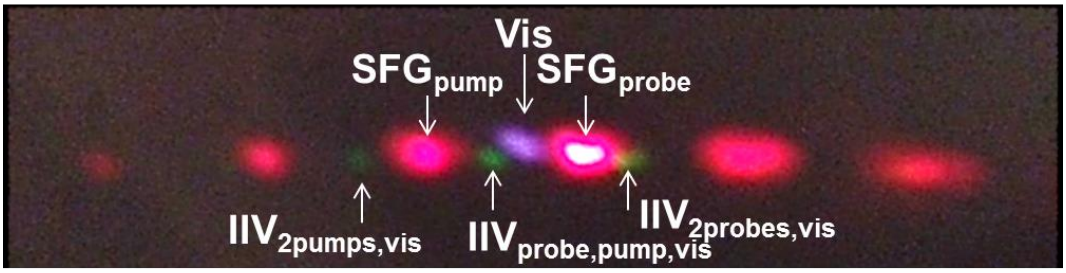

Figure 2.10 Multi-order signals generated in $LiNbO_3$ in transmission. Spots are horizontally separated after the sample, but vertically separated at the CCD slit due to the periscope. Thus, they can be binned separately.

The galvanometric mirror and chopper then need to be synchronized as in section 22.3, with one of the pumps blocked. Additional details regarding collecting 2D SFG data are provided in Chapter 4.

2.3 References

(1) Moad, A. J.; Simpson, G. J. A Unified Treatment of Selection Rules and Symmetry Relations for Sum-Frequency and Second Harmonic Spectroscopies. *J. Phys. Chem. B* **2004**, *108*, 3548–3562.

(2) Yan, E. C. Y.; Fu, L.; Wang, Z.; Liu, W. Biological Macromolecules at Interfaces Probed by Chiral Vibrational Sum Frequency Generation Spectroscopy. *Chem. Rev.* **2014**, *114*, 8471–8498.

(3) Boyd, R. W. *Nonlinear Optics*, Third.; Elsevier Inc.: Burlington, 2008.

(4) Vanselous, H. ; Petersen, P. B. Extending the Capabilities of Heterodyne-Detected Sum-Frequency Generation Spectroscopy: Probing Any Interface in

Any Polarization Combination. *J. Phys. Chem. C.* **2016**, *120*, 8175–8184.

(5) Superfine, R.; Huang, J. Y.; Shen, Y. R. Phase Measurements for Surface Infrared-Visible Sum-Frequency Generation. *Opt. Lett.* **1990**, *15*, 1276-1278.

(6) Ghosh, A.; Smits, M.; Bredenbeck, J.; Dijkhuizen, N.; Bonn, M. Femtosecond Time-Resolved and Two-Dimensional Vibrational Sum Frequency Spectroscopic Instrumentation to Study Structural Dynamics at Interfaces. *Rev. Sci. Instrum.* **2008**, *79*, 93907.

CHAPTER 3

HETERODYNE-DETECTED SFG: EXTENDING THE CAPABILITIES OF HETERODYNE-DETECTED SUM-FREQUENCY GENERATION SPECTROSCOPY*

3.1 Introduction

Understanding interfacial structure and chemistry is critical in many important applications including atmospheric and terrestrial processes, catalysis, and biological systems. Sum-frequency generation (SFG) spectroscopy is uniquely suited for studying noncentrosymmetric environments such as the interfaces and surfaces of centrosymmetric bulk phases. As a second-order nonlinear technique, SFG is forbidden in a centrosymmetric environment within the electric dipole approximation and probes only the interfacial layer of molecules, which exhibit a net asymmetry.[1–3] In conventional homodyne-detected SFG, the measured quantity is the intensity of the emitted SFG light, providing information on the square modulus of the second-order nonlinear susceptibility $|\chi^{(2)}|^2$. As such, the real and imaginary components of $\chi^{(2)}$ interfere, which can lead to significant distortions of the resonant features of the SFG spectrum. Furthermore, the signal in a homodyne-detected SFG experiment depends quadratically on the molecular concentration, making it difficult to measure SFG responses at low concentrations.[4] Obtaining the real and imaginary parts of the complex susceptibility avoids the complications arising from interference between the

two terms and affords absolute orientation of the molecules at the interface. The complex terms of $\chi^{(2)}$ can be derived from the careful fitting of homodyne-detected SFG data or by measuring at least two different polarization combinations.[5,6] However, an established technique for overcoming these limitations and obtaining $\chi^{(2)}$ directly is heterodyne-detected SFG spectroscopy. Incorporating heterodyne detection in SFG overcomes both of these obstacles, allowing detection of the absorptive imaginary component of $\chi^{(2)}$, leading to absolute orientation determination and a linear concentration dependence with improved signal-to-noise ratio, particularly at low concentrations.

Although phase information of an SFG response was first extracted interferometrically by Superfine et al. in 1990,[7] the general technique has only been adapted by about a dozen labs to study just a handful of different aqueous interfaces, likely due to the technological complexity and limitations in current implementations.[8] There have been two main approaches to extracting the complex phase of the non-linear susceptibility. The first,[7,9] developed by the Shen group, is often referred to as phase-sensitive SFG (PS-SFG) and has primarily been adopted by those using narrowband picosecond (ps) scanning infrared (IR) sources. In this geometry, collinear IR and visible beams generate a reference SFG field, termed the local oscillator (SFG_{LO}), in a nonlinear crystal, which is then delayed with respect to the incident beams by a transparent material. All three beams- SFG_{LO}, visible, and IR- are re-focused onto a sample to generate the sample SFG field (SFG_{sample}). The delay plate is rotated to vary the phase between SFG_{sample} and SFG_{LO} fields, producing an

interference pattern. This technique boasts high phase stability as all of the beams are passing through common optics, but requires a number of different measurements to obtain the absolute phase. This technique has been used to measure OTS monolayers on fused silica,[9,10] solid-water interfaces,[11–13] air-water interfaces,[14,15] and air-polymer film interfaces.[16,17]

The second approach to interferometrically determine the phase of the complex nonlinear susceptibility is commonly termed heterodyne-detected SFG (HD-SFG). This method was first implemented by the Benderskii group[4] with broadband femtosecond (fs) IR vibrational SFG and by the Tahara group with broadband electronic and vibrational SFG.[18,19] In the Benderskii design[4], small portions of the IR and visible beams were diverted and focused through a nonlinear crystal to generate the local oscillator (LO) that was then overlapped with the sample field by re-focusing the three beams. The time delay between SFG_{LO} and SFG_{sample} signals was controlled with a delay stage. Since SFG_{LO} was generated separately and passed through independent optics, this setup suffered from a phase drift that required independent post-processing correction for each of the 100 second integration time acquisitions.

In the Tahara group's design,[19] IR and visible beams were first focused onto the sample, creating an SFG response, after which the SFG_{sample} signal was delayed through a fused silica plate. All three beams were re-focused with a spherical mirror onto a GaAs crystal to generate the LO field. This design, where the beams are directed with common optics, increased the phase stability to be reliable over the course of a few hours.[19] However, for geometries in which the beams interacted with

the sample before generating the LO (sample-first geometry), the data collected of the air-water interface proved to require careful correction due to the frequency dependent reflectivity of water in the IR region studied.[20] When compared to PS-SFG, this technique allowed for shorter data collection times due to the use of broadband IR pulses and required the collection of only one sample and one reference spectrum. To date, HD-SFG has been adopted by few research groups and used to study a relatively narrow selection of systems, mostly air-aqueous solution interfaces. These systems include monolayers and lipids at the air-water interface,[4,21,22] surfactants and salts at the air-water interface,[19,20,23–28] the isotopically diluted air-water interface,[29] solvated water at the air-water interface,[30] chiral proteins at the air-water interface,[31] CO on Pt(111),[32] and a rhenium bipyridyl catalyst on rutile TiO_2[33], most of which were collected in the *ssp* polarization combination (polarization of SFG_{sample}, visible, and IR beams, respectively). Very recently, the buried polyelectrolyte/water interface was studied with HD-SFG, but the complex spectrum could not be obtained due to difficulty of obtaining a suitable reference spectrum.[34] As described in detail in this chapter, we solved this complication by including the reference on the same surface as the sample[35] enabling us to obtain the first phase-resolved HD-SFG spectrum of a buried surface.

A thorough overview of the previous methods can be found in two reviews published in 2013.[36,37] Most recently, two groups have combined aspects of these two techniques. Yamaguchi[38] performed HD-SFG with picoseond-duration IR pulses in a nearly collinear LO-first geometry before refocusing onto a sample. This method

exhibits 4 cm^{-1} resolution but required a number of different measurements to extract the phase for the water-air interface. Meanwhile, Xu et al.[39] adopted a LO-first collinear geometry with femtosecond-duration IR pulses. All three beams- SFG_{LO}, visible, and IR- passed through a thick delay plate and a lens to re-focus onto the sample. Due to the frequency-dependent delay introduced into the IR and visible pulses from the delay plate, it was necessary to intentionally de-tune the IR and visible temporal overlap at the LO-generation position to optimize the temporal overlap at the sample. A 10 mm thick MgF_2 window was needed to produce a 2 ps time delay between SFG_{LO} and SFG_{sample}. Due to the collinear geometry, they were able to obtain a phase stability of ±5° over the course of 30 minutes.

Despite the advances in interferometrically phase-resolved SFG within the past few decades, the method has not been widely integrated due to the increased technical difficulty when compared to homodyne-detected SFG. Additionally, the available techniques have been quite restricted in terms of surfaces and polarizations available to study, largely due to the high reflection losses of *p*-polarized light on transparent materials. There is still a need for a geometry that is readily adaptable for all polarizations and all interfaces, requires few measurements, is phase stable over extended periods of time, is easy to incorporate in existing SFG setups, and can conveniently be reverted to homodyne-detected SFG. Described here is an experimental design that fulfills all of these needs. By building on the previous methods described above, we have designed a new experimental geometry that is demonstrated to be capable of probing front air-solid surfaces, buried solid-air

surfaces, and buried solid-liquid interfaces in different polarization combinations. The key features of our design include generation of the LO in transmission before the sample, collimation of the beams between SFG_{LO} generation and sample with parabolic mirrors which allows for full polarization and timing control of the three beams, and the use of ZnO to generate the LO field. The advantage of each of these features is described below. Once the optics are in place, day-to-day operations are no more complicated than in conventional SFG experiments. The method is illustrated for a model self-assembled monolayer of octadecyltrichlorosilane (OTS) with sharp, distinct methyl vibrational stretches in *ppp* and *ssp* polarization combinations and found to be stable for over ten hours – long enough to eliminate the need for post-process phasing between scans and to perform data collection over extended times needed for advanced techniques such as time-resolved HD-SFG and 2D-HD-SFG.

3.2 Experimental Methods

Our homodyne-detected SFG experimental setup used for both static and transient SFG is described in detail elsewhere.[40,41] Briefly, a Ti:sapphire amplifier (Coherent Legend Elite Duo) seeded by a Ti:sapphire oscillator (Coherent Micra-5) generates 25 fs, 800 nm, 5 mJ pulses at a 1 kHz repetition rate. To generate our visible beam, 0.75 mJ of this output is filtered through a Fabry-Perot etalon (TecOptics, Inc.), while 3 mJ is used to generate tunable broadband IR pulses in a tunable commercial optical parametric amplifier (Coherent OPerA Solo). An overhead view of our experimental design for HD-SFG experiments is shown schematically in the top panel of Figure 3.1.

While the current setup includes a vertical sample geometry, it can easily be adapted to a horizontal sample geometry needed for studying air-liquid interfaces.

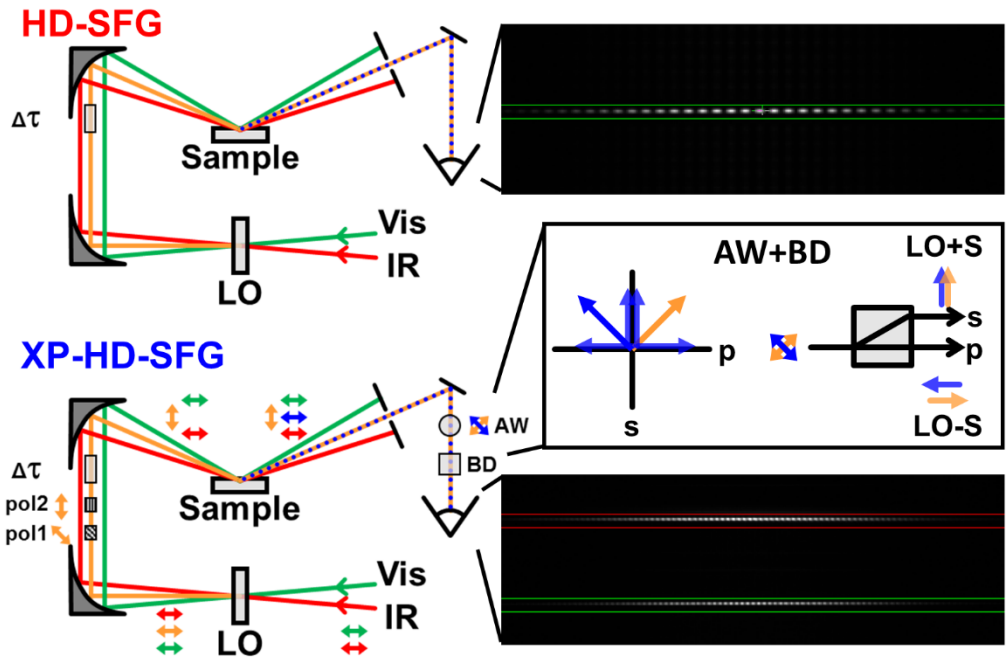

Figure 3.1 Top: HD-SFG setup including the local oscillator generating material (LO), delay plate (Δτ), sample, detector, and visible (green), IR (red), SFG_{LO} (yellow), and SFG_{sample} (blue dotted) beams. Inset shows image from CCD and region to be binned outlined in green. Bottom: Cross-polarized (XP) heterodyne-detected SFG setup. Polarizations represented with arrows of the corresponding beam color: horizontal arrows are *p*-polarized and vertical arrows are s-polarized. Polarization rotation is provided by pol1 (45° polarizer) and pol2 (90° polarizer). Other optical components include an achromatic waveplate (AW) and beam displacer (BD). Insets show AW and BD separating the *s*- and *p*-polarized components of the beams (middle) and CCD image of two regions to be binned (bottom).

In our geometry, the visible (central wavelength: 792.8 nm, bandwidth: 0.6 nm, pulse energy: 10 μJ) and IR (central wavelength: 2920 cm^{-1}, bandwidth: 290 cm^{-1}, pulse energy: 5 μJ) beams are focused through a transparent material to generate SFG_{LO} by an N-BK7 plano-convex lens (Thorlabs, LA1461-B) and a 90° off-axis parabolic mirror (Thorlabs, MPD169-P01), respectively. The material is in this case a 150 nm thin film of ZnO on soda lime glass (MTI Corporation). The three beams – SFG_{LO}, visible, and IR – are collimated with a 90° off-axis parabolic mirror (Thorlabs, MPD269-P01) before being refocused by a 60° off-axis parabolic mirror (PIKE Technologies, 300-1246-51) onto the sample. In this collimated region, the SFG_{LO}, visible, and IR beams are spatially separated by about 40 mm, which allows for the addition of any other optics, such as polarizers, waveplates, or filters, needed in the three beams. A delay plate of fused silica introduces a time delay, $\Delta\tau$, between the SFG_{LO} and the other two beams of approximately 6 ps for a 2 mm thick delay plate typically used. The SFG_{LO}, visible, and IR beams are then re-focused onto a 150 nm Au thin film reference or octadecyltricholorosilane (OTS) monolayer sample, at which point another SFG signal is generated— $SFG_{reference}$ or SFG_{sample}, respectively. The OTS sample was prepared on fused silica according to published literature procedures[35] and included a 5 mm diameter, 150 nm thick spot of Au deposited directly on the same surface as the monolayer as the reference. The SFG signals were then focused onto the slit of a polychromator (Princeton Instruments, Acton SP2500) where they were dispersed by a diffraction grating (600 grooves/mm, blazed at 500 nm). At the output of the polychromater, the light was spectrally narrowed, causing

the SFG_{LO} and SFG_{sample} (or $SFG_{reference}$) fields to interfere in time, producing fringes that could be seen when imaged on the liquid-nitrogen-cooled CCD camera (Princeton Instruments, Model 7509-0001, 1340 x 400 pixels). The resulting interferogram (insets in Figure 3.1) was typically five pixels high and vertically binned across 10 pixels. The spectral resolution corresponds to the bandwidth of the visible pulse, which is 10 cm^{-1}. Reference data was collected with a 0.5 second integration time and averaged over 10 scans, while sample data was collected with a 10 second integration time and averaged over 40 scans. Background data was collected between each scan for the same integration time by delaying the visible light pulse by 20 ps with respect to the IR pulse. The data obtained with this technique is denoted "HD-SFG data." To collect "homodyne-detected" SFG data (measuring $|\chi^{(2)}|^2$), the SFG_{LO} signal was blocked between the parabolic mirrors. Analogously, to obtain spectra of only the SFG_{LO}, the IR beam was blocked between the parabolic mirrors.

An advantage of the current experimental geometry is the ability to control the polarization and timing of the individual beams between the parabolic mirrors. This allowed us to compensate for poor reflectivity of *p*-polarized light at the sample using the cross-polarized heterodyne-detected SFG (XP-HD-SFG) setup, depicted in the bottom panel of Figure 3.1.

Polarization control of the SFG_{LO} in XP-HD-SFG allows for heterodyne detection of any SFG polarization combination by interfering the SFG_{sample} with an orthogonally polarized SFG_{LO} field. For the case of traditional HD-SFG in *ppp*-polarization, the SFG_{LO} is also *p*-polarized and has high reflection losses for many

systems of interest at typical incident angles. The combination of two dichroic film linear polarizers (Thorlabs, LPVISE2X2), the first at 45° and the second at 90° with respect to the SFG_{LO} polarization, rotates the SFG_{LO} polarization from *p* to *s* (or *s* to *p* for *ssp*-polarization combination), albeit reducing the SFG_{LO} intensity. Thus, the SFG_{sample} polarization is perpendicular to the SFG_{LO}. Rotating the polarization of the LO field allows for heterodyne detection to be performed in polarization combinations where SFG_{LO} would have poor reflectivity at the sample, as is discussed in the results section. An achromatic λ/2 waveplate (Eksma, 467-4205) rotated the two orthogonal SFG beams by 45° degrees, and a calcite beam displacer (Thorlabs, BD27) spatially separated the *s* and *p* components of the beams producing SFG_{LO} +/- SFG_{sample} combinations in the two directions. This spatial separation was imaged on two different strips on the CCD, and each was vertically binned into two separate regions of interest (ROI).

3.3 Results and Discussion

In conventional SFG, the measured quantity is the intensity of SFG light,[2,3,42]

$$I_{SFG} \propto \left|E_{sample}\right|^2 \propto \left|\chi^{(2)}\right|^2 \tag{3.1}$$

where E_{sample} is the electric field of the SFG light from the sample and $\chi^{(2)}$ is the second-order nonlinear susceptibility. In HD-SFG, an LO field with a given time delay with respect to the SFG_{sample} is also introduced:

$$I_{HD-SFG} \propto \left|E_{LO}(t)e^{i\omega\Delta\tau} + E_{sample}(t)\right|^2 \tag{3.2}$$

$$= |E_{LO}|^2 + \left|E_{sample}\right|^2 + E_{LO}E^*_{sample}e^{i\omega\Delta\tau} + E^*_{LO}E_{sample}e^{-i\omega\Delta\tau} \qquad (3.3)$$

where E_{LO} is the electric field of the LO and $\Delta\tau$ is the time delay between the sample and LO electric fields. The interferogram in the CH vibrational stretch region as measured on the detector is shown in Figure 3.2 for the Au reference (top) and OTS monolayer on the front surface (middle) and buried dry surface (bottom) of fused silica in *ppp* and *ssp* polarization combinations, respectively. The depth of the interference fringes is determined by the relative strength of the SFG_{sample} compared to SFG_{LO}, as exemplified in the comparison of the middle panel to the bottom panel in Figure 3.2. In the middle panel, the LO is relatively weak due to the high reflection loss of the *p*-polarized SFG_{LO}. Here, the homodyne signal is more intense than the heterodyned signal, which shows up as interference fringes on top of the homodyne peaks. Meanwhile, in the bottom panel, the LO intensity is higher as more LO light is reflected off of the sample, and so the heterodyned signal is seen clearly as interference fringes. The XP-HD-SFG geometry can overcome the high reflection losses of *p*-polarized light if a larger LO signal is needed, as will be illustrated later in this section. In the current case of strong CH stretches of an ordered monolayer, the LO field strength was adequate and the HD-SFG data in the following comparison was collected in the setup described in the top panel of Figure 3.2. The data analysis is demonstrated for the case of the front surface of the substrate in the *ppp* polarization combination.

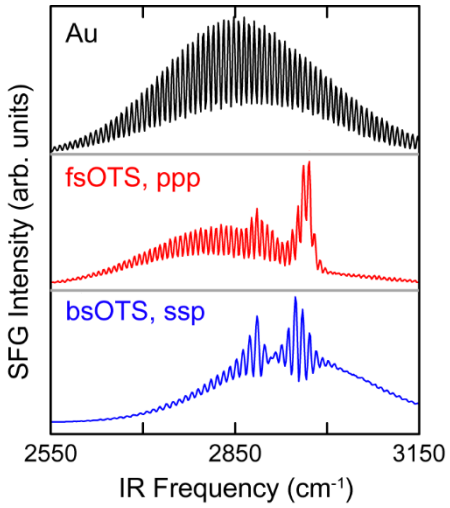

Figure 3.2 Heterodyne-detected SFG signal of Au reference (top), front air-OTS surface in *ppp* polarization (middle) illustrating a weak LO field, and buried OTS-air interface in *ssp* polarization (bottom) illustrating a strong LO field.

To extract the real and imaginary components of the spectra, we follow the standard data analysis which has been established for HD-SFG.[4,19] The data was first Fourier transformed into the time domain, shown in the top panel of Figure 3.3. The first two terms in Equation (3.3) are the homodyne contributions and are independent of the time delay, $\Delta\tau$. Accordingly, they show up around zero time delay in the top panel of Figure 3.3. Meanwhile, the third and fourth terms in Equation (3.3) correspond to the heterodyned components at ±6.2 ps, introduced by a 2 mm fused silica delay plate. A double-sided Hanning window was used to filter out the unwanted homodyne signals. The width and rise-time of the window was adjusted to reduce the noise introduced by the FFT procedure without clipping the free induction decay (FID) of the molecular vibration to maintain the peak shape and intensity. The bottom panel of Figure 3.3 shows the region to be windowed, highlighting the decay of the

FID towards earlier times for the CH vibrations in the sample compared to the instantaneous response from nonresonant Au. The FID decaying towards earlier times is a consequence of delaying the SFG_{LO} with respect to the SFG_{sample}, described further below.

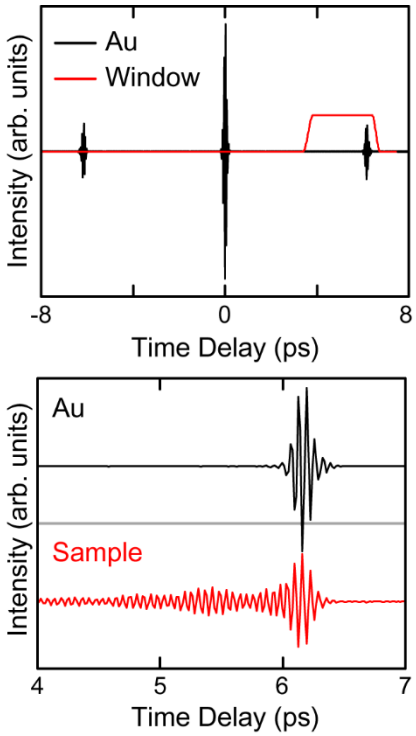

Figure 3.3 Top: Imaginary components of the fast Fourier transform of the imaginary components of the Au data into the time domain (black) and Hanning window function (red). Bottom: Scaled view with cross-term of interest for the imaginary component of Au reference (black) and OTS sample (red).

Once the desired cross term is separated, the data is then inverse Fourier transformed back to the frequency domain, shown in Figure 3.4.

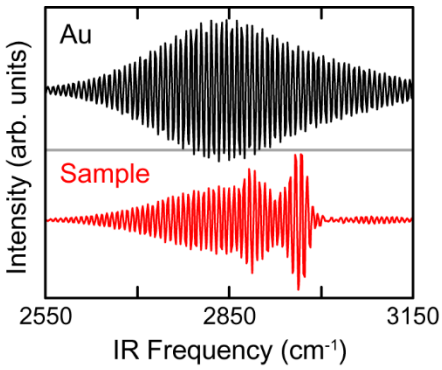

Figure 3.4 Imaginary component of the inverse fast Fourier transform of Au reference (black) and OTS sample (red) to the frequency domain.

The broad contributions from the homodyne LO and SFG signals are no longer present. Finally, the sample spectrum in Figure 3.4 is normalized to the Au signal to account for the IR envelope and provide a reference for the absolute phase, resulting in the HD-SFG spectra shown in Figure 3.5.

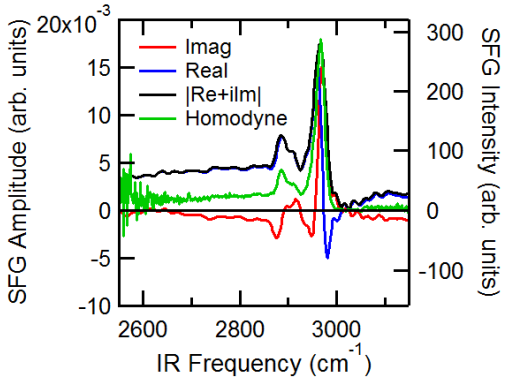

Figure 3.5 Heterodyne-detected SFG spectra: Imaginary component (red), real component (blue), and square-root of magnitude squared data (black) versus the SFG amplitude, and homodyne-detected data (green) versus SFG intensity. Data was collected in the *ppp* polarization combination.

The imaginary component of the HD-SFG data is the absorptive term containing peaks at molecular resonances, while the real component is the dispersive term.

While all of the data presented did not require any corrections to account for phase drift during or between scans, a phase factor of $e^{i\varphi}$ was introduced in the sample term to correct for slight phase variations when switching from the Au reference to the sample. This slight phase shift is caused by small differences in the sample position compared to the reference. The need for this correction was minimized, albeit not eliminated, by depositing the Au reference directly on the same surface as the monolayer allowing for switching between sample and reference by simply vertically translating the window by a few millimeters. When studying the front surface, depicted in Fig. 3.6, Au collected on the front was used as the reference. Analogously, when studying buried dry (solvated) surfaces, the buried dry (solvated) Au signal from

the back side of the window – collected immediately prior to collecting the sample signal – is used. Simply put, the Au signal collected in exactly the same conditions is used as the reference for the sample, ensuring a precise reference phase. The introduced phase term was set such that the imaginary component far from resonance was zero, consistent with literature procedure.[32,34] An alternative but analogous procedure for this correction is to introduce a phase such that the fringes of the reference and sample off-resonance overlap.[4] This process relies on an appreciable amount of nonresonant signal and was not used. As this well-ordered OTS model system has been studied previously[9,17] and our results are consistent with the literature, as discussed in detail later in this section, we can conclude that the phase of our Au reference is zero across the spectral region studied. A 180° degree phase was also included when considering the change in phase upon reflection of the SFG_{LO} depending on the polarization and refractive indices of the interfaces studied.

The square magnitude of the imaginary and real components overlap well with the homodyne-detected signal collected by simply blocking the LO, thereby validating the current method. Through the increased sensitivity in heterodyne detection, a number of additional peaks, for example in Fig. 3.5 at 2875 and 2960 cm^{-1}, clearly appear in the HD-SFG data that are obscured in the homodyne-detected data, illustrating the improved signal-to-noise of heterodyne detection in addition to the phase information.

Displayed in Figure 3.6 is the HD-SFG data collected for the OTS monolayer on fused silica at three different interfaces, schematically represented above the data,

and in both *ppp* (top row) and *ssp* (bottom row) polarization combinations.

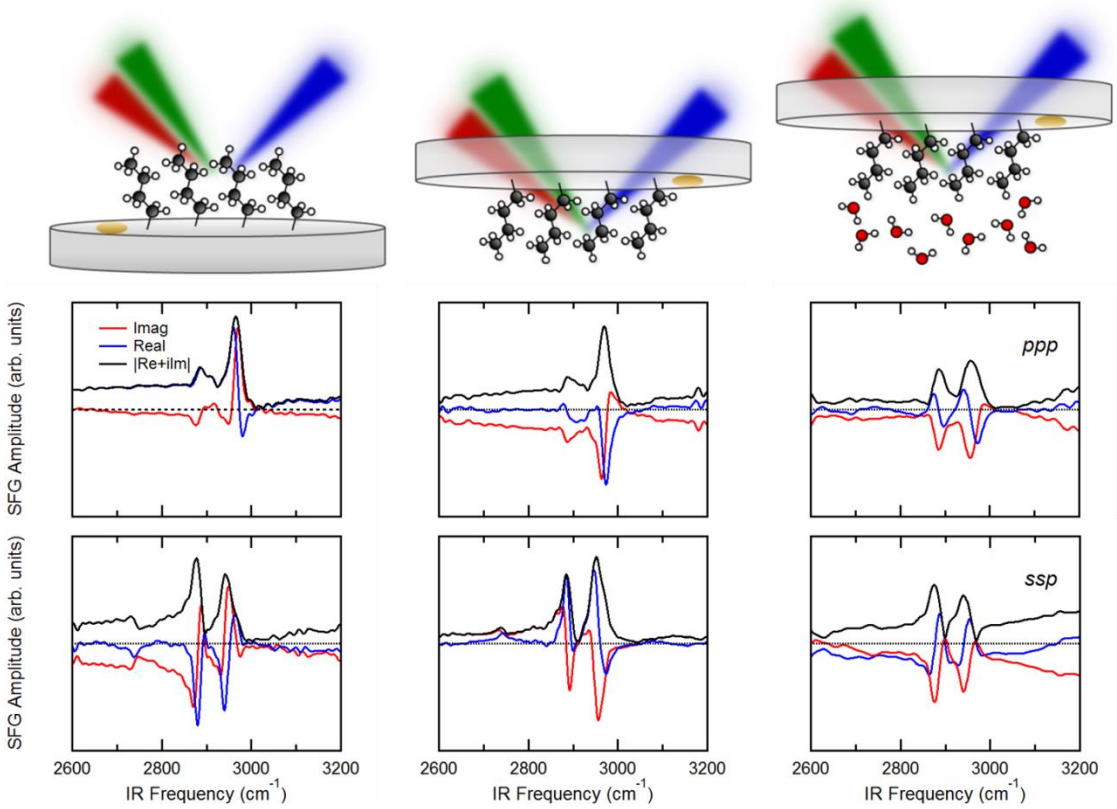

Figure 3.6 Heterodyne detected-SFG data of three OTS monolayer interfaces: air-monolayer-solid (left column), buried solid-monolayer-air (middle column), and buried solid-monolayer-water (right column). Data was collected in both *ppp* (top row) and *ssp* (bottom row) polarization combinations. Au thin film reference was deposited on the same surface as the monolayer.

The three cases studied here are the air-monolayer-solid substrate (left column), buried solid-monolayer-air (middle column), and buried solid-monolayer-water (right column) interfaces. Four peaks are clearly visible in the *ssp* polarization combination in the CH stretch region, and each surface was fit to these four peaks

corresponding to the CH_3 symmetric stretch (r+), the CH_2 asymmetric stretch (d-), the CH_3 Fermi-resonance of the bending overtone with r+ (r+FR), and the CH_3 asymmetric stretch (r-). The real and imaginary spectra were simultaneously fit to four Lorentzian peaks using a least-squares fit algorithm, the results of which are shown in Table 3.1 and compared to the HD-SFG results published previously for the dry front air-OTS surface observed using *ssp* polarized light.

Consistent with the previous homodyned SFG results from other groups,[35,43,44] the r+ and r- stretches are of opposite sign and r+ in oriented away from the solid substrate (negative sign). The CH_3 symmetric stretch on an ordered OTS monolayer is oriented away from the surface and exhibits a negative sign, which is the common convention used by many groups[17,19,21,34] but opposite the convention used by, for example, Shen et al.[9] As expected for a well-ordered monolayer, r+ and r+FR signals are most intense in *ssp*-polarization (bottom row), while r- is stronger in *ppp* (top row). The associated fits (Table 3.1) for the front surface correspond well to previous HD-SFG data of dry OTS on the front surface in *ssp* in terms of relative amplitude of the peaks, frequency, and linewidth.[9,17] Similar spectra were collected for the buried dry OTS surface in the middle column, however the signs are flipped- consistent with the absolute orientation of the molecules changing by 180°. To the best of our knowledge, this is the first example of broadband complex HD-SFG data of any buried interface.

For the buried OTS-water interface (right column), we observe the low frequency tail from the OH stretch at higher frequencies in *ssp*. Consistent with

previous reports of homodyne-detected SFG studied of solvated OTS monolayers, we see a slight red-shift of the r+ and r+FR modes when solvated due to the change in dielectric environment.[35] Additionally, we observe that the relative intensities of r+, r+FR, and d- all increase in *ppp* when solvated due to a change in the overall monolayer orientation. We do not observe significant changes to the linewidths of the solvated monolayers compared to the dry monolayers, suggesting that the solvation does not lead to significant inhomogeneous broadening. This lack of broadening is likely due to the hydrophobic nature of the interface that limits the interactions between water and the monolayer. The main advantage of heterodyne detection is exemplified by the enhanced detail shown in the solvated *ssp* and *ppp* fitted data (Figure 3.6). In particular, when the monolayer is in contact with water, the increase in the amplitude of the CH_2 asymmetric mode when solvated indicates a subtle increase in the disorder of the monolayer due to more gauche defects in which the CH_2 modes would not cancel. This change is not clear in the homodyne data.[35] The data exemplifies the versatility of the presented technique and its applicability for a broad range of systems and polarization combinations. This ability to probe buried surfaces will be particularly useful when studying complex systems, such as adsorbed proteins and peptides in contact with aqueous environments.

To further extend the capabilities of HD-SFG, we incorporated XP-HD-SFG, as a variation of balanced-detected HD-SFG. This technique involves simultaneously measuring SFG_{LO} +/- SFG_{sample} combinations, as discussed in further detail below. Balanced detected HD-SFG was demonstrated previously by Laaser et al.,[45] where the

two SFG_{LO} +/- SFG_{sample} combinations were spatially separated using a cube polarizer. This design had a phase stability of 1.5°/min and allowed for scans to be averaged over several minutes. In using a beam displacer in our design, the SFG_{LO} +/- SFG_{sample} combinations travel through all common optics leading to a simpler implementation and overall improved phase stability.

The collimation between the parabolic mirrors allows for control of both the polarization and timing of the individual beams. Following the scheme of the lower panel of Figure 3.1, the CCD chip images constructive interference between the SFG_{LO} beam and the SFG_{sample} beam in one region, while imaging destructive interference in the other region at a given frequency. The signals binned in the two separate regions on the CCD are shown for the interference between SFG_{LO} from ZnO and $SFG_{reference}$ from Au in the top left panel of Figure 3.7. A thin delay plate, and hence a small $\Delta\tau$, was used for this data to highlight the opposite fringe phase.

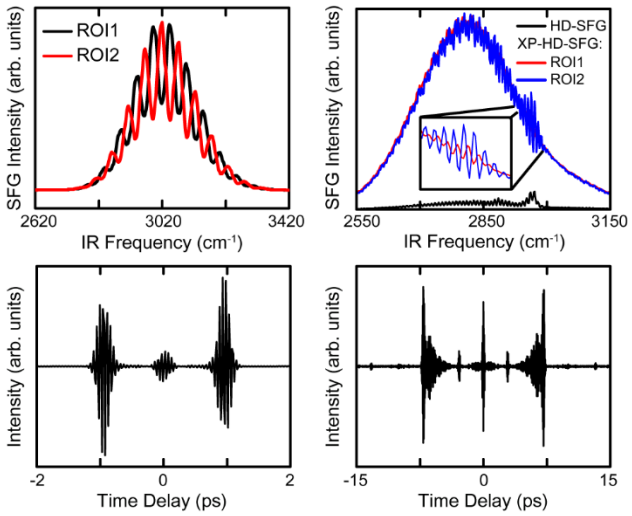

Figure 3.7 Top left: Cross-polarized heterodyne-detected SFG data of two regions of interest on the detector for the Au reference interfering with SFG_{LO}. Bottom Left: Fourier transform of the difference between the two regions of interest in the top left panel. Top right: Comparison of the interference signal collected for OTS on fused silica in *ppp* polarization using XP-HD-SFG (red and blue) compared to the same collected with HD-SFG (black) shown on the same scale. Bottom right: Fourier transform of the difference between the two regions of interest in the XP-HD-SFG data in the top right panel.

Performing an FFT of the difference of the two regions in the top panels of Figure 3.7 displays a significantly reduced homodyne contribution at time zero, shown in the bottom panels of Figure 3.7. The data analysis for XP-HD-SFG follows that of HD-SFG from this point, with windowing still being necessary to completely remove the homodyne contribution.

XP-HD-SFG broadens the capabilities of traditional HD-SFG to include the study of any polarization combination. Particularly for buried surfaces in contact with

water, the reflection of *p*-polarized SFG_{LO} light at the sample can be quite low. The SFG_{LO} is rotated to *s*-polarized light, improving the reflectivity off of the sample. The top right panel of Figure 3.7 compares the interference of OTS on fused silica collected with HD-SFG (*p*-polarized SFG_{LO}) to the same collected with XP-HD-SFG (*s*-polarized SFG_{LO}). In the latter case, the SFG_{LO} signal is stronger due to the stronger reflection with the polarization flip. This technique will allow for the determination of HD-SFG of any interface in which the *p*-polarized SFG_{LO} reflectivity is too low to collect with HD-SFG or the SFG_{sample} signal strength is very low and a stronger LO field is needed to increase the signal-to-noise ratio.

Incorporating two parabolic mirrors, rather than the single spherical mirror used by others, allows for easy expansion and customization of the HD-SFG technique. The time delay between SFG_{LO} and SFG_{sample} can be increased or decreased readily as there is sufficient spatial separation and collimation of the beams over the entire distance between the parabolic mirrors, and placing optics into the collimated beams does not affect the pointing. An appropriate amount of material delaying the SFG_{LO} from SFG_{sample} is critical for accurate data, as discussed in the following paragraphs. With the LO generating material placed before the sample, the FID of the vibrational mode decays towards zero time delay, as shown initially in the bottom panel of Figure 3.3 and also in Figure 3.8.

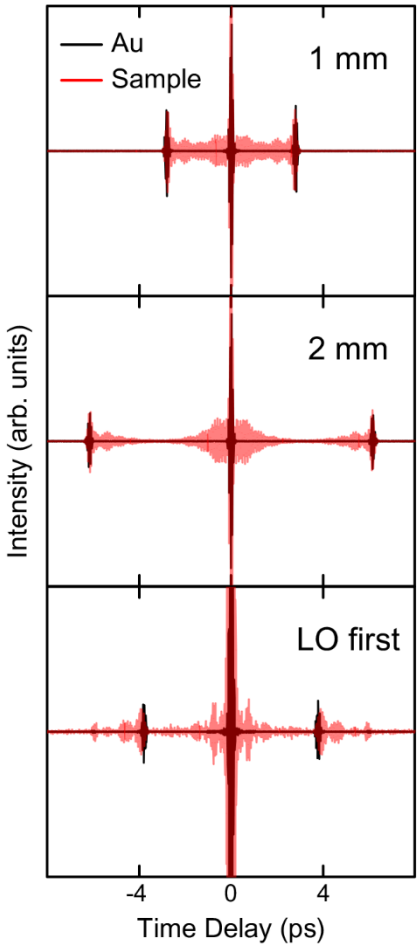

Figure 3.8 Comparison of time delay introduced by 1 mm SiO_2 in SFG_{LO} (top), 2 mm SiO_2 in SFG_{LO} (middle), and 2 mm KBr in visible and IR beams (bottom).

The center panel shows the imaginary component the data after FFT that was collected with 2 mm of fused silica as the delay plate in the SFG_{LO} beam, which introduced a 6.2 ps time delay between the SFG_{LO} and SFG_{sample}. The FID is well separated from the homodyne contribution at zero time delay. However, the top panel displays the same data collected with 1 mm fused silica as the delay plate. There is no clear division between homodyne and heterodyne components, and windowing cannot be used to isolate the two. Furthermore, the fringe spacing is inversely related to the time

delay. This constrains the time delay to be only as long as the narrowing fringes can be resolved. The use of the parabolic mirrors allows for the addition of KBr windows with minimal dispersion in the visible and IR beams, thereby delaying the SFG_{sample} with respect to the SFG_{LO}. This reverses the direction of the FID and allows for straightforward separation, shown in the bottom panel of Figure 3.8. This technical advance is particularly important for studying systems which exhibit vibrational modes with long free induction decays, being molecules with narrow vibrational features.

The importance of situating the LO-generating material before the sample has been explored previously by Pool et al.[20] The absorptivity and reflectivity of the sample is nearly wavelength independent in the narrow SFG wavelength range as compared to the broad span of the IR, especially when studying an aqueous interface. Thus the spectrum is not distorted between sample and reference in the LO-first geometry. Traditionally, $LiNbO_3$ or y-cut quartz have been used to generate the LO. The first material suffers from narrow phase-matching conditions, and therefore cannot be easily used for very broad IR applications. In our experience using y-cut quartz, the $SFG_{LO(qtz)}$ intensity and spectral profile varies with position in the focus and the visible beam polarization (*s*- or *p*- for *ssp* and *ppp* experiments, respectively) and required rotation by 90° to study the two different polarization combinations. Also, y-cut quartz required the use of a neutral density (ND) filter as the delay plate, because the generated SFG intensity was significantly higher than the Au reference and saturated the detector during normal sample acquisition times. Thus one would

need to determine the proper strength and thickness of an ND filter for a given sample and then return to Au to collect the reference with the same ND filter, i.e. same $\Delta\tau$. Rotation of the y-cut quartz to reduce the intensity introduced artifacts such as changing the spectral profile of the LO. Additionally, quartz strongly absorbs below 2100 cm^{-1}, interfering with the ability to collect HD-SFG data in that spectral region.

In the present study, we used 150 nm thin film ZnO deposited on glass to generate the LO, the FTIR absorbance spectrum of which is shown in Figure 3.9. The spectral profile of this substrate was found to be invariant as a function of polarization, and the intensity could be tuned by translating through the focus to be on the order of the intensity of our Au reference. This flexibility eliminates the need to adjust any optics when changing polarization combination or when collecting data for the reference and the sample. HD-SFG spectra showed identical features whether using ZnO or y-cut quartz as the LO generating material. The ZnO thin film can also potentially be used as a reference for both *ssp* and *ppp*, rather than either Au (used for *ppp*) or z-cut quartz (used for *ssp*) and can be deposited directly on a solid substrate by sputter deposition. The transmission of the ZnO film is greatly improved by depositing on CaF_2, facilitating HD-SFG down to ~1000 cm^{-1}, as shown in Figure 3.9. We have tested ZnO on CaF_2 for both generating the LO and acting as the reference, which has been found to produce identical data to ZnO on glass.

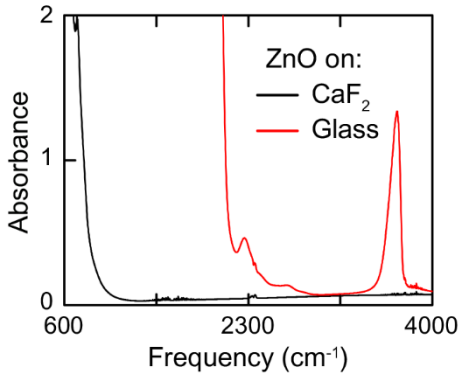

Figure 3.9 Infrared absorbance spectrum of 150 nm ZnO thin film on CaF2 (black) and glass (red).

Another advantage of the present geometry, in line with a number of other HD-SFG setups, is the ease of switching back to homodyne-detected SFG. In order to collect homodyne-detected SFG data, the SFG_{LO} is simply blocked between the parabolic mirrors. Analogously, the IR or visible beam is blocked after the LO to collect only the homodyne SFG_{LO} signal. Thus both homodyne and heterodyne SFG data can be collected in the exact same geometry and compared directly. While this comparison can be achieved in other HD-SFG designs, the collimated space created between the parabolic mirrors in our design makes this switch particularly easy.

An additional benefit of the current geometry is the use of the LO signal as an alignment tool for the sample. A HeNe reflection into the far field ensures the sample is reproducibly set at the same angle with respect to the plane of incidence of the input beams. Meanwhile, the vertical position of the SFG signal on the CCD chip from a sample when compared to Au is used to determine the correct position of the sample with respect to the beam overlap. Alternatively, a displacement sensor can be used.[8] In

our design, the SFG_{LO} reflection from the sample onto the CCD chip can be used to confirm the correct sample position, especially useful when the SFG_{sample} signal is weak and requires long integration times to determine the position on the chip. Furthermore, if the signal at the sample is lost during the course of a homodyne experiment, a thin piece of $LiNbO_3$ or y-cut quartz can be added to the LO position to verify spatial and temporal overlap easily without removing the sample since the SFG signal from both crystals is visible by eye.

In addition to the added versatility, the incorporation of parabolic mirrors and directing all of the beams with common optics greatly improves the phase stability between LO position and sample. The current experimental geometry had a high enough phase stability over the course of the data collection time of ~15 minutes per interface to eliminate the need to phase the individual scans before averaging, as discussed previously. A narrow section of the HD-SFG signal of Au taken every hour for 12 hours without a cover over the setup is shown in the top panel of Figure 3.10. Covering the optical table reduced disturbances introduced by air currents and further increased the phase stability, as displayed in the middle panel, with data collected every 30 minutes for 12 hours.

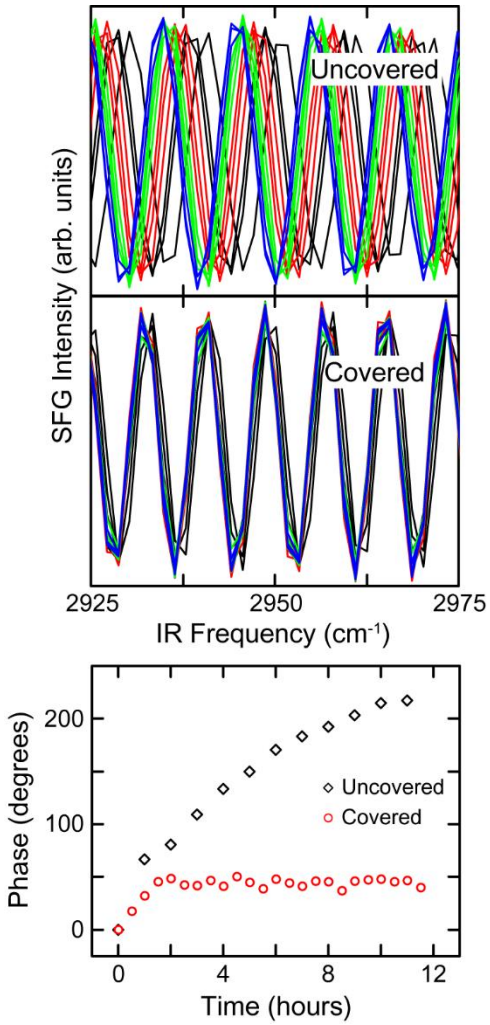

Figure 3.10 Heterodyne detected-SFG spectra collected once every hour while uncovered (top) and once every thirty minutes while covered (middle) for twelve hours. Comparison of the phase shift for the two cases (bottom).

When covered, the phase shift in the interference pattern is negligible for over 10 hours after an initial 2 hour equilibration period after containing the setup, shown in the bottom panel of Figure 3.10. This enhanced phase stability is imperative for collecting long scans such as is necessary for time-resolved HD-SFG and 2D-HD-SFG experiments. The present technique would be easy to incorporate in most SFG setups,

including horizontal sample geometries. While we use a vertical sample geometry with flat windows, we are currently extending this technique to work with buried solvated interfaces with prisms, which have been shown to significantly enhance the spectrum of water in these environments.[46]

3.4 Fitting Parameters

The real and imaginary components of the data presented in the main text in Figure 3.6 were simultaneously fit to a sum of four Lorentzian peaks without boundary conditions:

$$Re\left(\chi^{(2)}_{HD-SFG}(\omega_{IR})\right) = A_{NR} + \sum_k \frac{A_k(\omega_k - \omega_{IR})}{(\omega_k - \omega_{IR})^2 + \Gamma_k^2} \tag{3.4}$$

$$Im\left(\chi^{(2)}_{HD-SFG}(\omega_{IR})\right) = \sum_k \frac{A_k\Gamma_k}{(\omega_k - \omega_{IR})^2 + \Gamma_k^2} \tag{3.5}$$

where A is peak amplitude, ω is peak frequency, and Γ is the associated peak linewidth. The fit parameters are presented in Table 3.1 at the 95% confidence interval. While others[9,17] fit HD-SFG data of the dry OTS surface to six features, increasing the number of CH resonances could not be justified in our data. This is likely due to the high order of the OTS monolayer in the present study. The resonances we fit correspond to the r+ (CH_3 symmetric), d- (CH_2 asymmetric), r+FR (CH_3 symmetric + Fermi Resonance), and r- (CH_3 asymmetric). For the case of buried solvated OTS in *ssp*, we have also included a peak for the OH stretch. With the fit parameters determined in Table 3.1, the reconstructed norm-square fit can be compared to the data.

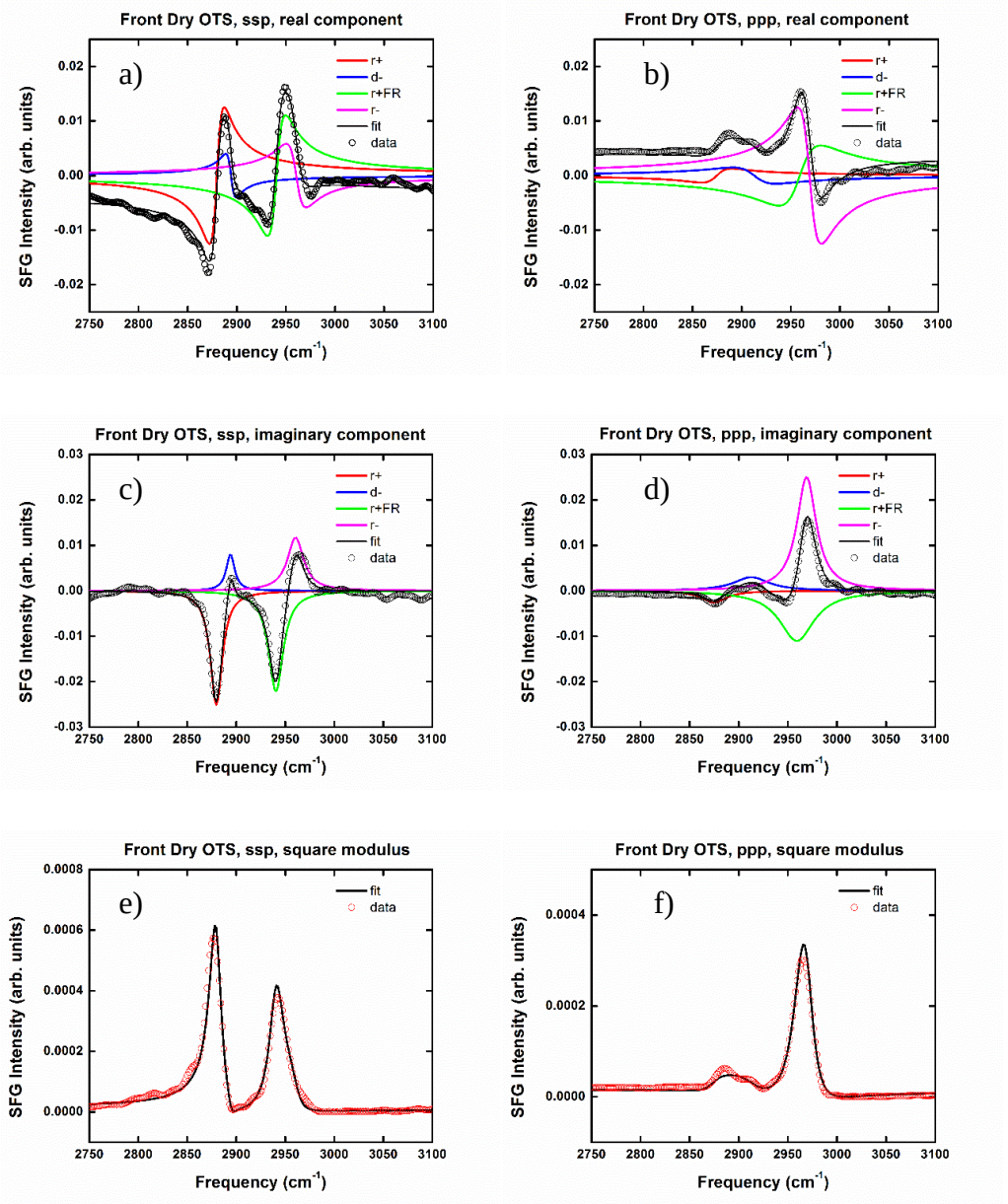

Figure 3.11 Fit results for the dry front OTS surface in *ssp*: a) real, c) imaginary, and e) square modulus and *ppp*: b) real, d) imaginary, and f) square modulus.

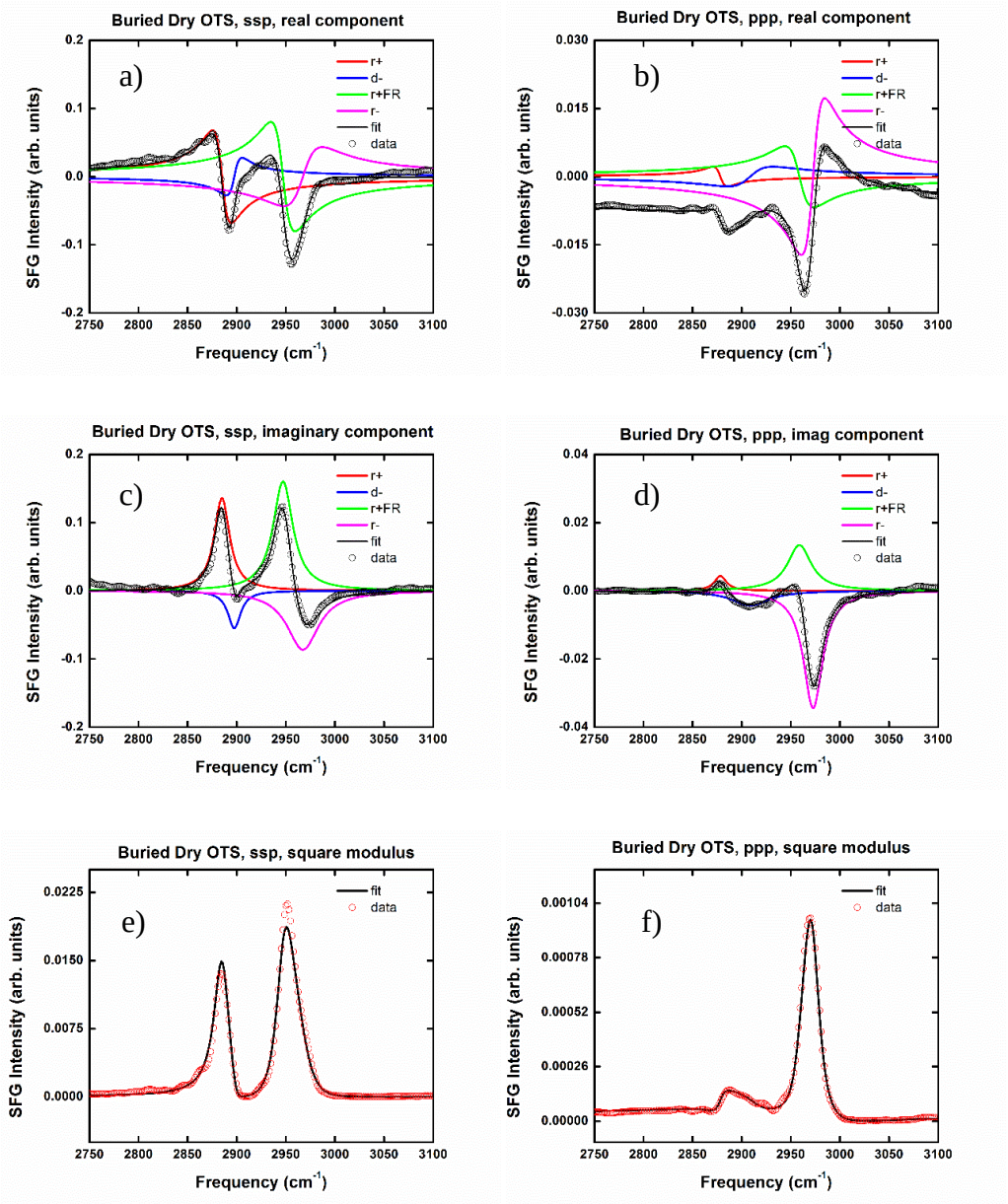

Figure 3.12 Fit results for the dry buried OTS surface in *ssp*: a) real, c) imaginary, and e) square modulus and *ppp*: b) real, d) imaginary, and f) square modulus.

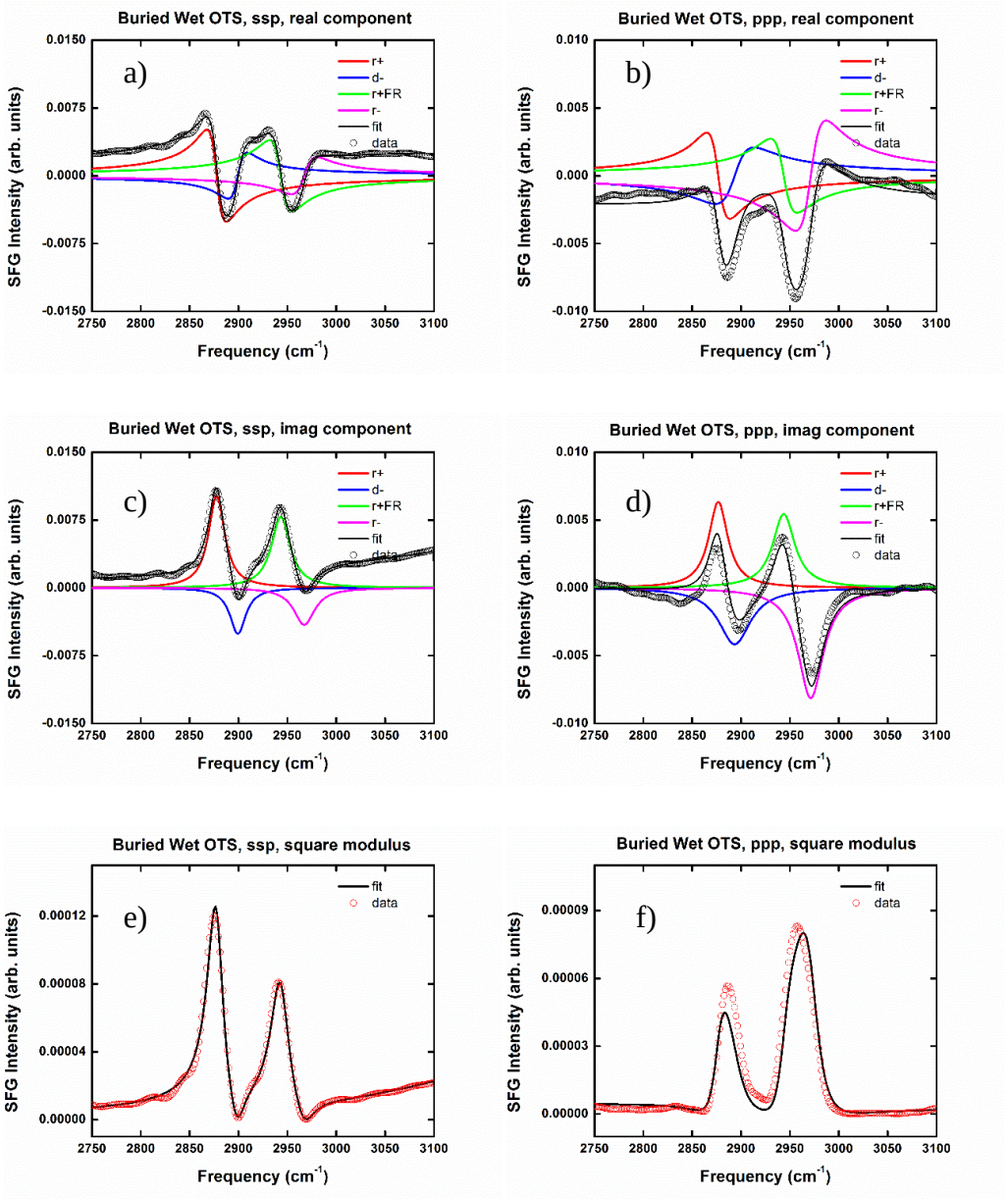

Figure 3.13 Fit results for the solvated buried OTS surface in *ssp*: a) real, c) imaginary, and e) square modulus and *ppp*: b) real, d) imaginary, and f) square modulus.

		Front Dry OTS			Buried Dry OTS		Buried Solvated OTS	
		Shen[9], Hore[17]	ssp	ppp	ssp	ppp	ssp	ppp
r+	A_1	-5.0, -3.6	-0.186 ± 0.010	-0.040 ± 0.021	1.30 ± 0.17	0.033 ± 0.009	0.102 ± 0.003	0.075 ± 0.053
	ω_1	2873, 2879	2879.7 ± 0.3	2874.7 ± 3.3	2884.9 ± 0.7	2878.3 ± 0.75	2877.6 ± 0.17	2876.7 ± 1.93
	Γ_1	5.5, 5.4	7.4 ± 0.4	15.6 ± 5.7	9.5 ± 0.7	7.6 ± 1.7	10.0 ± 0.3	11.8 ± 3.7
d-	A_2	1.6, 0.72	0.042 ± 0.009	0.065 ± 0.043	-0.439 ± 0.162	-0.101 ± 0.024	-0.050 ± 0.003	-0.083 ± 0.064
	ω_2	2883, 2889	2894.1 ± 0.6	2912.8 ± 3.9	2897.5 ± 1.3	2908.6 ± 2.1	2899.3 ± 0.3	2893.5 ± 7.9
	Γ_2	6.6, 5.2	5.2 ± 1.1	21.7 ± 11.2	7.9 ± 1.7	23.2 ± 4.7	9.8 ± 0.6	19.9 ± 6.0
r+FR	A_3	-7.5, -5.2	-0.201 ± 0.014	-0.237 ± 0.123	1.97 ± 0.25	0.200 ± 0.069	0.091 ± 0.004	0.075 ± 0.019
	ω_3	2935, 2942	2940.5 ± 0.4	2959.2 ± 5.7	2947.1 ± 0.5	2958.7 ± 2.1	2943.2 ± 0.3	2943.7 ± 1.3
	Γ_3	9.5, 9.1	9.1 ± 0.6	21.5 ± 3.3	12.3 ± 0.9	14.7 ± 2.0	11.6 ± 0.4	13.7 ± 2.7
r-	A_4	3.1, 2.2	0.118 ± 0.014	0.302 ± 0.127	-1.702 ± 0.285	-0.409 ± 0.058	-0.054 ± 0.004	-0.127 ± 0.015
	ω_4	2958, 2962	2960.5 ± 0.7	2969.1 ± 0.9	2967.4 ± 2.0	2972.7 ± 0.5	2967.2 ± 0.6	2971.3 ± 1.1
	Γ_4	11.9, 12	10.1 ± 1.1	12.1 ± 1.7	19.7 ± 1.6	11.9 ± 0.6	13.0 ± 0.9	15.6 ± 1.4
NR		0.10, -0.040	-0.0034 ± 0.0001	0.0035 ± 0.0001	0.0032 ± 0.0007	-0.0057 ± 0.0001	-0.0008 ± 0.0001	-0.0019 ± 0.0001
OH stretch	A_5						1.61 ± 0.09	
	ω_5						3297.5 ± 14.1	
	Γ_5						219.8 ± 9.9	

Table 3.1 Fitting results for three interfaces studied in *ssp* and *ppp* polarization combinations: A (amplitude, arb. units), ω (frequency, cm^{-1}), and Γ (linewidth, cm^{-1}) for four CH stretching resonances: r+ (CH_3 symmetric), d- (CH_2 asymmetric), r+FR (CH_3 symmetric + Fermi Resonance), r- (CH_3 asymmetric), and OH stretch for solvated OTS in *ssp*. All errors are given at 95% confidence level.

3.5 Conclusions

We demonstrate an improved design for HD-SFG which is exceedingly stable, versatile, easily integrated into conventional SFG designs, and extends the technique to be capable of probing diverse interfaces in any polarization combination through XP-HD-SFG. The results presented are representative of the different systems, including solid-air and buried solid-liquid interfaces, and the polarization combinations which can be studied. HD-SFG determines the complex nonlinear susceptibility $\chi^{(2)}$ rather than $|\chi^{(2)}|^2$ measured in homodyne-detected SFG, allowing absolute phase determination and enhanced signal-to-noise ratio. Using a model system of an OTS monolayer, we present the first broadband HD-SFG spectrum of a buried surface, which provided a higher level of detail about the molecular structure than observed in previous homodyne detected spectra. Polarization and timing control of all of the electric fields involved is possible through the use of a pair of parabolic mirrors that create a path in which the beams are collimated and spatially separated. ZnO as a local-oscillator-generating material is critical for effortlessly switching from *ppp* to *ssp* polarization combinations with no other changes necessary. All of these improvements have been incorporated with higher phase stability than has been previously achieved. Since the daily operations of this design are no more challenging than conventional SFG, the present design provides broad implementation of HD-SFG and the ability to obtain HD-SFG spectra of any interface in any polarization.

*Adapted from H. Vanselous and P. B. Petersen *J. Phys. Chem. C* 2016, 120, 8175–

8184

3.6 References

(1) Shen, Y. R. *The Principles of Nonlinear Optics*; Wiley-Interscience: New York, 1984.

(2) Boyd, R. W. *Nonlinear Optics*, Third.; Elsevier Inc.: Burlington, 2008.

(3) Moad, A. J.; Simpson, G. J. A Unified Treatment of Selection Rules and Symmetry Relations for Sum-Frequency and Second Harmonic Spectroscopies. *J. Phys. Chem. B* **2004**, *108*, 3548–3562.

(4) Stiopkin, I. V; Jayathilake, H. D.; Bordenyuk, A. N.; Benderskii, A. V. Heterodyne-Detected Vibrational Sum Frequency Generation Spectroscopy. *J. Am. Chem. Soc.* **2008**, *130*, 2271–2275.

(5) Rao, Y.; Comstock, M.; Eisenthal, K. B. Absolute Orientation of Molecules at Interfaces. *J. Phys. Chem. B* **2006**, *110*, 1727–1732.

(6) Fu, L.; Chen, S.-L.; Wang, H.-F. Validation of Spectra and Phase in Sub-1 cm^{-1} Resolution Sum-Frequency Generation Vibrational Spectroscopy through Internal Heterodyne Phase-Resolved Measurement. *J. Phys. Chem. B* **2015**.

(7) Superfine, R.; Huang, J. Y.; Shen, Y. R. Phase Measurement for Surface Infrared-Visible Sum-Frequency Generation. *Opt. Lett.* **1990**, *15*, 1276–1278.

(8) Nihonyanagi, S.; Kusaka, R.; Inoue, K.; Adhikari, A.; Yamaguchi, S.; Tahara, T. Accurate Determination of Complex $\chi^{(2)}$ Spectrum of the Air/water Interface. *J. Chem. Phys.* **2015**, *143*, 124707.

(9) Ji, N.; Ostroverkhov, V.; Chen, C. Y.; Shen, Y. R. Phase-Sensitive Sum-Frequency Vibrational Spectroscopy and Its Application to Studies of Interfacial Alkyl Chains. *J. Am. Chem. Soc.* **2007**, *129*, 10056–10057.

(10) Jena, K. C.; Covert, P. A.; Hore, D. K. Phase Measurement in Nondegenerate Three-Wave Mixing Spectroscopy. *J. Chem. Phys.* **2011**, *134*, 44712.

(11) Zhang, L.; Tian, C.; Waychunas, G. A.; Shen, Y. R. Structures and Charging of α-Alumina (0001)/Water Interfaces Studied by Sum-Frequency Vibrational Spectroscopy. *J. Am. Chem. Soc* **2008**, *130*, 7686–7694.

(12) Zhang, L.; Singh, S.; Tian, C.; Shen, Y. R.; Wu, Y.; Shannon, M. A.; Brinker, C. J. Nanoporous Silica-Water Interfaces Studied by Sum-Frequency Vibrational Spectroscopy. *J. Chem. Phys.* **2009**, *130*, 154702.

(13) Tian, C. S.; Shen, Y. R. Structure and Charging of Hydrophobic Material/water Interfaces Studied by Phase-Sensitive Sum-Frequency Vibrational Spectroscopy. *Proc. Natl. Acad. Sci.* **2009**, *106*, 15148–15153.

(14) Ji, N.; Ostroverkhov, V.; Tian, C. S.; Shen, Y. R. Characterization of Vibrational Resonances of Water-Vapor Interfaces by Phase-Sensitive Sum-Frequency Spectroscopy. *Phys. Rev. Lett.* **2008**, *100*, 96102.

(15) Tian, C.; Byrnes, S. J.; Han, H. L.; Shen, Y. R. Surface Propensities of Atmospherically Relevant Ions in Salt Solutions Revealed by Phase-Sensitive Sum Frequency Vibrational Spectroscopy. *J. Phys. Chem. Lett.* **2011**, *2*, 1946–1949.

(16) Jena, K. C.; Covert, P. A.; Hall, S. A.; Hore, D. K. Absolute Orientation of

Ester Side Chains on the PMMA Surface. *J. Phys. Chem. C* **2011**, *115*, 15570–15574.

(17) Covert, P. A.; Fitzgerald, W. R.; Hore, D. K. Simultaneous Measurement of Magnitude and Phase in Interferometric Sum-Frequency Vibrational Spectroscopy. *J. Chem. Phys.* **2012**, *137*, 14201.

(18) Yamaguchi, S.; Tahara, T. Heterodyne-Detected Electronic Sum Frequency generation: "Up" versus "down" alignment of Interfacial Molecules. *J. Chem. Phys.* **2008**, *129*, 1–4.

(19) Nihonyanagi, S.; Yamaguchi, S.; Tahara, T. Direct Evidence for Orientational Flip-Flop of Water Molecules at Charged Interfaces: A Heterodyne-Detected Vibrational Sum Frequency Generation Study. *J. Chem. Phys.* **2009**, *130*, 204704.

(20) Pool, R. E.; Versluis, J.; Backus, E. H. G.; Bonn, M. Comparative Study of Direct and Phase-Specific Vibrational Sum-Frequency Generation Spectroscopy: Advantages and Limitations. *J. Phys. Chem. B* **2011**, *115*, 15362–15369.

(21) Mondal, J. A.; Nihonyanagi, S.; Yamaguchi, S.; Tahara, T. Structure and Orientation of Water at Charged Lipid Monolayer/water Interfaces Probed by Heterodyne-Detected Vibrational Sum Frequency Generation Spectroscopy. *J. Am. Chem. Soc.* **2010**, *132*, 10656–10657.

(22) Chen, X.; Hua, W.; Huang, Z.; Allen, H. C. Interfacial Water Structure Associated with Phospholipid Membranes Studied by Phase-Sensitive

Vibrational Sum Frequency Generation Spectroscopy. *J. Am. Chem. Soc* **2010**, *132*, 11336–11342.

(23) Nihonyanagi, S.; Yamaguchi, S.; Tahara, T. Water Hydrogen Bond Structure near Highly Charged Interfaces Is Not like Ice. *J. Am. Chem. Soc.* **2010**, *132*, 6867–6869.

(24) Hua, W.; Chen, X.; Allen, H. C. Phase-Sensitive Sum Frequency Revealing Accommodation of Bicarbonate Ions, and Charge Separation of Sodium and Carbonate Ions within the Air/water Interface. *J. Phys. Chem. A* **2011**, *115*, 6233–6238.

(25) Hua, W.; Jubb, A. M.; Allen, H. C. Electric Field Reversal of Na_2SO_4, $(NH_4)_2SO_4$, and Na_2CO_3 Relative to $CaCl_2$ and NaCl at the Air/Aqueous Interface Revealed by Heterodyne Detected Phase-Sensitive Sum Frequency. *J. Phys. Chem. Lett.* **2011**, *2*, 2515–2520.

(26) Mondal, J. A.; Nihonyanagi, S.; Yamaguchi, S.; Tahara, T. Three Distinct Water Structures at a Zwitterionic Lipid/Water Interface Revealed by Heterodyne-Detected Vibrational Sum Frequency Generation. *J. Am. Chem. Soc* **2012**, *134*, 7842–7850.

(27) Nihonyanagi, S.; Singh, P. C.; Yamaguchi, S.; Tahara, T. Ultrafast Vibrational Dynamics of a Charged Aqueous Interface by Femtosecond Time-Resolved Heterodyne-Detected Vibrational Sum Frequency Generation. *Bull. Chem. Soc. Jpn.* **2012**, *85*, 758–760.

(28) Singh, P. C.; Nihonyanagi, S.; Yamaguchi, S.; Tahara, T. Interfacial Water in

the Vicinity of a Positively Charged Interface Studied by Steady-State and Time-Resolved Heterodyne-Detected Vibrational Sum Frequency Generation. *J. Chem. Phys.* **2014**, *141*, 18C527.

(29) Stiopkin, I. V; Weeraman, C.; Pieniazek, P. A.; Shalhout, F. Y.; Skinner, J. L.; Benderskii, A. V. Hydrogen Bonding at the Water Surface Revealed by Isotopic Dilution Spectroscopy. *Nature* **2011**, *474*, 192–195.

(30) Chen, X.; Allen, H. C. Water Structure at Aqueous Solution Surfaces of Atmospherically Relevant Dimethyl Sulfoxide and Methanesulfonic Acid Revealed by Phase-Sensitive Sum Frequency Spectroscopy. *J. Phys. Chem. B* **2010**, *114*, 14983–14988.

(31) Okuno, M.; Ishibashi, T. Heterodyne-Detected Achiral and Chiral Vibrational Sum Frequency Generation of Proteins at Air/Water Interface. *J. Phys. Chem. C* **2015**, *119*, 9947–9954.

(32) Watanabe, K.; Inoue, K. I.; Nakai, I. F.; Matsumoto, Y. Nonadiabatic Coupling between C-O Stretching and Pt Substrate Electrons Enhanced by Frustrated Mode Excitations. *Phys. Rev. B - Condens. Matter Mater. Phys.* **2010**, *81*, 241408.

(33) Anfuso, C. L.; Xiao, D.; Ricks, A. M.; Negre, C. F. A.; Batista, V. S.; Lian, T. Orientation of a Series of CO_2 Reduction Catalysts on Single Crystal TiO_2 Probed by Phase-Sensitive Vibrational Sum Frequency Generation Spectroscopy (PS-VSFG). *J. Phys. Chem. C* **2012**, *116*, 24107–24114.

(34) Ge, A.; Peng, Q.; Qiao, L.; Yepuri, N. R.; Darwish, T. A.; Matsusaki, M.;

Akashi, M.; Ye, S. Molecular Orientation of Organic Thin Films on Dielectric Solid Substrates: A Phase-Sensitive Vibrational SFG Study. *Phys. Chem. Chem. Phys.* **2015**, *17*, 18072–18078.

(35) Barrett, A.; Petersen, P. B. Order of Dry and Wet Mixed-Length Self-Assembled Monolayers. *J. Phys. Chem. C* **2015**, *119*, 23943–23950.

(36) Shen, Y. R. Phase-Sensitive Sum-Frequency Spectroscopy. *Annu. Rev. Phys. Chem.* **2013**, *64*, 129–150.

(37) Nihonyanagi, S.; Mondal, J. a; Yamaguchi, S.; Tahara, T. Structure and Dynamics of Interfacial Water Studied by Heterodyne-Detected Vibrational Sum-Frequency Generation. *Annu. Rev. Phys. Chem.* **2013**, *64*, 579–603.

(38) Yamaguchi, S. Development of Single-Channel Heterodyne-Detected Sum Frequency Generation Spectroscopy and Its Application to the Water/vapor Interface. *J. Chem. Phys.* **2015**, *143*, 34202.

(39) Xu, B.; Yajing, W.; Sun, D.; Dai, H.-L.; Rao, Y. Stabilized Phase Detection of Heterodyne Sum Frequency Generation for Interfacial Studies. *Opt. Lett.* **2015**, *40*, 4472–4475.

(40) McDermott, M. L.; Petersen, P. B. Robust Self-Referencing Method for Chiral Sum Frequency Generation Spectroscopy. *J. Phys. Chem. B* **2015**, *119*, 12417–12423.

(41) Calabrese, C.; Vanselous, H.; Petersen, P. B. Deconstructing the Heterogeneity of Surface-Bound Catalysts: Rutile Surface Structure Affects Molecular Properties. *J. Phys. Chem. C* **2016**, *120*, 1515–1522.

(42) Shen, Y. R. *The Principles of Nonlinear Optics*; John Wiley & Sons, Inc.: New York, 1984.

(43) Lü, R.; Gan, W.; Wu, B.; Zhang, Z.; Guo, Y.; Wang, H. C−H Stretching Vibrations of Methyl, Methylene and Methine Groups at the Vapor/Alcohol (N= 1−8) Interfaces. *J. Phys. Chem. B* **2005**, *109*, 14118–14129.

(44) Nihonyanagi, S.; Eftekhari-Bafrooei, A.; Borguet, E. Ultrafast Vibrational Dynamics and Spectroscopy of a Siloxane Self-Assembled Monolayer. *J. Chem. Phys.* **2011**, *134*, 84701.

(45) Laaser, J. E.; Xiong, W.; Zanni, M. T. Time-Domain SFG Spectroscopy Using Mid-IR Pulse Shaping: Practical and Intrinsic Advantages. *J. Phys. Chem. B* **2011**, *115*, 2536–2546.

(46) York, R. L.; Li, Y.; Holinga, G. J.; Somorjai, G. A. Sum Frequency Generation Vibrational Spectra: The Influence of Experimental Geometry for an Absorptive Medium or Media. *J. Phys. Chem. A* **2009**, *113*, 2768–2774.

CHAPTER 4

TWO DIMENSIONAL SFG OF NANOCRYSTALLINE TIO_2: INTERFEROMETRIC 2D SUM FREQUENCY GENERATION SPECTROSCOPY REVEALS STRUCTURAL HETEROGENEITY OF CATALYTIC MONOLAYERS ON TRANSPARENT MATERIALS*

4.1 Introduction

Heterogeneous chemistry drives numerous biological, chemical, and physical processes. Examples of such processes include reactions that occur in solutions at cell membranes, in gases at the surface of aerosol particles, and in solutions at hydrophobic and hydrophilic surfaces. Here, overall properties such as reaction efficiency and selectivity, are directly linked to molecular characteristics, including structure, dynamics, and energy transfer capabilities at the interface. However, characterizing interfacial properties of complex heterogeneous systems through spectroscopy is technically challenging as the response from the molecules in the bulk is typically much stronger than from the few molecules at the interface. As an important model system, we focus on a molecular CO_2 reduction catalyst covalently bound to nanostructured TiO_2. Photocatalytic and electrocatalytic reduction of CO_2 to liquid fuels, has been a high priority goal in response to the rise in atmospheric concentration of greenhouse gases and the need for environmentally friendly alternative energy sources.[1–3]

To make heterogeneous CO_2 catalysis viable, the catalyst is immobilized on a high surface area inorganic support, such as nanostructured TiO_2.[4–7] However, such systems exhibit a large structural heterogeneity due to the multitude of ways the catalyst can be bound to the substrate. The catalyst could be bound at a range of angles with respect to the surface, altering the strength of any molecule-surface interaction, or if the catalyst contains more than one anchoring group, it can bind through one or more of the anchoring groups, resulting in different orientations at the surface. To gain a fundamental understanding of the catalytic process and the ability to rationally design improved systems, model CO_2 reduction catalysts based on Re(2,2'-bipyridine)$(CO)_3Cl$ complexes have been studied on TiO_2 using a number of nonlinear spectroscopic methods.[8–15] For molecules that are not confined to a surface, separating the relatively few interfacial molecules from the bulk contribution is a challenge that can be overcome with surface-specific vibrational sum frequency generation (SFG) spectroscopy, in which a signal is only generated, within the dipole approximation, when inversion symmetry is broken, such as at an interface.[16–18] Technological developments in this field have led to the ability to determine absolute molecular orientation with heterodyne detection (HD-SFG)[19,20] and lifetimes of vibrational dynamics with time-resolved infrared (IR) pump – SFG probe experiments (TR-SFG)[21–27]. Recent advances in high-resolution SFG[28–30] provide the ability to perform detailed spectral decomposition and orientational analysis. However, a spectral lineshape, often a homogeneously broadened Lorentzian, has to be assumed. While discrete vibrational modes can be successfully fit to Lorentzian peaks, broad and

inhomogeneous features may not uniquely fit to a sum of Lorenztian peaks.

The orientation of catalysts at a surface will directly influence the reaction efficiency through the steric availability of the active site at the metal center, while the vibrational dynamics may affect the energy flow through the system. A 2D IR spectrum constitutes a correlation map between initial and induced frequencies after a sample is excited and the system is allowed to evolve for a finite time. The results reveal intramolecular vibrational coupling, anharmonicities, and spectral diffusion, further detailing the energy landscape of the system and characterizing the ultrafast dynamics. Spectral diffusion can distinguish structural and dynamic heterogeneities of bulk systems.[31,32] Bulk 2D IR experiments have been used to study interfacial systems where the molecules in question were bound to a surface[33,34] or through enhancement with, for example, a metal surface[35,36]. However, to study interfacial molecules where there is an appreciable bulk concentration, e.g. Gibbs monolayers or liquids, a truly surface-specific technique is needed. Different implementations of 2D IR spectroscopic methods vary in their time and frequency resolutions, which determine what systems and types of processes can be studied.

Several surface-specific analogues of bulk 2D IR spectroscopy have been recently developed. There are two general ways to implement this technique: narrowband pump-probe 2D SFG[37,38] and interferometric 2D SFG.[39,40] In narrowband pump-probe 2D SFG experiments, a narrow-band pump pulse is scanned across the frequency range of interest, while the transient broadband SFG spectrum is recorded. The time and frequency resolution of the experiment is restricted by the time-

bandwidth product of the pump pulse. Alternatively, two broadband pump pulses can be used to excite the sample while scanning the relative timing between them, resulting in an interferogram in the recorded broadband SFG spectrum that is then Fourier transformed to obtain the excitation axis. This interferometric 2D SFG method maintains high spectral resolution and produces the highest temporal resolution.[41–43] All prior studies performed on non-metallic surfaces were conducted in the narrowband pump-probe 2D SFG experimental configuration due to the comparatively more simple experimental design of varying the pump wavelength with a commercial optical parametric amplifier.

An important component of 2D SFG is the incorporation of heterodyne detection. Thus far, all interferometric 2D SFG experiments of resonant samples have been "self-heterodyned," i.e. the sample substrate studied was metallic and produced the local oscillator. Self-heterodyne detection limits the variety of interfaces that can be studied to only molecules at an air-metal interface. Schleeger et al.[44] implemented an external local oscillator in interferometric 2D SFG in a noncollinear geometry and obtained a 2D spectrum from a non-resonant GaAs sample. By incorporating an interfering pump pulse pair with our recent technical advances in long-term phase stable heterodyne-detected SFG[45] and time-resolved SFG, we are able to carry out the first interferometric 2D SFG spectroscopic measurements of a molecular system on a transparent (non-metallic) material. The methods used in the present study open up the technique to a wider array of systems than have previously been studied and can resolve dynamical and structural heterogeneity without assuming a specific lineshape.

Interferometric 2D SFG is a fourth-order nonlinear spectroscopy. Two broadband pump pulses create a vibrational excitation that is probed by an infrared probe pulse resonant with a vibrational transition overlapped in space and time with a visible upconversion pulse at the sample surface. The experimental geometry used here is shown in Figure 4.1a. An external local oscillator field, SFG_{LO}, is generated by focusing the IR probe and visible upconversion pulses on a nonlinear material- in this case an amorphous ZnO film coated on a CaF_2 window- before the sample. These three fields, IR, visible, and SFG_{LO}, are recombined at the sample where another field, SFG_{sample}, is generated. In our implementation of the interferometric 2D SFG experiment, the pump pulse pair is generated in a Mach-Zehnder interferometer.[46,47] Alternatively, the pump pair could be generated in a pulse shaper.[39] Further experimental details are provided in the Experimental Methods. The relative timing between the two pump pulses is varied (τ_1, Figure 4.1b) to generate the excitation axis upon Fourier transformation, and the time between pump and probe is varied (τ_2) to collect a series of 2D surfaces at different waiting times, which provides information on energy redistribution and relaxation. By incorporating a broadband interfering pump pair instead of frequency scanning a spectrally narrow pump, as is done in pump-probe 2D SFG, we can simultaneously obtain higher frequency and time resolution. It should be noted that each 2D SFG surface presented here was acquired in 8 hours. We did not utilize advanced methods used in 2D IR for noise reduction and decreasing acquisition time, including undersampling, phase cycling, and rotating reference frames, some of which require a pulse shaper, but these could be

incorporated for further improvement in the data quality or alternatively reduction of the acquisition time by an estimated 95%.[48]

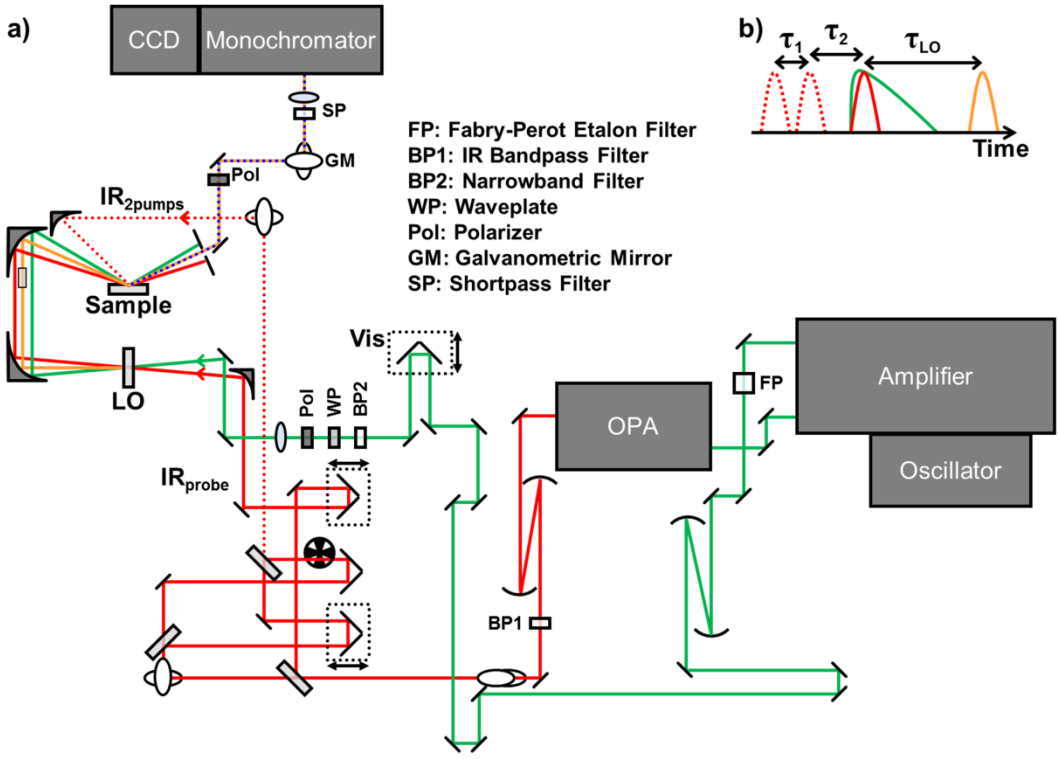

Figure 4.1 a) Interferometric 2D SFG experimental geometry. IR_{probe} (solid red) and visible (green) pulses are focused onto a local oscillator generating crystal (LO), where the external field (yellow) is generated. All three pulses are recombined at the sample and the LO is delayed by a transparent CaF_2 window. Interfering IR_{2pumps} (dashed red) pulses are overlapped with IR_{probe}, Vis, and LO fields at the sample where SFG (dashed blue) is generated and detected. b) Pulse sequence. IR_{2pumps} pulses are scanned in time (τ_1) to generate the pump axis. IR_{probe} is overlapped in time with Vis, and both are delayed with respect to the pump (τ_2). The LO is delayed further (τ_{LO}) by a CaF_2 delay plate (DP).

4.2 Experimental Methods

4.2.1 Sample Preparation

Re(4,4′-dicarboxyl-2,2′-bipyridine)$(CO)_3Cl$ was synthesized according to published literature procedure.[14] Nanostructured TiO_2 thin films were doctor bladed onto microscope slides from a slurry of 20 nm > 99% anatase TiO_2 nanoparticles (Sigma Aldrich, 791547) dispersed in a 6% acetic acid solution. The films were annealed at progressively higher temperatures up to 500°C according to published literature procedure.[49] The thin films were sensitized overnight in saturated $Re(CO)_3$ in ethanol and subsequently rinsed with excess ethanol.

4.2.2 Experimental Details

The experimental details for the HD-SFG,[45] IR-pump SFG-probe,[14] and 2D IR[46] setups have been described previously. For the 2D SFG experiment, the 800 nm (0.7 nm fwhm) 10 μJ visible, 1980 cm^{-1} (125 cm^{-1} fwhm) 5 μJ IR probe, and 6 μJ total (3 μJ in each) IR pump pair pulses were overlapped at the sample at 60°, 65°, and 55° with respect to the surface normal in the *ppppp* polarization combination (polarization of SFG, visible, IR probe, and each IR pump pulse, respectively). To collect 2D SFG data, the galvanometric mirror is synchronized with an optical chopper.[25] The chopper blocks every other pulse in one arm of the interferometer. Therefore, the signal corresponding to the pump-probe, in addition to the linear spectrum, is in one region of interest (ROI) on the CCD, while the 2D SFG signal is in the other region. Through this method, both laser fluctuations and sample degradation can be corrected for, as

discussed in Chapter 2, section 2.2.3. The τ_1 time is scanned by moving one translation stage in the interferometer with a step size of 3 fs, generating the pump axis. The spectral resolution in the probe axis is 10 cm^{-1}, set by the visible upconversion pulse, and 15 cm^{-1} in the excitation axis, determined by the length of time scanned in τ_1. To monitor dynamics, τ_2 is scanned by stepping both visible and IR translation stages by a finite amount relative to the stationary pump stage. HD data along the probe axis is analyzed[45] at each pump time, and then the pump axis undergoes Fourier transformation to the frequency domain at each probe frequency to generate a two-dimensional spectrum.

4.3 Results and Discussion

Here, 2D SFG is employed to study a model CO_2 reduction catalyst, Re(4,4′-dicarboxyl-2,2′-bipyridine)$(CO)_3Cl$ (abbreviated $Re(CO)_3$) bound to nanocrystalline TiO_2 , which has three IR active CO stretch modes (structure and FTIR in Figure 4.2a). The low frequency feature at 1920 cm^{-1} is a combination of the A′(2) antisymmetric stretch of the axial CO ligands with respect to the equatorial CO ligands and the A″ antisymmetric stretch of the equatorial carbonyls. The high frequency mode at 2048 cm^{-1} is the A′(1) symmetric stretch of the three CO ligands. All three of these modes are SFG active on nanostructured TiO_2 (Figure 4.2b). Since SFG signals from isotropic environments cancel, molecules bound to the sides of the nanoparticles do not contribute since vibrational modes pointing to the left will cancel those pointing to the right, and only those at the air-TiO_2 interface generate the SFG response.[50,51] The

HD-SFG spectrum features a positive high frequency peak and a broad, negative low frequency peak. The opposite relative phase of the A′(1) mode shows that the direction of the dipole of the symmetric mode is opposite to the direction of the dipole of the antisymmetric modes and $Re(CO)_3$ is aligned with the metal carbonyl modes oriented away from the TiO_2 surface, consistent with other HD-SFG reports on the carbonyl ligands of similar molecules on gold and TiO_2.[15,52]

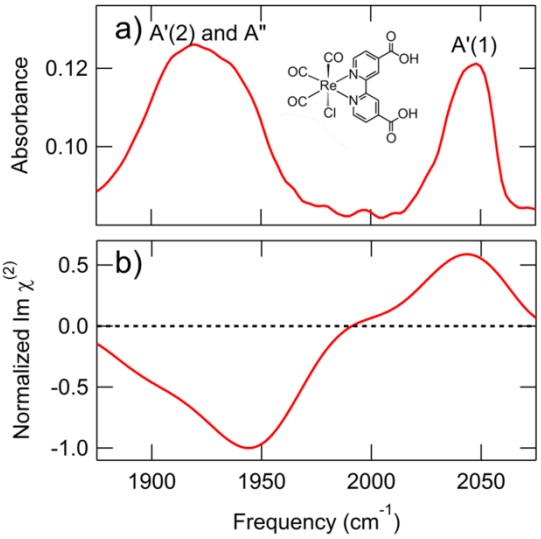

Figure 4.2 a) Molecular structure of $Re(CO)_3$ and FTIR spectrum on nanostructured TiO_2 in the CO stretch region. Labeled modes are the overlapping A′(2) and A″ CO stretch modes at 1920 cm^{-1} and the A′(1) stretch at 2048 cm^{-1}. b) Imaginary (absorptive) component of the heterodyne-detected SFG spectrum of $Re(CO)_3$ on nanostructured TiO_2.

In the interferometric 2D SFG experiments, all three CO modes are pumped simultaneously along the ω_1 axis (IR pump) and, after a given waiting time τ_2, the influence on each mode is read out along the ω_3 axis (SFG probe) in the 2D SFG

spectrum (Figure 4.3). Since spectral features in the HD-SFG spectrum can be either negative or positive depending on the absolute orientation of the vibrational dipole with respect to the interface, the corresponding 2D SFG spectrum contains important sign information that has no counterpart in bulk 2D IR experiments. Laaser and Zanni performed a detailed theoretical orientational analysis of the 2D SFG response of a model system containing two vibrational modes of equal intensity as a function of molecular orientation and beam polarizations.[53]

Ground state bleach features (reduced absorbances at the 0→1 transition frequency) exhibit the opposite sign as the HD-SFG spectrum, and induced absorbances of the 1→2 transition exhibit the opposite sign as the corresponding 0→1 bleach feature. Thus along the diagonal we observe a positive feature at lower frequencies for the ground state bleach of the (initially negative) A′(2) and A″ modes, while the negative feature at higher frequencies is the ground state bleach of the (initially positive) A′(1) mode. Corresponding induced absorbances with opposite signs are observed below the diagonal due to the redshift expected for anharmonic oscillators.

The intensity of the emitted SFG signal depends on the overlap of the projection of the vibrational dipole and Raman polarizability and the polarization of the incident and emitted beams. Vibrational modes that lie within the plane of the interface do not contribute to the generated SFG response, nor do modes which are orientationally averaged. As stated above, the diagonal features exhibit opposite signs, indicating the symmetric and antisymmetric modes are pointing in opposite directions

("up" and "down") with respect to the surface. Therefore, on average, the CO modes are pointing away from the surface, which is consistent with binding through the carboxylic acid groups on the bipyridine ligand.[53,54]

Furthermore, distinct cross peaks are observed between the higher frequency and lower frequency modes, indicating vibrational coupling. The sign and intensity of the cross peak relative to the coupled modes can reveal the relative orientation of the coupled modes. In this specific case, as seen from Figure 4.3, the sign of the cross peak follows that of the mode which is probed and is opposite the mode that is excited: the positive cross peak pumped at 2050 cm^{-1} and probed at 1950 cm^{-1} is the same sign as the positive bleach along the diagonal at 1950 cm^{-1} and opposite the sign of the negative bleach along the diagonal at 2050 cm^{-1}.

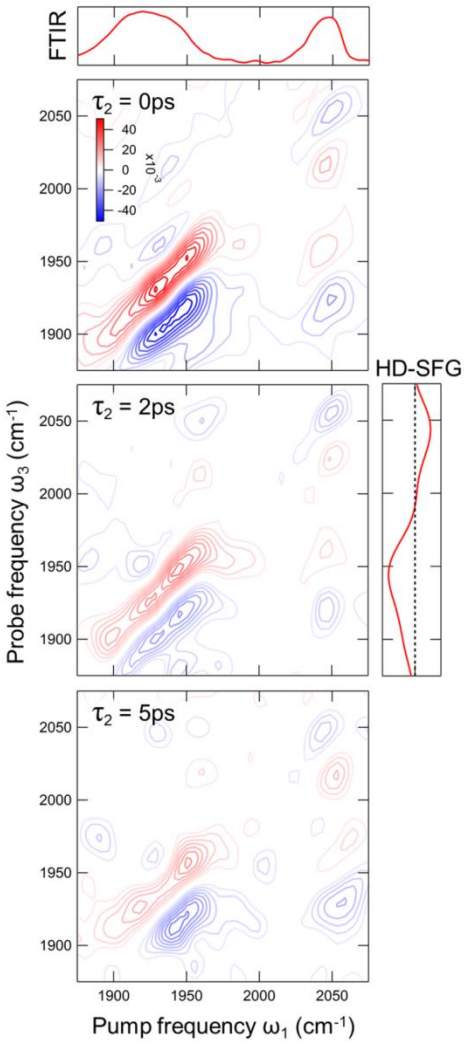

Figure 4.4 Linear FTIR spectrum (top), heterodyne-detected SFG spectrum (middle right), and interferometric 2D SFG spectra as a function of waiting time, τ_2, (center panel) of $Re(CO)_3$ on nanostructured TiO_2.

Immediately after pump excitation (τ_2 = 0ps), the elongation of the peaks along the diagonal is due to inhomogeneous broadening. Inhomogeneity arises from differences in the local environment causing frequency shifts to local vibrational modes. As a function of waiting time, molecules sample the available configurations

causing spectral diffusion with features becoming more round. Spectral diffusion dynamics are largely driven by solvent fluctuations. Fayer and coworkers observed that immobilized catalysts in contact with solvent exhibit similar spectral diffusion dynamics compared to those in bulk solutions, but dry monolayers exhibit 40% slower spectral diffusion dynamics.[55] Previous 2D IR experiments of the $Re(CO)_3$ catalyst in bulk solvent have found that spectral diffusion dynamics occur on the 3 ps time scale.[56] By extrapolation, we expect a timescale of ~4 ps for the spectral diffusion dynamics of $Re(CO)_3$ when immobilized. Since some inhomogeneity persists in the spectrum at 5 ps, we attribute this to a static heterogeneity in the system, caused by different binding geometries of the catalyst on different exposed crystal faces of the highly heterogeneous TiO_2 nanoparticles.

Previous bulk 2D IR studies of $Re(CO)_3$ and its analogs on nanostructured TiO_2 focused on the A′(1) mode. Heterogeneity in that feature was initially attributed to multiple binding geometries.[9] However, density functional theory (DFT) calculations performed to determine the frequency shift of different binding modes on the anatase (101) surface were not able to account for the experimentally observed frequencies.[12] Instead, the heterogeneity was attributed to aggregate formation, which matched well with the calculations. Aggregation was minimized when sensitizing from ethanol solution, as done here.[34] Our previous IR pump – SFG probe experiments have shown that the underlying TiO_2 structure directly coupled to the COOH ligand can change the frequency of the A′(1) mode by 10 cm^{-1}.[14] This further supports the conclusion of multiple binding geometries on the different exposed crystal faces, not

only (101) as studied previously.

Furthermore, we have observed that the catalyst bound to different single-crystalline rutile TiO_2 surfaces exhibits distinct vibrational dynamics.[14] For the A′(1) symmetric stretch, the vibrational relaxation on rutile (110) was 30% faster than that on the rutile (001) surface, with a higher frequency of the A′(1) mode on (110) compared to (001). CO vibrational modes are sensitive to the local electronic environment, therefore this difference in frequency and relaxation dynamics could be attributed to a change in the electronic structure upon binding to TiO_2 due to a difference in the surface density of states, carboxylic acid binding motif, and/or packing density within the different binding sites. Here, on nanostructured TiO_2, we also observe a frequency shift of the A′(1) mode as the system evolves. The symmetric stretch, initially at 2055 cm^{-1} with a tail at 2020 cm^{-1}, shifts to 2045 cm^{-1} by 5 ps, which is similar to the 10 cm^{-1} difference observed in the central frequency on the rutile (110) and (001) surfaces. Therefore, we attribute the apparent shift in frequency to different vibrational relaxations of subspecies bound to the different exposed crystal faces on the nanostructured TiO_2.

Additionally, the waiting time dependence of the substructure within the lower frequency diagonal feature displayed faster vibrational relaxation times of the A′(2) and A″ modes at ~1900 cm^{-1} and 1920 cm^{-1} as the intensity decreases more rapidly than the peak at ~1950 cm^{-1}. The A′(2) and A″ modes are spectrally separated in bulk solution by ~20 cm^{-1}, but this is not observed for the molecule tethered to a surface.[33,56] Since the relaxation times of these two modes were very similar when

measured in bulk with 2D IR,[57] the difference in timescales cannot be attributed to distinct vibrational modes. Therefore, analogous to the discussion above for the A′(1) mode, the low frequency feature is inhomogeneous in that it is composed of vibrational modes in slightly different environments, resulting in different vibrational lifetimes that arise from the disordered surface structure of the TiO_2.

4.4 Conclusions

Through technical advancements in increasing the phase stability in heterodyne-detected SFG experiments and incorporating an interfering pump pulse pair in IR-pump SFG-probe experiments, we have measured for the first time an interferometric 2D SFG resonant spectrum of a monolayer on a transparent material. The CO modes are found to be pointing away from the TiO_2 surface based on the relative signs of the peaks in the HD and 2D SFG spectra. The spectral diffusion and vibrational relaxation dynamics of the different modes as a function of waiting time reveal that $Re(CO)_3$ bound to nanostructured TiO_2 exhibits a mixture of different geometries, leading to a large static structural heterogeneity. The variation is due to the interaction of the complex with the underlying exposed crystal faces on the TiO_2 particles. The interfacial geometry and dynamics are critical for the CO_2 reduction reaction that occurs at the metal center. Steric considerations arising from the binding geometry and energy redistribution will play a key role in the catalytic reaction rate. The different relaxation rates and substructure within the vibrational features can be further explored by studying the complex immobilized on single crystal TiO_2 surfaces, as described in

Chapter 5. The experiments in the following chapter require a very high level of stability, as the number of molecules at the single crystal interface is less than are on the nanoparticles, thus resulting in a much smaller signal.

*Adapted from H. Vanselous, A. M. Stingel, and P. B. Petersen *J. Phys. Chem. Lett.* 2017, 8, 825-830

4.5 References

(1) Olah, G. A. Beyond Oil and Gas: The Methanol Economy. *Angew. Chem. Int. Ed.* **2005**, *44*, 2636–2639.

(2) Ganesh, I. Conversion of Carbon Dioxide into Methanol – a Potential Liquid Fuel: Fundamental Challenges and Opportunities (a Review). *Renew. Sustain. Energy Rev.* **2014**, *31*, 221–257.

(3) Kumar, B.; Llorente, M.; Froehlich, J.; Dang, T.; Sathrum, A.; Kubiak, C. P. Photochemical and Photoelectrochemical Reduction of CO_2. *Annu. Rev. Phys. Chem.* **2012**, *63*, 541–569.

(4) Cecchet, F.; Alebbi, M.; Bignozzi, C. A.; Paolucci, F. Efficiency Enhancement of the Electrocatalytic Reduction of CO_2: Fac-[Re(v-bpy)$(CO)_3$Cl] Electropolymerized onto Mesoporous TiO_2 Electrodes. *Inorganica Chim. Acta* **2006**, *359*, 3871–3874.

(5) Takeda, H.; Ohashi, M.; Tani, T.; Ishitani, O.; Inagaki, S. Enhanced Photocatalysis of rhenium(I) Complex by Light-Harvesting Periodic

Mesoporous Organosilica. *Inorg. Chem.* **2010**, *49*, 4554–4559.

(6) Liu, C.; Dubois, K.; Louis, M.; Vorushilov, A.; Li, G. Photocatalytic CO_2 Reduction and Surface Immobilization of a Tricarbonyl Re (I) Compound Modified with Amide Groups. *ACS Catal.* **2013**, *3*, 655-662.

(7) Windle, C. D.; Pastor, E.; Reynal, A.; Whitwood, A. C.; Vaynzof, Y.; Durrant, J. R.; Perutz, R. N.; Reisner, E. Improving the Photocatalytic Reduction of CO_2 to CO through Immobilisation of a Molecular Re Catalyst on TiO_2. *Chemistry* **2015**, *21*, 3746–3754.

(8) Anderson, N. A.; Lian, T. Ultrafast Electron Injection from Metal Polypyridyl Complexes to Metal-Oxide Nanocrystalline Thin Films. *Coord. Chem. Rev.* **2004**, *248*, 1231–1246.

(9) Xiong, W.; Laaser, J. E.; Paoprasert, P.; Franking, R. A.; Hamers, R. J.; Gopalan, P.; Zanni, M. T. Transient 2D IR Spectroscopy of Charge Injection in Dye-Sensitized Nanocrystalline Thin Films. *J. Am. Chem. Soc.* **2009**, *131*, 18040–18041.

(10) Paoprasert, P.; Laaser, J. E.; Xiong, W.; Franking, R. a; Hamers, R. J.; Zanni, M. T.; Schmidt, J. R.; Gopalan, P. Bridge-Dependent Interfacial Electron Transfer from Rhenium - Bipyridine Complexes to TiO_2 Nanocrystalline Thin Films. *J. Phys. Chem. C* **2010**, *114*, 9898–9907.

(11) Anfuso, C. L.; Snoeberger, R. C.; Ricks, A. M.; Liu, W.; Xiao, D.; Batista, V. S.; Lian, T. Covalent Attachment of a Rhenium Bipyridyl CO_2 Reduction Catalyst to Rutile TiO_2. *J. Am. Chem. Soc.* **2011**, *133*, 6922–6925.

(12) Laaser, J. E.; Christianson, J. R.; Oudenhoven, T. A.; Joo, Y.; Gopalan, P.; Schmidt, J. R.; Zanni, M. T. Dye Self-Association Identified by Intermolecular Couplings between Vibrational Modes As Revealed by Infrared Spectroscopy, and Implications for Electron Injection. *J. Phys. Chem. C* **2014**, *118*, 5854–5861.

(13) Ricks, A. M.; Anfuso, C. L.; Rodríguez-Córdoba, W.; Lian, T. Vibrational Relaxation Dynamics of Catalysts on TiO_2 Rutile (110) Single Crystal Surfaces and Anatase Nanoporous Thin Films. *Chem. Phys.* **2013**, *422*, 264–271.

(14) Calabrese, C.; Vanselous, H.; Petersen, P. B. Deconstructing the Heterogeneity of Surface-Bound Catalysts: Rutile Surface Structure Affects Molecular Properties. *J. Phys. Chem. C* **2016**, *120*, 1515–1522.

(15) Rich, C. C.; Mattson, M. A.; Krummel, A. T. Direct Measurement of the Absolute Orientation of N3 Dye at Gold and Titanium Dioxide Surfaces with Heterodyne-Detected Vibrational SFG Spectroscopy. *J. Phys. Chem. C* **2016**, *120*, 6601–6611.

(16) Shen, Y. R. *The Principles of Nonlinear Optics*; John Wiley & Sons, Inc.: New York, 1984.

(17) Boyd, R. W. *Nonlinear Optics*, Third.; Elsevier Inc.: Burlington, 2008.

(18) Moad, A. J.; Simpson, G. J. A Unified Treatment of Selection Rules and Symmetry Relations for Sum-Frequency and Second Harmonic Spectroscopies. *J. Phys. Chem. B* **2004**, *108*, 3548–3562.

(19) Shen, Y. R. Phase-Sensitive Sum-Frequency Spectroscopy. *Annu. Rev. Phys.*

Chem. **2013**, *64*, 129–150.

(20) Nihonyanagi, S.; Mondal, J. A; Yamaguchi, S.; Tahara, T. Structure and Dynamics of Interfacial Water Studied by Heterodyne-Detected Vibrational Sum-Frequency Generation. *Annu. Rev. Phys. Chem.* **2013**, *64*, 579–603.

(21) Guyot-Sionnest, P.; Dumas, P.; Chabal, Y. Lifetime of an Adsorbate-Substrate Vibration Measured by Sum Frequency Generation: H on Si (111). *J. Electron Spectrosc. Relat. Phenom.* **1990**, *54/55*, 27–38.

(22) Wolfrum, K.; Löbau, J.; Birkhölzer, W.; Laubereau, A. Vibrational Sum-Frequency Spectroscopy of Phase Transitions in Langmuir Films and Three-Colour Pump - Probe Studies of Chemisorbed Molecules. *Quantum Semiclassical Opt.* **1997**, *9*, 257–267.

(23) Bordenyuk, A. N.; Jayathilake, H.; Benderskii, A. V. Coherent Vibrational Quantum Beats as a Probe of Langmuir-Blodgett Monolayers. *J. Phys. Chem. B* **2005**, *109*, 15941–15949.

(24) McGuire, J. A.; Shen, Y. R. Ultrafast Vibrational Dynamics at Water Interfaces. *Science* **2006**, *313*, 1945–1948.

(25) Ghosh, A.; Smits, M.; Bredenbeck, J.; Dijkhuizen, N.; Bonn, M. Femtosecond Time-Resolved and Two-Dimensional Vibrational Sum Frequency Spectroscopic Instrumentation to Study Structural Dynamics at Interfaces. *Rev. Sci. Instrum.* **2008**, *79*, 93907.

(26) Rao, Y.; Song, D.; Turro, N. J.; Eisenthal, K. B. Orientational Motions of Vibrational Chromophores in Molecules at the Air/water Interface with Time-

Resolved Sum Frequency Generation. *J. Phys. Chem. B* **2008**, *112*, 13572–13576.

(27) Eftekhari-Bafrooei, A.; Borguet, E. Effect of Surface Charge on the Vibrational Dynamics of Interfacial Water. *J. Am. Chem. Soc.* **2009**, *131*, 12034–12035.

(28) Velarde, L.; Zhang, X.; Lu, Z.; Joly, A. G.; Wang, Z.; Wang, H. Communication : Spectroscopic Phase and Lineshapes in High- Resolution Broadband Sum Frequency Vibrational Spectroscopy : Resolving Interfacial Inhomogeneities of " Identical " Molecular Groups Communication : Spectroscopic Phase and Lineshapes in High-Re. **2011**, *241102*.

(29) Chen, S.-L.; Fu, L.; Chase, Z. A.; Gan, W.; Wang, H.-F. Local Environment and Interactions of Liquid and Solid Interfaces Revealed by Spectral Line Shape of Surface Selective Nonlinear Vibrational Probe. *J. Phys. Chem. C* **2016**, *120*, 25511–25518.

(30) Wang, H.-F. Sum Frequency Generation Vibrational Spectroscopy (SFG-VS) for Complex Molecular Surfaces and Interfaces: Spectral Lineshape Measurement and Analysis plus Some Controversial Issues. *Prog. Surf. Sci.* **2016**, *91*, 155–182.

(31) Hamm, P.; Zanni, M. *Concepts and Methods of 2D Infrared Spectroscopy*; Cambridge University Press, 2011.

(32) Fayer, M. D. *Ultrafast Infrared Vibrational Spectroscopy*; CRC Press, 2013; Vol. 2.

(33) Rosenfeld, D. E.; Gengeliczki, Z.; Smith, B. J.; Stack, T. D. P.; Fayer, M. D.

Structural Dynamics of a Catalytic Monolayer Probed by Ultrafast 2D IR Vibrational Echoes. *Science* **2011**, *334*, 634–639.

(34) Oudenhoven, T. A.; Joo, Y.; Laaser, J. E.; Gopalan, P.; Zanni, M. T. Dye Aggregation Identified by Vibrational Coupling Using 2D IR Spectroscopy. *J. Chem. Phys.* **2015**, *142*, 212449.

(35) Kraack, J. P.; Lotti, D.; Hamm, P. Ultrafast, Multidimensional Attenuated Total Reflectance Spectroscopy of Adsorbates at Metal Surfaces. *J. Phys. Chem. Lett.* **2014**, *5*, 2325–2329.

(36) Kraack, J. P.; Hamm, P. Surface-Sensitive and Surface-Specific Ultrafast Two-Dimensional Vibrational Spectroscopy. *Chem. Rev.* DOI: 10.1021/acs.chemrev.6b00437

(37) Hsieh, C. S.; Okuno, M.; Hunger, J.; Backus, E. H. G.; Nagata, Y.; Bonn, M. Aqueous Heterogeneity at the Air/water Interface Revealed by 2D-HD-SFG Spectroscopy. *Angew. Chemie - Int. Ed.* **2014**, *53*, 8146–8149.

(38) Inoue, K.; Nihonyanagi, S.; Singh, P. C.; Yamaguchi, S.; Tahara, T. 2D Heterodyne-Detected Sum Frequency Generation Study on the Ultrafast Vibrational Dynamics of H_2O and HOD Water at Charged Interfaces. *J. Chem. Phys.* **2015**, *142*, 212431.

(39) Xiong, W.; Laaser, J. E.; Mehlenbacher, R. D.; Zanni, M. T. Adding a Dimension to the Infrared Spectra of Interfaces Using Heterodyne Detected 2D Sum-Frequency Generation (HD 2D SFG) Spectroscopy. *Proc. Natl. Acad. Sci. U.S.A.* **2011**, *108*, 20902–20907.

(40) Wang, J.; Clark, M. L.; Li, Y.; Kaslan, C. L.; Kubiak, C. P.; Xiong, W. Short-Range Catalyst–Surface Interactions Revealed by Heterodyne Two-Dimensional Sum Frequency Generation Spectroscopy. *J. Phys. Chem. Lett.* **2015**, *6*, 4204–4209.

(41) Cervetto, V.; Helbing, J.; Bredenbeck, J.; Hamm, P. Double-Resonance versus Pulsed Fourier Transform Two-Dimensional Infrared Spectroscopy: An Experimental and Theoretical Comparison. *J. Chem. Phys.* **2004**, *121*, 5935–5942.

(42) Shim, S.-H.; Strasfeld, D. B.; Ling, Y. L.; Zanni, M. T. Automated 2D IR Spectroscopy Using a Mid-IR Pulse Shaper and Application of This Technology to the Human Islet Amyloid Polypeptide. *Proc. Natl. Acad. Sci.* **2007**, *104*, 14197–14202.

(43) Shim, S.-H.; Zanni, M. T. How to Turn Your Pump-Probe Instrument into a Multidimensional Spectrometer: 2D IR and Vis Spectroscopies via Pulse Shaping. *Phys. Chem. Chem. Phys.* **2009**, *11*, 748–761.

(44) Schleeger, M.; Grechko, M.; Bonn, M. Background-Free Fourth-Order Sum Frequency Generation Spectroscopy. *J. Phys. Chem. Lett.* **2015**, *6*, 2114–2120.

(45) Vanselous, H.; Petersen, P. B. Extending the Capabilities of Heterodyne-Detected Sum-Frequency Generation Spectroscopy : Probing Any Interface in Any Polarization Combination. *J. Phys. Chem. C* **2016**, *120*, 8175–8184.

(46) Stingel, A. M.; Petersen, P. B. Couplings Across the Vibrational Spectrum Caused by Strong Hydrogen Bonds: A Continuum 2D IR Study of the 7-

Azaindole--Acetic Acid Heterodimer. *J. Phys. Chem. B* **2016**, *120*, 10768–10779.

(47) DeFlores, L. P.; Nicodemus, R. A.; Tokmakoff, A. Two-Dimensional Fourier Transform Spectroscopy in the Pump-Probe Geometry. *Opt. Lett.* **2007**, *32*, 2966.

(48) Karthick Kumar, S. K.; Tamimi, A.; Fayer, M. D. Comparisons of 2D IR Measured Spectral Diffusion in Rotating Frames Using Pulse Shaping and in the Stationary Frame Using the Standard Method. *J. Chem. Phys* **2012**, *137*, 184201.

(49) Diao, F.; Liang, W.; Tian, F.; Wang, Y.; Vivo, P.; Efimov, A.; Lemmetyinen, H. Preferential Attachments of Organic Dyes onto {101} Facets of TiO_2 Nanoparticles. *J. Phys. Chem. C* **2015**, *119*, 8960–8965.

(50) Bordenyuk, A. N.; Weeraman, C.; Yatawara, A. K.; Jayathilake, H. D.; Stiopkin, I.; Liu, Y.; Benderskii, A. V. Vibrational Sum Frequency Generation Spectroscopy of Dodecanethiol on Metal Nanoparticles. *J Phys Chem C* **2007**, *111*, 8925–8933.

(51) Frederick, M. T.; Achtyl, J. L.; Knowles, K. E.; Weiss, E. A; Geiger, F. M. Surface-Amplified Ligand Disorder in CdSe Quantum Dots Determined by Electron and Coherent Vibrational Spectroscopies. *J. Am. Chem. Soc.* **2011**, *133*, 7476–7481.

(52) Anfuso, C. L.; Ricks, A. M.; Rodríguez-Córdoba, W.; Lian, T. Ultrafast Vibrational Relaxation Dynamics of a Rhenium Bipyridyl CO_2–Reduction

Catalyst at a Au Electrode Surface Probed by Time-Resolved Vibrational Sum Frequency Generation Spectroscopy. *J. Phys. Chem. C* **2012**, *116*, 26377–26384.

(53) Laaser, J. E.; Zanni, M. T. Extracting Structural Information from the Polarization Dependence of One- and Two-Dimensional Sum Frequency Generation Spectra. *J. Phys. Chem. A* **2013**, *117*, 5875–5890.

(54) Wang, J.; Clark, M. L.; Li, Y.; Kaslan, C. L.; Kubiak, C. P.; Xiong, W. Short-Range Catalyst–Surface Interactions Revealed by Heterodyne Two-Dimensional Sum Frequency Generation Spectroscopy. *J. Phys. Chem. Lett.* **2015**, *6*, 4204–4209.

(55) Rosenfeld, D. E.; Nishida, J.; Yan, C.; Kumar, S. K. K.; Tamimi, A.; Fayer, M. D. Structural Dynamics at Monolayer-Liquid Interfaces Probed by 2D IR Spectroscopy. *J. Phys. Chem. C* **2013**, *117*, 1409–1420.

(56) Kiefer, L. M.; Kubarych, K. J. Solvent-Dependent Dynamics of a Series of Rhenium Photoactivated Catalysts Measured with Ultrafast 2DIR. *J. Phys. Chem. A* **2015**, *119*, 959–965.

(57) Delor, M.; Sazanovich, I. V; Towrie, M.; Spall, S. J.; Keane, T.; Blake, A. J.; Wilson, C.; Meijer, A. J. H. M.; Weinstein, J. A. Dynamics of Ground and Excited State Vibrational Relaxation and Energy Transfer in Transition Metal Carbonyls. *J. Phys. Chem. B* **2014**, *118*, 11781–11791.

CHAPTER 5

TWO DIMENSIONAL SFG OF MONOLAYERS: STRIKING DIFFERENCE BETWEEN CO_2 REDUCTION CATALYSTS ON NANOSTRUCTURED AND SINGLE CRYSTALLINE TIO_2 SURFACES

5.1 Introduction

Titanium dioxide (TiO_2) is widely employed in photo and electrocatalysis as both a photosensitizer (e.g in photodegradation of organic compounds and water splitting[1]) and an electron acceptor (e.g. in dye-sensitized solar cells[2] and CO_2 photocatalysis[3]). By immobilizing the catalyst on a high-surface area support, the overall device efficiency is enhanced due to an increased number of active sites.[4–6] Furthermore, TiO_2 nanoparticles when sensitized with molecular CO_2 catalysts significantly enhance the molecular reaction efficiency when compared to other oxide structures or in solution.[3,7] Charge injection from the catalyst to TiO_2 was a critical step in the proposed enhanced reaction mechanism. Rhenium tricarbonyl complexes[3-7] have been model complexes for CO_2 reduction, and ruthenium based dyes, such as the N3, which are structurally similar to the rhenium complexes, are often used in dye-sensitized solar cells.[8] A better understanding of how these catalysts interact with different TiO_2 surfaces on a molecular level is not only relevant for our fundamental understanding of organic/inorganic interfaces, but would have significant implications in the fields of catalysis and solar energy harvesting. Particularly with the increased interest in high

surface area nanostructured single crystal architectures, such as nanorods and nanosheets,[9-17] understanding this interaction is crucial for the rational and directed design of advanced materials.

It has become well known that the binding of molecules to specific surface structures can significantly influence the efficiency of reactions on TiO_2,.[18-28] As an example, photodegradation of methyl orange was found to be most efficient on the anatase (001) surface compared to the (101) and (010) surfaces.[27] Meanwhile, photovoltaic performance of a metal-free organic dye (MK-2) sensitized TiO_2 was more efficient on anatase (010) compared to (101) and (001)[27] while the performance of N3 sensitized TiO_2 was optimum on rutile (100) compared to rutile (001) and anatase (001) and (101).[18] Li et. al. attributed the increased performance of the MK-2 TiO_2 system to a stronger interaction and faster charge injection between the dye and anatase (010).[27] Lu et. al. attributed the difference in the N3 system to differences in the binding geometry at the different surfaces.[18] Likely, these two contributions are highly related: the interaction between TiO_2 and the catalyst is modulated through the binding mode and geometry.

To examine how the bonding to single crystalline and nanostructured TiO_2 surfaces affects CO_2 reduction catalysts, we use recently developed interferometric 2D sum-frequency generation (2D SFG) spectroscopy.[29-31] This technique can characterize the vibrational spectrum, molecular orientation of the surface-bound catalyst, homogeneous and heterogenerous line broadening, and vibrational couplings and dynamics. Accordingly, it provides detailed information on the molecular

orientation, femtosecond and picosecond vibrational dynamics, and vibrational relaxation processes of catalytic monolayers on nanostructured and single-crystalline TiO_2 surfaces alike. Our robust method features high frequency and temporal resolution to resolve femtosecond vibrational dynamics coupled with high experimental stability needed to collect data from transparent materials, which often require long acquisition times.[29,32,33] By probing the frequency and dynamics of the carbonyl vibrational modes at the metal center on the catalyst, which are good markers for the electronic structure, we can directly monitor the degree of electronic interaction, for example partial electron transfer, between the catalyst and TiO_2 surface. Additionally, studies of the photocatalytic reaction mechanism showed a ~30 picosecond delay between excitation and electron injection into the TiO_2,[7] suggesting that the vibrational dynamics, which are on that timescale, may act as a barrier for the important photoexcited electron-injection step. Here, we compare the carbonyl vibrational properties of a rhenium tricarbonyl CO_2 reduction catalyst on single crystal rutile (110), rutile (001), and anatase (101) surfaces. The carbonyl vibrations in the catalyst prepared on the three distinct surfaces show measurably different vibrational coupling and relaxation timescales compared to the catalyst on a nanocrystalline TiO_2 thin film.

5.2 Experimental Methods

5.2.1 Sample Preparation

Re(4,4′-dicarboxyl-2,2′-bipyridine)$(CO)_3Cl$ ($Re(CO)_3$) was synthesized according to a

published literature procedure.[33,59] Polished single crystal rutile (110) and (001) substrates were purchased from MTI Corporation and anatase (101) was purchased from SurfaceNet GmbH. The substrates were pretreated[60] in basic piranha solution (1:1:2 $H_2O_2/NH_4OH/H_2O$) at 80°C for ten minutes and rinsed thoroughly with ultrapure water (Millipore Milli-Q, 18.2 MΩ·cm, ≤5 ppb total organic carbon) until neutral pH was achieved. The crystals were sensitized overnight in $Re(CO)_3$ saturated ethanol solution and rinsed with excess ethanol before use.

5.2.2 2D SFG Experiments

Experimental details for 2D SFG experiments have been described previously.[29] Briefly, a Ti:sapphire oscillator (Coherent Micra-5) seeded a Ti:sapphire amplifier (Coherent Legend Elite Duo), which produced 800 nm pulses (5 mJ, 25 fs, 1 kHz). The 800 nm beam was split into three separate beams. One beam contained 0.75 mJ and was spectrally narrowed using a Fabry−Perot etalon (TecOptics, Inc.) to create the visible upconversion pulse (792.3 nm, 0.7 nm full-width at half-maximum intensity (FWHM)). Another beam contained 3 mJ and was used to pump a commercial optical parametric amplifier (Coherent OPerA Solo), which generated tunable mid-IR pulses (1924 cm^{-1}, 249 cm^{-1} fwhm). The IR pulses were split into a probe pulse and a pump pulse with a KBr beamsplitter. The pump was further split, interfered in a Mach-Zehnder interferometer, and recombined collinearly. An external local oscillator was generated spatially before the sample in transmission by focusing the visible and IR beams in a ZnO coated (150 nm) 0.7 mm thick CaF_2 window. The three beams

(visible, IR probe, and SFG_{LO}) were recollimated with an off-axis parabolic mirror. A delay plate, 2 mm thick SiO_2, was used to temporally delay the SFG_{LO} beam. The visible (10.4 uJ), IR probe (3.5 uJ), and IR pump pair (2.6 uJ in each arm) were focused on the sample with another off-axis parabolic mirror at 60°, 65°, and 55° with respect to the surface normal in the *ppppp* polarization combination (polarization of SFG, visible, IR probe, and each IR pump pulse, respectively). The emitted SFG signal was dispersed by a grating and imaged onto a liquid-nitrogen-cooled CCD (Princeton Instruments, model 7509-0001, 1340 × 400 pixels). To correct for potential laser fluctuations and sample degradation, the pump was synchronized with an optical chopper which was triggered by the laser (every other pump pulse in one arm of the interferometer was blocked by the chopper). A galvanometric mirror was fed a 500 Hz sine wave, also synchronized with the laser, and spatially separated the generated SFG field influenced by one pump from the SFG field with two interfering pumps on the CCD.[61]

By scanning one pump with respect to the other with a step size of 2 fs from -100 to 1500 fs, an interferogram was formed in the pump axis, τ_1. At each time point, heterodyne-detected (HD) SFG data was collected in the probe axis with an integration time of five seconds The HD SFG signal is collected as a function of τ_1, and the signal is Fourier transformed to obtain a complex signal which is a function of two frequency variables, ω_1 and ω_2. For each sample, the data presented here was an average of four acquisitions, with the exception of the anatase (101) which was an average of two. A series of waiting times, τ_2, are collected by delaying the visible and

IR probe pulses with respect to the stationary pump. The frequency resolution in the probe axis is 10 cm^{-1}, set by the visible upconversion pulse, the frequency resolution in the pump axis is 22 cm^{-1}, set by the step size and distance scanned between the pump pulses, and the temporal resolution in τ_2 is 100 fs, determined by the third-order IR_{pump}-IR_{probe}-Visible cross-correlation.

5.3 Results and Discussion

5.3.1 Bulk FTIR Spectra

The $Re(CO)_3$ molecule used in the present study contains three CO ligands at the metal center which have three vibrational modes, shown in Figure 5.1. The lower frequency feature at ~1950 cm^{-1} is a combination of the A′(2) antisymmetric stretch of the axial versus equatorial CO ligands and the A″ antisymmetric stretch of the equatorial carbonyl ligands, while the higher frequency mode ~2050 cm^{-1} is the A′(1) symmetric stretch involving all three carbonyl ligands. Bulk FTIR measurements were collected for a saturated solution of the catalyst in ethanol (Figure 5.1, black trace). When $Re(CO)_3$ was immobilized on TiO_2 nanoparticles, the CO stretch frequencies shifted and broadened substantially (Figure 5.1, red trace). These spectral differences are an indication of a large heterogeneous distribution vibrational frequencies on nanocrystalline TiO_2, reflecting either different structural binding motifs or different aggregation states which could influence the degree of charge transfer from the catalyst to the TiO_2.[34-36]

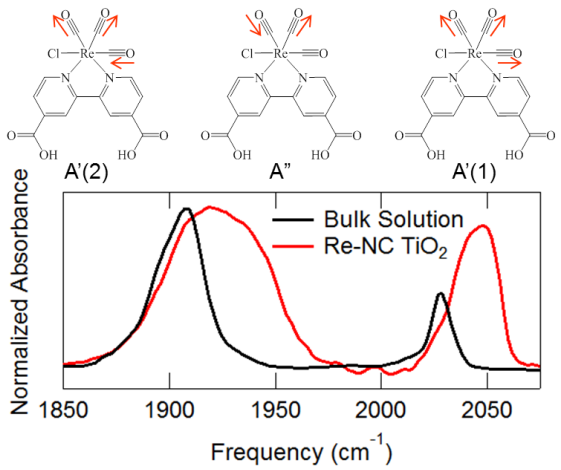

Figure 5.1 FTIR spectra of $Re(CO)_3$ in bulk ethanol solution and immobilized on nanocrystalline TiO_2 nanoparticles.

5.3.2 Surface-Sensitive Heterodyne-Detected Measurements

Sum-frequency generation spectroscopy is a surface-specific technique with sub-monolayer sensitivity which provides the vibrational spectrum of the surface.[37] To increase the sensitivity and obtain orientational information, heterodyne-detection (HD) can be used.[38,39] The electric field generated by the sample is a complex quantity where real and imaginary components are the in-phase and out-of-phase components of the field. In this notation, the real and imaginary components of the SFG electric field correspond to the dispersive and absorptive lineshapes, respectively (Figure 5.2). Consistent with previous HD SFG experiments of $Re(CO)_3$ monolayers on TiO_2 and gold, the high and low frequency modes exhibit opposite signs,[29,31,40,41] indicating that the transition dipole moment of the vibrational symmetric stretch mode is oriented away from the surface and the dipole moments of the asymmetric modes are oriented

towards the surface. The molecular orientation is thus observed to be generally perpendicular to the surface as expected, because the complex is anchored to the surface through carboxylate groups.

As shown in Figure 5.2, the ratio of the two features varies as a function of the TiO_2 surface, reflecting differences in the molecular orientation, where a bigger ratio of low frequency mode to high frequency mode is indicative of an angle further from perpendicular to the surface.[40] Furthermore, like the linear FTIR spectra, broader features in the HD SFG spectrum indicate larger heterogeneity. As seen in Figure 5.2, $Re(CO)_3$ on nanocrystalline TiO_2 has the largest ratio and distribution, indicating a large heterogeneity at the surface. Comparing the single-crystalline surfaces, we observe that the rutile (001) surface has a higher asymmetric:symmetric stretch ratio than the (110) surface. One explanation could be the difference in symmetry of the two surfaces. Reducing the symmetry of the surface from isotropic C_{4v} for (001) to C_{2v} for (110)[43] results in a more narrow range of orientations which are closer to perpendicular. The anatase (101) contains 2-fold coordinated oxygen atoms and 5-coordinated Ti atoms similar to the rutile (110) surface, and also has a similar asymmetric:symmetric stretch ratio. The overall orientation is important for the reaction mechanism, as CO_2 binds to the rhenium center from solution and must not be sterically hindered.

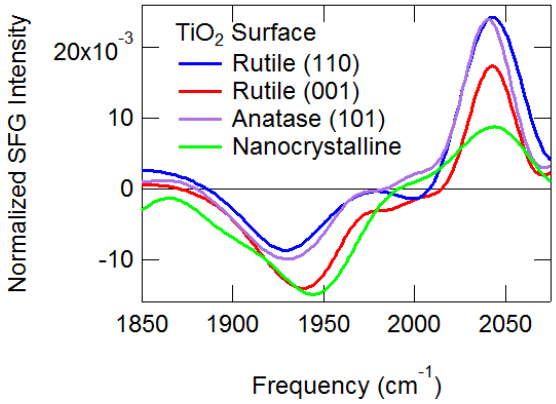

Figure 5.2 Imaginary component of the heterodyne-detected SFG spectrum of $Re(CO)_3$ on different TiO_2 surfaces. Spectra are normalized to the total absolute peak area.

5.3.3 Interferometric 2D Sum-Frequency Generation Spectra

Higher order spectroscopies can provide added information compared to linear spectroscopy by, for example, separating contributions from heterogeneous and homogeneous broadening and measuring vibrational couplings. Bulk 2D IR spectroscopy[44,45] has recently been applied to molecular monolayers, but 2D SFG is a direct surface-specific extension to bulk 2D IR.[42,46-48] 2D SFG can be performed in two general formats: a low-resolution single-excitation pulse variant, and an interferometric two-excitation pulse version exhibiting the highest spectral and temporal resolution.[49-51] To resolve the real and imaginary components of the signal electric field without assuming a lineshape, heterodyne detection has to be implemented. This can either be done *in situ* for molecules bound to surfaces

exhibiting a large nonresonant SFG response, such as gold or crystalline quartz,[38,52] or with an external local oscillator.[39] The pulse sequence for interferometric 2D SFG with an external oscillator is shown in Figure 5.3. An interferometric pump pulse pair excites the sample, which is then probed with HD SFG. The relative delay time between the pump pair, τ_1, is scanned, producing an interferogram which is then Fourier transformed to create the excitation axis. To monitor dynamics, the waiting time, τ_2, is varied.

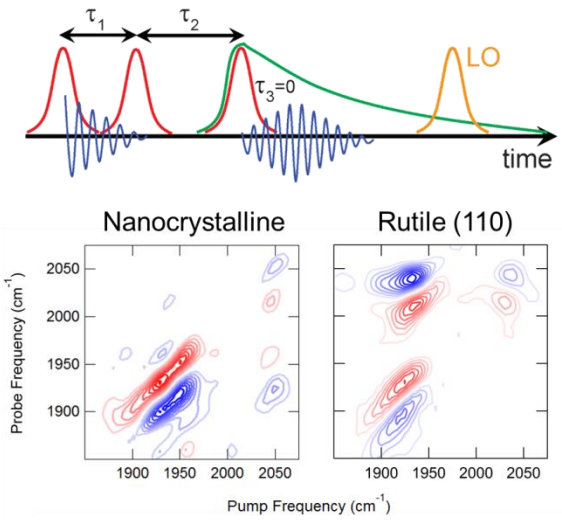

Figure 5.3 Top: Pulse sequence. Bottom: 2D SFG spectrum of $Re(CO)_3$ on nanocrystalline TiO_2 (left) and single crystal rutile (110) TiO_2 collected at a waiting time, τ_2, of 0 ps. Contours are evenly spaced with blue indicating negative values and red indicating positive values.

The 2D SFG spectra are rich with structural and dynamic information of the surface-bound catalyst, shown in Figure 5.3 for a waiting time of zero. Along the diagonal (pump frequency equal to probe frequency), the bleach of the fundamental transitions of the vibrational modes in Figure 5.2 appear with opposite signs. Bleach

features are a result of a reduced absorbance, and since the HD SFG spectrum contains a positive and a negative peak, the resulting bleach peaks along the diagonal in the 2D SFG spectrum will exhibit a negative and positive feature, respectively. In bulk 2D IR experiments, phase information is not retained and all bleach features are negative. Below each diagonal feature is a feature with opposite sign corresponding to an induced absorbance from excitation of the ν=2 level.

5.3.4 Cross-Peak Variation

Cross-peaks in 2D vibrational spectra signify anharmonic coupling between the given vibrational modes and thus help to explore the vibrational energy landscape of the system. If a set of vibrations are coupled, a pair of cross-peaks will be present in the off-diagonal regions of the 2D spectrum. The off-diagonal feature at higher probe frequency (the blue peak in the (110) surface at pump frequency = 1925 cm^{-1} and probe frequency = 2040 cm^{-1} in Fig. 5.3) is due reduced population in the mode that is not at that excitation frequency, which arising due to a coupled ground state. Meanwhile, the off-diagonal feature at lower probe frequency (the red peak in the (110) surface at pump frequency = 1925 cm^{-1} and probe frequency = 2000 cm^{-1} in Fig. 5.3) is due to an induced absorption into the combination band.

In the bulk 2D IR spectrum, at zero waiting time, the cross-peaks in the two quadrants are equal in intensity, with asymmetries at longer times reflecting energy relaxation. In 2D SFG, the intensity of the cross-peaks can be asymmetric due to several effects, including differences in intensity in the two coupled modes, providing

further information on the molecular structure. As seen in Figure 5.3, in the case of the nanocrystalline system, a cross-peak is observed when exciting the symmetric stretch and probing the asymmetric stretch while, within signal-to-noise, no discernable cross-peak is present when exciting in the reverse order. However, the opposite trend is observed on the single crystal surface. There are two potential contributions to this difference.

The first contribution is related to the selection rules and cross-sections for the excitation and detection axes in 2D SFG when compared to 2D IR. In 2D SFG, the detection features must be SFG (both IR and Raman) active, while excitation only requires IR activity through a change in the transition dipole. Furthermore, for the mode to be SFG active, there needs to be an anisotropic distribution of the transition dipole moment in the vibrational chromophores. In a theoretical study of 2D SFG by Laaser and Zanni, it was shown that SFG-silent modes could be probed through cross-peaks when coupled to an SFG-active mode.[55] The excitation axis involved two dipole transitions, $\mu\mu$, while the detection axis is produced through a Raman and dipole transition, $\alpha\mu$. That study focused on spectral changes assuming that both modes had equivalent dipole transition and polarizability strengths. Building on that, we explore changes as a result of different strengths.

The dependence of the main features of the 2D SFG spectrum is depicted in Figure 5.4. If there are two coupled vibrational modes of unequal intensity, the cross-peaks will also be unequal. For example, if peak 1 were stronger than peak 2 due to a larger Raman transition, then cross-peak 4 would be stronger than cross-peak 3. If

instead, peak 1 were stronger due to a larger dipole moment, then cross-peak 3 would be stronger than cross-peak 4. From the HD spectra in Figure 5.2, it is clear that the SFG peak of the symmetric stretch is stronger than the asymmetric stretches on the single crystal surfaces, while the IR intensities from the FTIR spectrum of the immobilized catalyst in Figure 5.1 are roughly equivalent. This difference would contribute to a stronger cross-peak in the upper left quadrant of the 2D SFG spectrum. Since the HD SFG spectra of the nanocrystalline system displays a stronger asymmetric stretch compared to the symmetric stretch, the opposite cross-peak trend is expected in the 2D data for the nanocrystalline system.

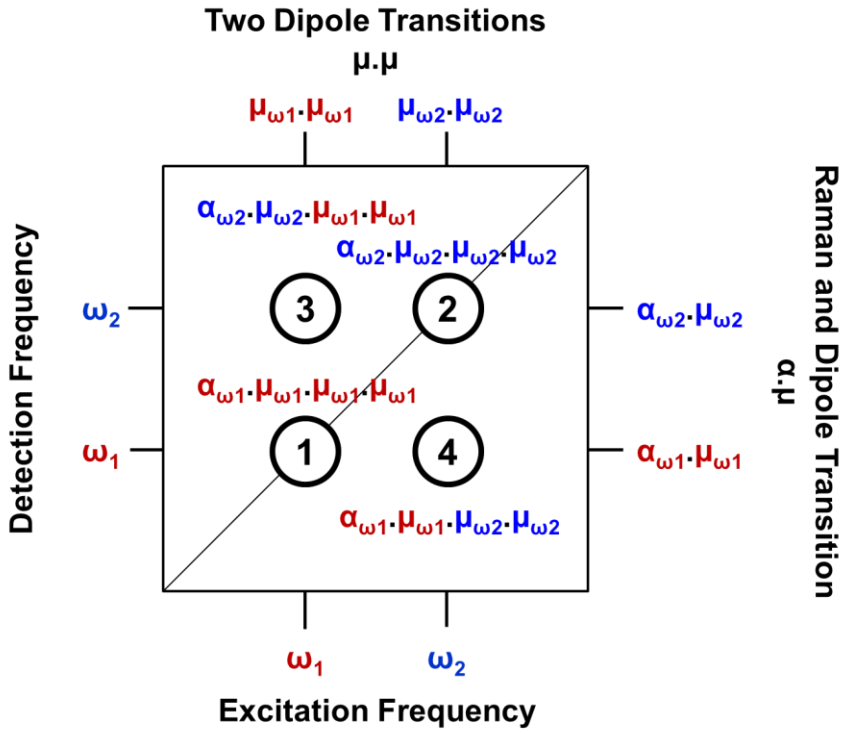

Figure 5.4 Schematic diagram of a 2D SFG spectrum containing two vibrational modes, ω_1 and ω_2. The dependence of the detection and excitation axes are listed on the opposing axis and contributions to each feature are noted.

While these trends are observed in Figure 5.3 and such Raman and dipole transition strength differences likely contribute to the uneven intensities of the cross-peaks, which could explain why the upper cross-peak for the nanostructured surface is not observed within the signal-to-noise, the complete lack of the lower frequency cross-peak is striking, particularly given the exceedingly strong upper cross-peak. Another explanation for this striking peak asymmetry may lie in the high level of molecular ordering on single crystal TiO_2. The transition dipole moment of the symmetric stretch roughly points perpendicular to the surface for all of the molecules, while the asymmetric modes are closer to parallel with the A′(2) and A″ modes 90° apart. Therefore, a delocalized vibrational mode[56] created through aligned dipole-dipole interactions, previously invoked to explain 2D studies of the amide I band of peptides[57] and OH stretches of water[58], may exist among the symmetric modes of neighboring $Re(CO)_3$ molecules. Exciting the asymmetric modes produces a coherent response from this exciton, resulting in the presence of an anomalously strong cross-peak. However, exciting the symmetric stretch does not produce a cross-peak since the asymmetric stretches are not all aligned, resulting in cancelation. A third possibility is that the average over different molecular orientations within the sample ensemble results in cancelations of one cross-peak but not the other. A collaboration with the Batista group is currently underway to further explore these different contributions. The Batista group is able to simulate 2D SFG spectra of this molecule and vary the overall orientation and distribution at the surface to better understand the influence of geometry on the 2D spectra.

5.3.5 Vibrational Relaxation Dynamics

Our previous pump-SFG probe experiments examined the vibrational relaxation of the symmetric stretch carbonyl mode of the catalyst on rutile (110) and (001).[33] That previous work found a symmetric stretch vibrational relaxation timescale of 18 ps on rutile (110) and 26 ps on the (001) surface. 2D SFG measurements as a function of waiting time, shown in Figure 5.5, frequency resolve the excitation axis which makes it possible to determine the direction of vibrational energy flow in the system. The corresponding pump-probe signal at a given waiting time can be obtained by integrating the 2D spectrum along the excitation axis thereby summing diagonal and off-diagonal features. Normally, off-diagonal peaks are significantly weaker than diagonal peaks and pump-probe spectra are dominated by the diagonal features. Therefore, the observed relaxation dynamics in pump-probe experiments reflect the relaxation of the vibrational mode at the given frequency.

These typical 2D spectral features are observed for the case of $Re(CO)_3$ on nanocrystalline TiO_2, as described in detail in Ref. 29. However, for the rutile (110) surface, the diagonal peak of the symmetric mode relaxes within 5 ps, while the strong cross-peak to the antisymmetric modes decays much more slowly and is still present at 10 ps. The symmetric stretch decay on rutile (001) is similar although somewhat slower than on (110). Accordingly, the upper cross-peak is much stronger than the diagonal peak of the symmetric mode. This means that the pump-probe experiments are actually measuring the longer vibrational relaxation of the asymmetric modes at the lower frequency through the cross-peak. This highlights the importance of 2D

experiments which can reveal previously obscured information.

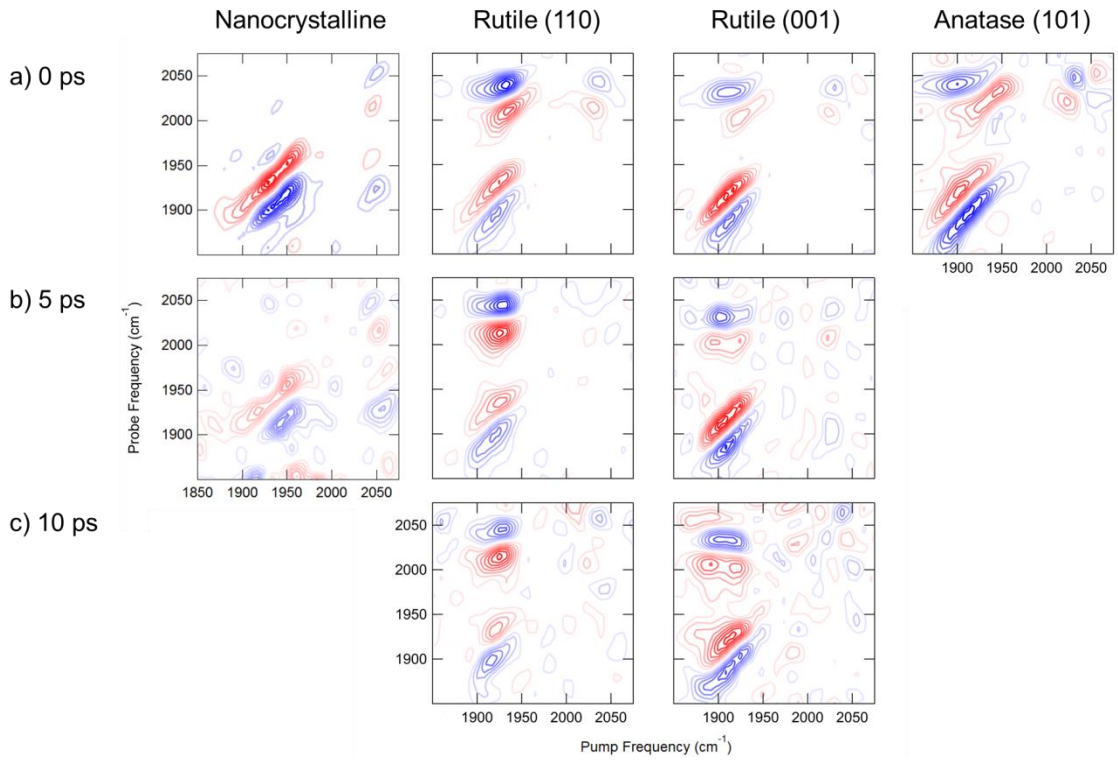

Figure 5.5 2D SFG surfaces of $Re(CO)_3$ on different TiO_2 surfaces as a function of waiting time, τ_2.

5.3.6 Spectral Diffusion Dynamics

In addition to resolving vibrational structure and couplings, 2D SFG is capable of measuring spectral diffusion dynamics: the timescale corresponding to molecules sampling the different microstructures available within a heterogeneously broadened sample. Figure 5.5 displays the time evolution of the 2D SFG spectra of the catalyst on nanostructured and single-crystalline surfaces. By varying the waiting time, τ_2, the spectral evolution of the system can be followed, and the initially strong diagonal

features decay as the waiting time increases due to vibrational relaxation. The diagonal features, which are initially elongated along the diagonal due to inhomogeneous broadening, show a sub-structure that persists at 5 ps. We have previously attributed this sub-structure to a structural heterogeneity.[29] Previous bulk 2D IR studies of TiO_2 nanoparticles have suggested the heterogeneity could be in part due to aggregated molecules. Here, we do not see any sub-structure in the symmetric stretch at the single crystal surfaces that would indicate aggregation, such as distinct intensities at slightly different vibrational frequencies within the symmetric stretch region.[42]

The linewidth along the diagonal reports on the inhomogeneous broadening, while the antidiagonal linewidth of same diagonal mode is a measure of the homogeneous broadening.[44] As a homogeneous system spectrally diffuses and samples the available frequency space, the diagonal linewidth decreases, and the features become less elongated and more spherical. The spectral diffusion dynamics can be characterized by the waiting time evolution, τ_2, of the center line slope[53,54] (CLS), which is related to the frequency-frequency correlation function. The measured CLS for the different TiO_2 surfaces is shown in Figure 5.6. The CLS decays more quickly for rutile (110), so the molecules on that surface are more homogeneous than on rutile (001) and the nanoparticles. The anatase (101) slope is in between the slope seen on the two rutile surfaces.

Since the rutile (110) surface is rather homogeneous, the molecules on that surface are likely in the same environment and have the same binding geometries. Meanwhile, the catalyst on nanocrystalline and rutile (001) TiO_2 surfaces are more

disordered, with more than one binding mode. In particular, the nanocrystalline surface maintains discrete features at longer waiting times, indicating multiple distinct local environments.[29] Since the compound was unstable on the anatase (101) surface, multiple waiting times were not measured.

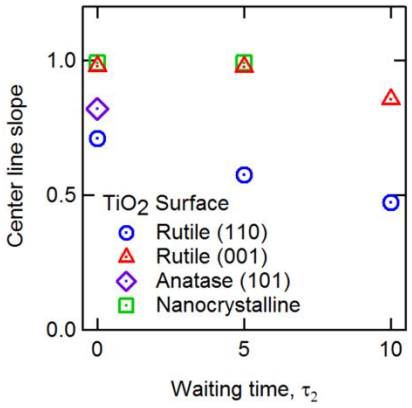

Figure 5.6 Center line slope measured at different waiting times for $Re(CO)_3$ on different TiO_2 surfaces.

5.4 Conclusions

The technologically important molecular catalyst-single crystal TiO_2 CO_2 reduction system is found to be significantly different than the nanocrystalline TiO_2 system in regards to molecular orientation, vibrational relaxation dynamics, spectral diffusion, and intramolecular vibrational coupling. The catalysts on single crystal TiO_2 are generally more ordered and perpendicular to the surface. The vibrational energy in the A′(1) mode was found to quickly (within 5 ps) relax into the low frequency modes on rutile (110). While a bit slower on rutile (001), the vibrational relaxation of the

symmetric mode is still significantly faster compared to nanocrystalline TiO_2. By monitoring the CLS of the low frequency feature, rutile (110) was found to be more homogeneous than the other single crystal surfaces, and the nanoparticles exhibited a static structural heterogeneity.

Furthermore, the coupling was much stronger on the single crystal surfaces when comparing to the nanocrystalline system. Therefore, $Re(CO)_3$ has a distinctly different interaction when bound to TiO_2 single crystal surfaces compared to nanoparticles, which must be carefully understood in order to rationally design catalytic systems. If indeed as earlier mentioned, TiO_2 acts as an electron sink for the reaction, but first requires vibrational relaxation, then the rutile (110) surface may be better than (001) for this type of reaction. The anatase (101) surface has an intermediate degree of coupling and may not perform as well as rutile (110). The carbonyl vibrational modes are highly sensitive to the local electronic environment. Such a large perturbation in the electronic structure around the rhenium atom will certainly have an influence on the catalytic cycle, as CO_2 is reduced at the metal center. These differences, particularly between the single crystal and nanoparticle environments, have significant implications for the design and optimization of nanostructured high surface area catalysts. Interferometric 2D SFG has thus proven to be a powerful tool for obtaining unique structural and dynamic information of catalytic monolayers.

5.5 References

(1) Fujishima, A.; Rao, T. N.; Tryk, D. A. Titanium Dioxide Photocatalysis. *J. Photochem. Photobiol. C Photochem. Rev.* **2000**, *1*, 1–21.

(2) Ulrike, D. The Surface Science of Titanium Dioxide. *Surf. Sci. Rep.* **2003**, *48*, 53–229.

(3) Windle, C. D.; Pastor, E.; Reynal, A.; Whitwood, A. C.; Vaynzof, Y.; Durrant, J. R.; Perutz, R. N.; Reisner, E. Improving the Photocatalytic Reduction of CO_2 to CO through Immobilisation of a Molecular Re Catalyst on TiO_2. *Chem. Eur. J.* **2015**, *21*, 3746–3754.

(4) Cecchet, F.; Alebbi, M.; Bignozzi, C. A.; Paolucci, F. Efficiency Enhancement of the Electrocatalytic Reduction of CO_2: Fac-[Re(v-bpy)$(CO)_3$Cl] Electropolymerized onto Mesoporous TiO_2 Electrodes. *Inorganica Chim. Acta* **2006**, *359*, 3871–3874.

(5) Takeda, H.; Ohashi, M.; Tani, T.; Ishitani, O.; Inagaki, S. Enhanced Photocatalysis of rhenium(I) Complex by Light-Harvesting Periodic Mesoporous Organosilica. *Inorg. Chem.* **2010**, *49*, 4554–4559.

(6) Liu, C.; Dubois, K.; Louis, M.; Vorushilov, A.; Li, G. Photocatalytic CO_2 Reduction and Surface Immobilization of a Tricarbonyl Re (I) Compound Modified with Amide Groups. *ACS Catal.* **2013**, *3*, 655-662.

(7) Abdellah, M.; El-Zohry, A. M.; Antila, L. J.; Windle, C. D.; Reisner, E.; Hammarström, L. Time-Resolved IR Spectroscopy Reveals a Mechanism with TiO_2 as a Reversible Electron Acceptor in a TiO_2 −Re Catalyst System for CO_2

Photoreduction. *J. Am. Chem. Soc.* **2017**, *139*, 1226–1232.

(8) Grätzel, M. Dye-Sensitized Solar Cells. *J. Photochem. Photobiol. C.* **2003**, *4*, 145-153.

(9) Miao, L.; Tanemura, S.; Toh, S.; Kaneko, K.; Tanemura, M. Preparation and Characterization of Rutile-TiO_2 Nanorods. *J. Mater. Sci. Technol.* **2004**, *20*, 59–62.

(10) Liu, B.; Aydil, E. S. Growth of Oriented Single-Crystalline Rutile TiO_2 Nanorods on Transparent Conducting Substrates for Dye-Sensitized Solar Cells. *J. Am. Chem. Soc.* **2009**, *131*, 3985–3990.

(11) Li, Y.; Guo, M.; Zhang, M.; Wang, X. Hydrothermal Synthesis and Characterization of TiO_2 Nanorod Arrays on Glass Substrates. *Mater. Res. Bull.* **2009**, *44*, 1232–1237.

(12) Wang, S.-M.; Dong, W.-W.; Tao, R.-H.; Deng, Z.-H.; Shao, J.-Z.; Hu, L.-H.; Zhu, J.; Fang, X.-D. Optimization of Single-Crystal Rutile TiO_2 Nanorod Arrays Based Dye-Sensitized Solar Cells and Their Electron Transport Properties. *J. Power Sources* **2013**, *235*, 193–201.

(13) Huang, H.; Pan, L.; Lim, C. K.; Gong, H.; Guo, J.; Tse, M. S.; Tan, O. K. Hydrothermal Growth of TiO_2 Nanorod Arrays and in Situ Conversion to Nanotube Arrays for Highly Efficient Quantum Dot-Sensitized Solar Cells. *Small* **2013**, *9*, 3153–3160.

(14) Zhang, W.; Xie, Y.; Xiong, D.; Zeng, X.; Li, Z.; Wang, M.; Cheng, Y.-B.; Chen, W.; Yan, K.; Yang, S. TiO_2 Nanorods: A Facile Size- and Shape-Tunable

Synthesis and Effective Improvement of Charge Collection Kinetics for Dye-Sensitized Solar Cells. *ACS Appl. Mater. Interfaces* **2014**, *6*, 9698–9704.

(15) Jarosz, M.; Syrek, K.; Kapusta-Kołodziej, J.; Mech, J.; Małek, K.; Hnida, K.; Łojewski, T.; Jaskuła, M.; Sulka, G. D. Heat Treatment Effect on Crystalline Structure and Photoelectrochemical Properties of Anodic TiO_2 Nanotube Arrays Formed in Ethylene Glycol and Glycerol Based Electrolytes. *J. Phys. Chem. C* **2015**, *119*, 24182–24191.

(16) Fakharuddin, A.; Di Giacomo, F.; Palma, A. L.; Matteocci, F.; Ahmed, I.; Razza, S.; D'Epifanio, A.; Licoccia, S.; Ismail, J.; Di Carlo, A.; et al. Vertical TiO_2 Nanorods as a Medium for Stable and High-Efficiency Perovskite Solar Modules. *ACS Nano* **2015**, *9*, 8420–8429.

(17) Guo, W.; Xu, C.; Wang, X.; Wang, S.; Pan, C.; Lin, C.; Wang, Z. L. Rectangular Bunched Rutile TiO_2 Nanorod Arrays Grown on Carbon Fiber for Dye-Sensitized Solar Cells. *J. Am. Chem. Soc.* **2012**, *134*, 4437–4441.

(18) Lu, Y.; Choi, D.; Nelson, J.; Yang, O.-B.; Parkinson, B. A. Adsorption, Desorption, and Sensitization of Low-Index Anatase and Rutile Surfaces by the Ruthenium Complex Dye N3. *J. Electrochem. Soc.* **2006**, *153*, E131–E137.

(19) Yang, H. G.; Sun, C. H.; Qiao, S. Z.; Zou, J.; Liu, G.; Smith, S. C.; Cheng, H. M.; Lu, G. Q. Anatase TiO_2 Single Crystals with a Large Percentage of Reactive Facets. *Nature* **2009**, *453*, 638–642.

(20) Spitler, M. T.; Parkinson, B. A. Dye Sensitization of Single Crystal Semiconductor Electrodes. *Acc. Chem. Res.* **2009**, *42*, 2017–2029.

(21) Liu, G.; Yu, J. C.; Lu, G. Q.; Cheng, H.-M. Crystal Facet Engineering of Semiconductor Photocatalysts: Motivations, Advances and Unique Properties. *Chem. Commun.* **2011**, *47*, 6763–6783.

(22) Wu, X.; Chen, Z.; Qing, G.; Wang, L. Nanosized Anatase TiO_2 Single Crystals with Tunable Exposed (001) Facets for Enhanced Energy Conversion Efficiency of Dye-Sensitized Solar Cells. *Adv. Funct. Mater.* **2001**, *21*, 4167–4172.

(23) Lin, H.; Li, L.; Zhao, M.; Huang, X.; Chen, X.; Li, G.; Yu, R. Synthesis of High-Quality Brookite TiO_2 Single-Crystalline Nanosheets with Specific Facets Exposed: Tuning Catalysts from Inert to Highly Reactive. *JACS* **2012**, *134*, 8328–8331.

(24) Tachikawa, T.; Yamashita, S.; Majima, T. Evidence for Crystal-Face-Dependent TiO_2 Photocatalysis from Single-Molecule Imaging and Kinetic Analysis. *J. Am. Chem. Soc* **2011**, *133*, 7197–7204.

(25) Yu, J.; Low, J.; Xiao, W.; Zhou, P.; Jaroniec, M. Enhanced Photocatalytic CO_2-Reduction Activity of Anatase TiO_2 by Coexposed {001} and {101} Facets. *J. Am. Chem. Soc.* **2014**, *136*, 8839–8842.

(26) Ong, W.-J.; Tan, L.-L.; Chai, S.-P.; Yong, S.-T.; Mohamed, A. R. Facet-Dependent Photocatalytic Properties of TiO_2-Based Composites for Energy Conversion and Environmental Remediation. *Chem Sus Chem* **2014**, *7*, 690–719.

(27) Li, C.; Koenigsmann, C.; Ding, W.; Rudshteyn, B.; Yang, K. R.; Regan, K. P.;

Konezny, S. J.; Batista, V. S.; Brudvig, G. W.; Schmuttenmaer, C. A.; et al. Facet-Dependent Photoelectrochemical Performance of TiO_2 Nanostructures: An Experimental and Computational Study. *J. Am. Chem. Soc.* **2015**, *137*, 1520–1529.

(28) Guo, Q.; Zhou, C.; Ma, Z.; Ren, Z.; Fan, H.; Yang, X. Elementary Photocatalytic Chemistry on TiO_2 Surface. *Chem Soc Rev* **2016**, *45*, 3701.

(29) Vanselous, H.; Stingel, A. M.; Petersen, P. B. Interferometric 2D Sum Frequency Generation Spectroscopy Reveals Structural Heterogeneity of Catalytic Monolayers on Transparent Materials. *J. Phys. Chem. Lett.* **2017**, *8*, 825–830.

(30) Xiong, W.; Laaser, J. E.; Mehlenbacher, R. D.; Zanni, M. T. Adding a Dimension to the Infrared Spectra of Interfaces Using Heterodyne Detected 2D Sum-Frequency Generation (HD 2D SFG) Spectroscopy. *Proc. Natl. Acad. Sci. U.S.A.* **2011**, *108*, 20902–20907.

(31) Wang, J.; Clark, M. L.; Li, Y.; Kaslan, C. L.; Kubiak, C. P.; Xiong, W. Short-Range Catalyst–Surface Interactions Revealed by Heterodyne Two-Dimensional Sum Frequency Generation Spectroscopy. *J. Phys. Chem. Lett.* **2015**, *6*, 4204–4209.

(32) Vanselous, H.; Petersen, P. B. Extending the Capabilities of Heterodyne-Detected Sum-Frequency Generation Spectroscopy : Probing Any Interface in Any Polarization Combination. *J. Phys. Chem. C* **2016**, *120*, 8175–8184.

(33) Calabrese, C.; Vanselous, H.; Petersen, P. B. Deconstructing the Heterogeneity

of Surface-Bound Catalysts: Rutile Surface Structure Affects Molecular Properties. *J. Phys. Chem. C* **2016**, *120*, 1515–1522.

(34) Xiong, W.; Laaser, J. E.; Paoprasert, P.; Franking, R. A.; Hamers, R. J.; Gopalan, P.; Zanni, M. T. Transient 2D IR Spectroscopy of Charge Injection in Dye-Sensitized Nanocrystalline Thin Films. *J. Am. Chem. Soc.* **2009**, *131*, 18040–18041.

(35) Laaser, J. E.; Christianson, J. R.; Oudenhoven, T. A.; Joo, Y.; Gopalan, P.; Schmidt, J. R.; Zanni, M. T. Dye Self-Association Identified by Intermolecular Couplings between Vibrational Modes As Revealed by Infrared Spectroscopy, and Implications for Electron Injection. *J. Phys. Chem. C* **2014**, *118*, 5854–5861.

(36) Oudenhoven, T. A.; Joo, Y.; Laaser, J. E.; Gopalan, P.; Zanni, M. T. Dye Aggregation Identified by Vibrational Coupling Using 2D IR Spectroscopy. *J. Chem. Phys.* **2015**, *142*, 212449.

(37) Shen, Y. R. *The Principles of Nonlinear Optics*; John Wiley & Sons, Inc.: New York, 1984.

(38) Shen, Y. R. Phase-Sensitive Sum-Frequency Spectroscopy. *Annu. Rev. Phys. Chem.* **2013**, *64*, 129–150.

(39) Nihonyanagi, S.; Mondal, J. A; Yamaguchi, S.; Tahara, T. Structure and Dynamics of Interfacial Water Studied by Heterodyne-Detected Vibrational Sum-Frequency Generation. *Annu. Rev. Phys. Chem.* **2013**, *64*, 579–603.

(40) Anfuso, C. L.; Xiao, D.; Ricks, A. M.; Negre, C. F. A.; Batista, V. S.; Lian, T.

Orientation of a Series of CO_2 Reduction Catalysts on Single Crystal TiO_2 Probed by Phase-Sensitive Vibrational Sum Frequency Generation Spectroscopy (PS-VSFG). *J. Phys. Chem. C* **2012**, *116*, 24107–24114.

(41) Li, Z.; Wang, J.; Li, Y.; Xiong, W. Solving the "Magic Angle" Challenge in Determining Molecular Orientation Heterogeneity at Interfaces. *J. Phys. Chem. C* **2016**, *120*, 20239–20246.

(42) Oudenhoven, T. A.; Joo, Y.; Laaser, J. E.; Gopalan, P.; Zanni, M. T. Dye Aggregation Identified by Vibrational Coupling Using 2D IR Spectroscopy. *J. Chem. Phys.* **2015**, *142*, 212449.

(43) Ge, A.; Rudshteyn, B.; Psciuk, B. T.; Xiao, D.; Song, J.; Anfuso, C. L.; Ricks, A. M.; Batista, V. S.; Lian, T. Surface-Induced Anisotropic Binding of a Rhenium CO_2-Reduction Catalyst on Rutile TiO_2 (110) Surfaces. *J. Phys. Chem. C* **2016**, *120*, 20970–20977.

(44) Hamm, P.; Zanni, M. *Concepts and Methods of 2D Infrared Spectroscopy*; Cambridge University Press, 2011.

(45) Fayer, M. D. *Ultrafast Infrared Vibrational Spectroscopy*; CRC Press, 2013; Vol. 2.

(46) Rosenfeld, D. E.; Gengeliczki, Z.; Smith, B. J.; Stack, T. D. P.; Fayer, M. D. Structural Dynamics of a Catalytic Monolayer Probed by Ultrafast 2D IR Vibrational Echoes. *Science* **2011**, *334*, 634–639.

(47) Kraack, J. P.; Lotti, D.; Hamm, P. Ultrafast, Multidimensional Attenuated Total Reflectance Spectroscopy of Adsorbates at Metal Surfaces. *J. Phys. Chem. Lett.*

2014, *5*, 2325–2329.

(48) Kraack, J. P.; Hamm, P. Surface-Sensitive and Surface-Specific Ultrafast Two-Dimensional Vibrational Spectroscopy. *Chem. Rev.* DOI: 10.1021/acs.chemrev.6b00437

(49) Cervetto, V.; Helbing, J.; Bredenbeck, J.; Hamm, P. Double-Resonance versus Pulsed Fourier Transform Two-Dimensional Infrared Spectroscopy: An Experimental and Theoretical Comparison. *J. Chem. Phys.* **2004**, *121*, 5935–5942.

(50) Shim, S.-H.; Strasfeld, D. B.; Ling, Y. L.; Zanni, M. T. Automated 2D IR Spectroscopy Using a Mid-IR Pulse Shaper and Application of This Technology to the Human Islet Amyloid Polypeptide. *Proc. Natl. Acad. Sci.* **2007**, *104*, 14197–14202.

(51) Shim, S.-H.; Zanni, M. T. How to Turn Your Pump-Probe Instrument into a Multidimensional Spectrometer: 2D IR and Vis Spectroscopies via Pulse Shaping. *Phys. Chem. Chem. Phys.* **2009**, *11*, 748–761.

(52) Ghosh, A.; Ho, J.-J.; Serrano, A. L.; Skoff, D. R.; Zhang, T.; Zanni, M. T. Two-Dimensional Sum-Frequency Generation (2D SFG) Spectroscopy: Summary of Principles and Its Application to Amyloid Fiber Monolayers. *Faraday Discuss.* **2015**, *177*, 493.

(53) Kwak, K.; Park, S.; Finkelstein, I. J.; Fayer, M. D. Frequency-Frequency Correlation Functions and Apodization in Two-Dimensional Infrared Vibrational Echo Spectroscopy: A New Approach. *J. Chem. Phys.* **2007**, *127*,

124503.

(54) Kwak, K.; Rosenfeld, D. E.; Fayer, M. D. Taking Apart the Two-Dimensional Infrared Vibrational Echo Spectra: More Information and Elimination of Distortions. *J. Chem. Phys.* **2008**, *128*, 204505.

(55) Laaser, J. E.; Zanni, M. T. Extracting Structural Information from the Polarization Dependence of One- and Two-Dimensional Sum Frequency Generation Spectra. *J. Phys. Chem. A* **2013**, *117*, 5875–5890.

(56) Hexter, R. M. Intermolecular Coupling of Vibrations in Molecular Crystals: A Vibrational Exciton Approach. *J. Chem. Phys.* **1960**, *33*, 1833–1841.

(57) Hamm, P.; Lim, M.; Hochstrasser, R. M. Structure of the Amide I Band of Peptides Measured by Femtosecond Nonlinear-Infrared Spectroscopy. *J Phys Chem B* **1998**, *102*, 6123–6138.

(58) Ramasesha, K.; De Marco, L.; Mandal, A.; Tokmakoff, A. Water Vibrations Have Strongly Mixed Intra- and Intermolecular Character. *Nat. Chem.* **2013**, *5*, 935–940.

(59) Smieja, J. M.; Kubiak, C. P. Re(bipy-tBu)$(CO)_3$Cl-Improved Catalytic Activity for Reduction of Carbon Dioxide: IR-Spectroelectrochemical and Mechanistic Studies. *Inorg. Chem.* **2010**, *49*, 9283–9289.

(60) Skibinski, E. S.; Song, A.; DeBenedetti, W. J. I.; Ortoll-Bloch, A. G.; Hines, M. A. Solution Deposition of Self-Assembled Benzoate Monolayers on Rutile (110): Effect of π−π Interactions on Monolayer Structure. *J. Phys. Chem. C* **2016**, *120*, 11581–11589.

(61) Ghosh, A.; Smits, M.; Bredenbeck, J.; Dijkhuizen, N.; Bonn, M. Femtosecond Time-Resolved and Two-Dimensional Vibrational Sum Frequency Spectroscopic Instrumentation to Study Structural Dynamics at Interfaces. *Rev. Sci. Instrum.* **2008**, *79*, 93907.

CHAPTER 6

TWO DIMENSIONAL SFG OF WATER: VIBRATIONAL RELAXATION OF WATER AT HYDROPHOBIC SURFACES IS REMARKABLY FASTER THAN BULK WATER

6.1 Introduction

Water is a remarkable liquid and often considered the solvent of life, being a requirement for the creation and evolution of life as we know it.[1,2] Therefore, in order to understand processes involved in biological functions for example, a solid understanding of the structure and dynamics of water in biological settings is needed. Many of the unique properties of water are governed by the structure and dynamics of the intermolecular hydrogen bonding (H-bonding) network.

Ultrafast vibrational spectroscopy, in particular two-dimensional infrared (2D IR), coupled with molecular dynamics (MD) simulations, have proven to be an ideal tool to observe such fast (femtosecond and picosecond) dynamics.[3–11] These experiments have revealed that the hydrogen-bonded network in bulk water exhibits extremely fast (~100 fs) hydrogen-bond rearranging dynamics with large amplitude jump motions that result in hydrogen bond switching on the ~1.5 ps time scale. In neat H_2O the OH vibrations are very strongly coupled resulting in delocalized vibrational excitons spread over several water molecules, strikingly different than the typical concept of normal modes (symmetric and asymmetric stretches) in gas phase

spectroscopy.

Meanwhile, when water is at an interface, the bulk hydrogen-bonding network is disrupted. Interfacial water is incredibly important for chemical interactions occurring at hydrophobic interfaces, such as protein folding and amyloid fiber aggregation which both involve water displacement at a hydrophobic surface. To probe only the interfacial layer of water without an overwhelming contribution from the bulk, surface-specific sum frequency generation (SFG) vibrational spectroscopy has been utilized. While 2D IR is sensitive enough to study a single monolayer in a tethered dye-solvent system, this technique cannot be used to separate interface water from bulk water.[12] As a second-order nonlinear process, under the electric dipole approximation, SFG is only generated at the interface since isotropic signals from the bulk cancel.[13–15] Using this technique, the structure of water at different hydrophobic interfaces, such as air, has been studied. Interestingly, it seems that water does not interact with all hydrophobic surfaces in the same way. In 1994, the spectrum of the air-water and hydrophobic self-assembled monolayer (SAM)-water interfaces were found to be unique.[16] Two main features are present in the interfacial water spectrum and are often described as strongly (lower frequency ~3200 cm^{-1}) and weaker (higher frequency ~3400 cm^{-1}) hydrogen bonding species. Shen and co-workers attributed the larger intensity strongly H-bonded species at the SAM-water interface to a rigid wall confining the H-bonded network into a more ice-like arrangement when compared to the air-water interface.[16] This is perhaps an oversimplification but is consistent with the well-established correlation between H-bond strength and vibrational frequency of

OH stretches in solids.[17] The interfacial water spectrum has alternatively been described as a combination of inter and intramolecular coupling.[18–21] Through isotopic dilution, the intramolecular coupling between the OH stretch and the overtone of the OH bend can be suppressed. We note that this coupling explanation has been questioned due to a discrepancy in data collected by different research groups.[22]

The biologically relevant interface to study would be pure H_2O (rather than D_2O or HOD) at a rigid neutral hydrophobic surface (rather than air). The dynamics of the dangling OH at the water-OTS modified silica interface have been studied with time-resolved SFG experiments[26–28] and MD simulations[29]. Here, the free OH was found to have slower relaxation dynamics than bulk water and very fast dephasing times, while jumping to a new H-bonded partner was faster than in bulk. Meanwhile, the dynamics of the hydrogen-bonded region has yet to be studied for a neutral condensed phase hydrophobic – water interface.

In order to obtain the degree of information obtained thus far for bulk water, a surface-specific analog of 2D IR is needed. Heterodyne detected (HD) 2D SFG is rigorously analogous to 2D IR experiments, which also measure the absorptive lineshape directly. A two-dimensional map can be created with a series of narrowband IR pump – SFG probe experiments by varying the pump wavelength. Such experiments have been performed on a number of different air-water interfaces, thoroughly summarized in Ref. 30. In particular, at the air-pure-H_2O interface, a frequency dependent spectral diffusion was observed, with the strongly H-bonded region showing spectral diffusion dynamics at least 1.5 times slower than in the bulk

(250 fs versus ~50-150 fs for the bulk[6,11]), attributed to a lower density of water molecules at the surface, and the weaker H-bonded region slowed even more to ~500 fs, attributed to localization at the interface reducing the intermolecular vibrational coupling energy transfer pathway.[31] However, these measurements, performed in the scanning pump geometry of 2D SFG, possess a temporal resolution limited to the duration of the pump pulse- a narrowband pump of 100 cm^{-1} will be approximately 200 fs broad in time. Our interferometric broadband pump pulse pair technique has both higher temporal and spectral resolution, which is especially important for observing these ultrafast dynamics.[32–35] We show, for the first time, that the vibrational relaxation dynamics of interfacial water at a condensed phase hydrophobic surface are essentially just as fast as those in the bulk, which is in contrast to the air-water interface which has slower vibrational dynamics than in the bulk. While both of these surfaces can be considered hydrophobic, the different vibrational dynamics indicate very different environments and intermolecular interactions. Understand the cause of these differences may lead to a further understanding of hydrophobic interfaces important for biological processes such as protein folding.

6.2 Experimental Details

6.2.1 Sample Preparation

CaF_2 hemicylindrical prisms (10x10mm diameter, Crystran Limited) with a 125 nm SiO_2 layer deposited through atomic layer deposition were coated on one half with a 150 nm layer of gold, and the other half was modified with an octadecyltrichlorosilane

self-assembled monolayer according to published literature procedures.[36] Ultrapure water (Millipore MilliQ, 18.2 MΩ•cm, ≤ 5 ppb total organic carbon) was used throughout the experiment.

6.2.2 2D SFG Experiments

The experimental setup for the heterodyne-detected SFG spectra is described in Chapter 3 and for the 2D SFG spectra in Chapters 4 and 5. For this particular system, the IR pulses were centered at 3220 cm^{-1} with a bandwidth of 300 cm^{-1}. The relative IR pump pulse timing, and hence the free-induction decay, was scanned from -150 fs to 400 fs in step sizes of 2 fs to create the ω_1 axis. This corresponds to an excitation frequency resolution of 60 cm^{-1}. Meanwhile, a cross-correlation signal measured on gold at the backside of the prism between IR_{pump}, IR_{probe}, and visible pulses (IIV), shown in Figure 6.1, displayed a Gaussian envelope with full-width at half-maximum of 114 fs, which determines the resolution in τ_2, and corresponds to an IR pulse duration of 80 fs. These short pulses are critical for resolving ultrafast vibrational dynamics such as those in water.

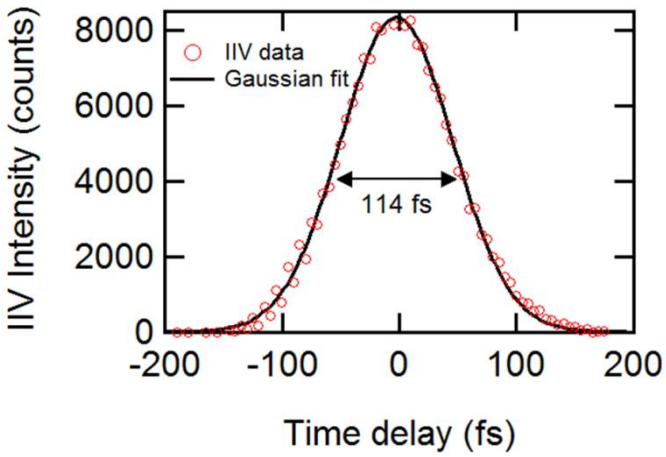

Figure 6.1 IR pump+IR probe+Visible (IIV) cross-correlation with full-width at half-maximum of 114 fs corresponds to a pulse duration of 80 fs.

6.3 Results and Discussion

6.3.1 Interfacial Structure through HD SFG

The features in the H-bonding region of the interfacial water spectrum, particularly at the air-water interface, have been generally described in two ways: 1) two distinct strongly and weaker H-bonded regions and 2) a H-bonded region with a dip due to a Fermi resonance with the overtone of the OH bend mode. HD SFG can be utilized in order to simplify the spectrum, i.e. remove interference from real and imaginary components (dispersive and absorptive line shapes, respectively).[37–39] The HD SFG spectrum of water at OTS is shown in Figure 6.2. Two main features can be seen in the imaginary component: one strong feature around 3250 cm^{-1} due to strongly H-bonded water molecules and a weaker shoulder around 3500 cm^{-1} from weaker H-

bonding. Thus, the interfacial water molecules display an overall broad hydrogen-bonded structure. This spectrum is consistent with previous homodyne-detected SFG measurements of this interface.[16,40,41] Furthermore, both features are positive, indicating that on average the hydrogen bonds are pointing away from the hydrophobic monolayer and towards the bulk. Any OH bonds in the plane of the interface would not contribute to the signal, and dangling OH bonds pointing toward the surface were outside of the spectral window of the current study. Therefore, within the probe depth, the OH bonds which are not oriented in the plane of the interface are repelled from the OTS and the water molecules are oriented towards the bulk with their lone pair electrons directed towards the OTS monolayer and away from the bulk water.

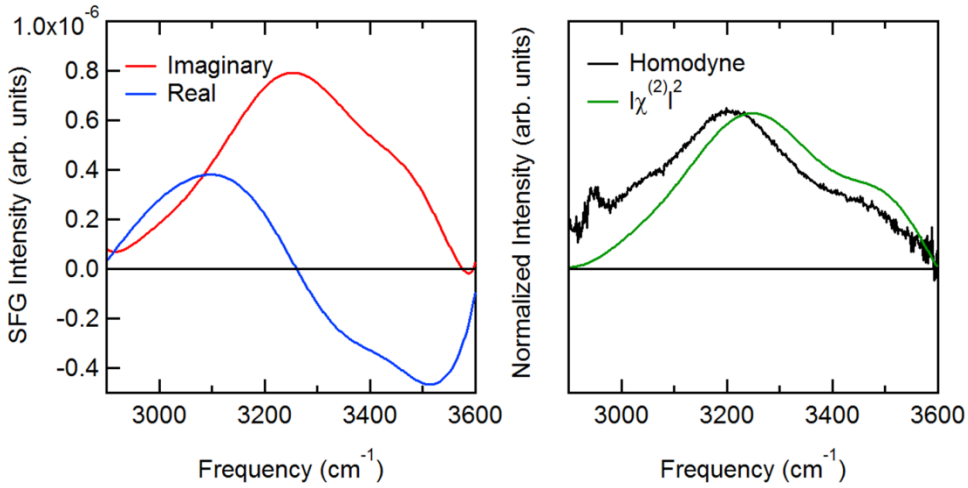

Figure 6.2 Heterodyne-detected SFG spectrum of H_2O at the hydrophobic OTS modified surface. Left: this technique resolves real (blue trace) and imaginary (red trace) components of the spectrum. Right: the square magnitude (green) is similar in shape to the homodyne measurement (black).

6.3.2 Vibrational Dynamics through Time-Resolved SFG

Broadband IR-pump - SFG probe experiments can reveal interfacial vibrational relaxation dynamics. Figure 6.3 shows the SFG response as a function of time delay between the IR pump and SFG probe. A ground state bleach is observed at 3150 cm^{-1}, and an induced feature is also observed. This band is blue-shifted with respect to the bleach. Accordingly, this is not the 1→2 transition but is often described as a slightly thermally excited "hot ground state". While this feature is spectrally similar to what would be seen from a temperature increase, as a shift to higher frequencies due to thermal excitation weakens the H-bonding throughout the water network, due to the rapid time scale of the energy relaxation, this feature cannot be a thermally equilibrated state but has recently been attributed instead to strong coupling to low-frequency intermolecular modes in bulk measurements.[11]

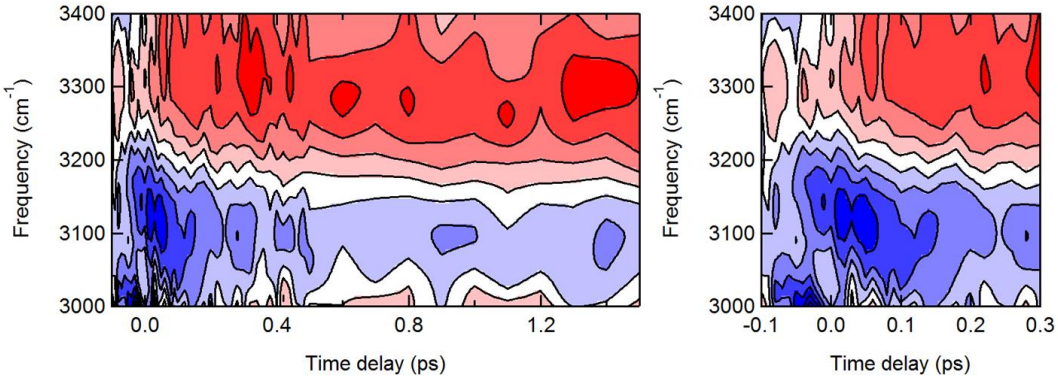

Figure 6.3 IR pump – SFG probe spectrum of the water-OTS interface. The right panel highlights the fast dynamics before 300 fs delay time between IR pump and SFG probe.

To better quantify the vibrational dynamics, the lower frequency signal

between 3040 and 3200 cm^{-1} was averaged, as was the higher frequency spanning 3250-3400 cm^{-1}. These two regions were fit to exponential functions, with the resulting fits shown in Figure 6.4. The bleach (Figure 6.4, bottom) displayed single exponential relaxation dynamics whose lifetime was 160±26 fs. Meanwhile, the mode at approximately 3300 cm^{-1} arising from coupling to lower frequency modes, within signal to noise, exhibited an identical lifetime, suggesting population relaxation from one state into another. Therefore, the 3300 cm^{-1} signal decay was fit to two timescales, one ultrafast component was constrained to 160 fs, corresponding to the bleach timescale, and a longer intermolecular coupling relaxation timescale that could not be fit accurately with only measuring to 1.6 ps.

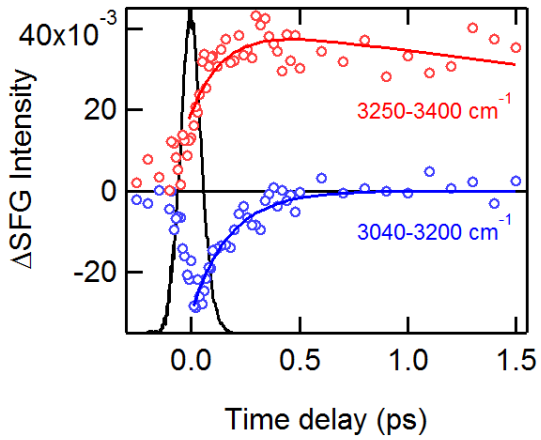

Figure 6.4 Averaged pump-probe regions (open circles) and their corresponding fits (solid lines). IR pump + IR probe + Visible cross-correlation is shown in black.

A bleach in the higher frequency weaker H-bonded region is not seen in the pump-probe data, which can be attributed to a cancellation of the negative bleach and the positive hot ground state, which grows in immediately, as seen in the 2D SFG spectra

discussed below.

The broadband IR pump – SFG probe experiments reveal ultrafast vibrational relaxation at the solid hydrophobic interface even faster than that observed in bulk water (~300 fs), in contrast to the air-water interface displaying slower dynamics. Therefore, confinement of a rigid SAM does not seem to slow down the relaxation of the OH stretch, at least of the strongly H-bonded species. An obvious follow up question is: how is the energy distributed among the molecules at the interface?

6.3.3 Vibrational Energy Distribution through 2D SFG

Bulk water displays delocalized vibrational energy spanning 1-6 water molecules, observed through ultrafast spectral diffusion dynamics and simulations.[11,42] Recent 2D SFG experiments in the scanning pump geometry and MD simulations have presented a considerably different picture of water in contact with air, with spectral diffusion dynamics significantly slower than in the bulk.[31,43]

Interferometric 2D SFG measurements for pure water in contact with an OTS-coated SiO_2 surface are shown in Figure 6.5 at a number of different waiting times, τ_2. Beginning at $\tau_2 = 0$ ps, there is a clear bleach at ($\omega_{pump} = 3150$ cm^{-1}, $\omega_{probe} = 3250$ cm^{-1}) from the strongly H-bonded species. The positive feature red-shifted from the bleach along the probe axis is the induced absorption from the 1→2 transition of the OH stretch.

The most striking feature of the 2D spectrum is the homogeneity present at $\tau_2 = 0$ ps. Rather than elongation along the diagonal, indicative of some initial

inhomogeneous broadening arising from molecules in slightly different environments observed in the bulk, these spectra are homogeneous within the time resolution of the experiment. This observation is consistent with but even faster than the exciton hopping picture in the bulk system, and strongly contrasts the dynamics seen at the air-water interface. Therefore, water in contact with a rigid hydrophobic surface is extremely bulk-like in its behavior. At later delay times, the induced feature attributed to thermalization or coupling to lower frequency modes grows in and dominates the spectrum by 400 fs, also supporting ultrafast interfacial energy transfer.

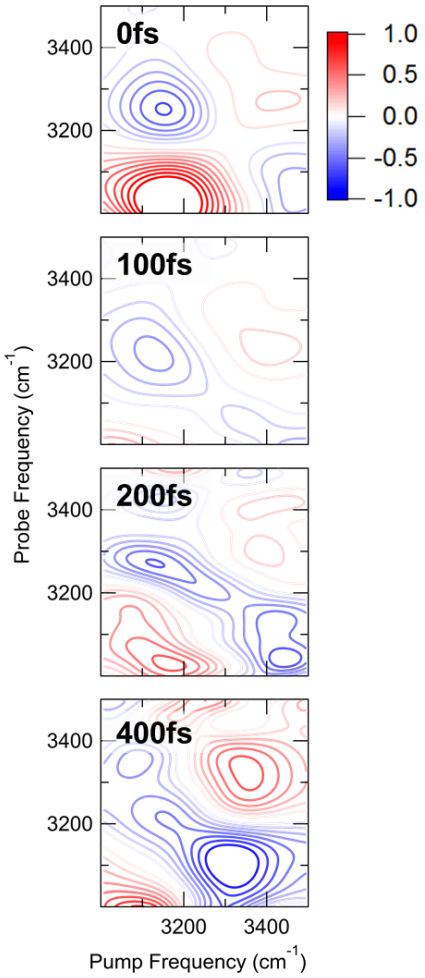

Figure 6.5 Interferometric 2D SFG data of the H_2O – OTS interface at different waiting times, τ_2. All 2D spectra are shown at equal contour levels.

6.4 Conclusions

In this study, a series of ultrafast vibrational experiments were performed on the interface between water and OTS modified fused silica to understand the interfacial hydrogen bonding environment in terms of surface structure and vibrational energy redistribution. Previous bulk 2D IR experiments on water revealed ultrafast vibrational

dynamics, while scanning narrowband excitation SFG experiments by the Bonn group showed that the vibrational dynamics of water at the air interface were slower than those found in the bulk 2D IR experiments. By incorporating the experimental advances made throughout this dissertation, including phase-stable heterodyne-detected SFG at buried interfaces and interferometric 2D SFG experiments with an external local oscillator, we have found that the vibrational dynamics of water at a different hydrophobic interface consisting of an octadecyltrichlorosilane self-assembled monolayer are even faster than those found in the bulk. The heterodyne-detected SFG spectrum described a surface in which all water molecules had their OH groups pointing away from the hydrophobic OTS and towards the bulk water. Time-resolved IR pump – SFG probe experiments revealed relaxation dynamics of the hydrogen-bonded OH stretch mode on the order of 200 fs. Finally, interferometric 2D SFG showed the interfacial environment as essentially homogeneous, consistent with the idea of delocalized vibrational energy. Through these experiments, the overall picture of water at a condensed phase hydrophobic interface is that of a minimally perturbed, highly coupled interface, schematically represented in Figure 6.6, in contrast to previous studies of the air-water and charged lipid-water interfaces. The air-water interface was suggested to have slower-than-bulk dynamics due to the lower density of molecules at the surface. Here, at the OTS monolayer, the density is not lower and the transition dipoles are more aligned than in the bulk, thus creating faster-than-bulk vibrational dynamics.

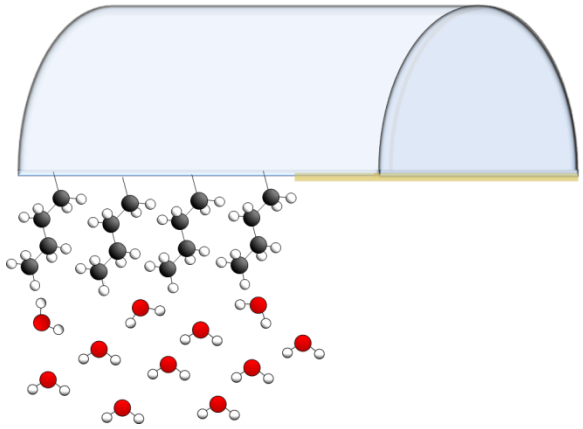

Figure 6.6 Schematic of interfacial water at OTS-modified hemicylindrical prism (4 of 18 carbons explicitly shown) partly coated in gold.

6.5 References

(1) Bruylants, G. Water, Solvent of Life. *Encyclopedia of Astrobiology*; Springer Berlin Heidelberg, 2011; pp 1773–1775.

(2) Pohorille, A.; Pratt, L. R. Is Water the Universal Solvent for Life? *Orig Life Evol Biosph* **2012**, *42*, 405–409.

(3) Deàk, J. C.; Rhea, S. T.; Iwaki, L. K.; Dlott, D. D. Vibrational Energy Relaxation and Spectral Diffusion in Water and Deuterated Water. *J Phys Chem A* **2000**, *104*, 4866–4875.

(4) Lawrence, C. P.; Skinner, J. L. Vibrational Spectroscopy of HOD in Liquid D2O. III. Spectral Diffusion, and Hydrogen- Bonding and Rotational Dynamics. *J. Chem. Phys.* **2003**, *118*, 264.

(5) Asbury, J. B.; Steinel, T.; Stromberg, C.; Corcelli, S. A.; Lawrence, C. P.;

Skinner, J. L.; Fayer, M. D. Water Dynamics: Vibrational Echo Correlation Spectroscopy and Comparison to Molecular Dynamics Simulations. *J Phys Chem A* **2004**, *108*, 1107–1119.

(6) Cowan, M. L.; Bruner, B. D.; Huse, N.; Dwyer, J. R.; Chugh, B.; Nibbering, E. T. J.; Elsaesser, T.; Miller, R. J. D. Ultrafast Memory Loss and Energy Redistribution in the Hydrogen Bond Network of Liquid H2O. *Nature* **2005**, *434*, 199–202.

(7) Eaves, J. D.; Loparo, J. J.; Fecko, C. J.; Roberts, S. T.; Tokmakoff, A.; Geissler, P. L. Hydrogen Bonds in Liquid Water Are Broken Only Fleetingly. *Proc. Natl. Acad. Sci. U.S.A.* **2005**, *102*, 13019–13022.

(8) Auer, B.; Kumar, R.; Schmidt, J. R.; Skinner, J. L. Hydrogen Bonding and Raman, IR, and 2D-IR Spectroscopy of Dilute HOD in Liquid D_2O. *Proc. Natl. Acad. Sci. U.S.A.* **2007**, *104*, 14215–14220.

(9) Kraemer, D.; Cowan, M. L.; Paarmann, A.; Huse, N.; Nibbering, E. T. J.; Elsaesser, T.; Miller, R. J. D. Temperature Dependence of the Two-Dimensional Infrared Spectrum of Liquid H_2O. *Proc. Natl. Acad. Sci.* **2008**, *105*, 437–442.

(10) Paarmann, A.; Hayashi, T.; Mukamel, S.; Miller, R. J. D. Nonlinear Response of Vibrational Excitons: Simulating the Two-Dimensional Infrared Spectrum of Liquid Water. *J. Chem. Phys.* **2009**, *130*, 204110.

(11) Ramasesha, K.; De Marco, L.; Mandal, A.; Tokmakoff, A. Water Vibrations Have Strongly Mixed Intra- and Intermolecular Character. *Nat. Chem.* **2013**, *5*,

935–940.

(12) Rosenfeld, D. E.; Gengeliczki, Z.; Smith, B. J.; Stack, T. D. P.; Fayer, M. D. Structural Dynamics of a Catalytic Monolayer Probed by Ultrafast 2D IR Vibrational Echoes. *Science* **2011**, *334*, 634–639.

(13) Shen, Y. R. *The Principles of Nonlinear Optics*; Wiley-Interscience: New York, 1984.

(14) Boyd, R. W. *Nonlinear Optics*, Third.; Elsevier Inc.: Burlington, 2008.

(15) Moad, A. J.; Simpson, G. J. A Unified Treatment of Selection Rules and Symmetry Relations for Sum-Frequency and Second Harmonic Spectroscopies. *J. Phys. Chem. B* **2004**, *108*, 3548–3562.

(16) Du, Quan; Freysz, Eric, Shen, Y. R. Surface Vibrational Spectroscopic Studies of Hydrogen Bonding and Hydrophobicity. *Science.* **1994**, *264*, 826–828.

(17) Novak, A. Hydrogen Bonding in Solids Correlation of Spectroscopic and Crystallographic Data. *Large Mol.* **1974**, *18*, 177–216.

(18) Raymond, E. A.; Tarbuck, T. L.; Brown, M. G.; Richmond, G. L. Hydrogen-Bonding Interactions at the Vapor/water Interface Investigated by Vibrational Sum-Frequency Spectroscopy of HOD/H_2O/D_2O Mixtures and Molecular Dynamics Simulations. *J. Phys. Chem. B* **2003**, *107*, 546–556.

(19) Sovago, M.; Campen, R.; Wurpel, G.; Müller, M.; Bakker, H. J.; Bonn, M. Vibrational Response of Hydrogen-Bonded Interfacial Water Is Dominated by Intramolecular Coupling. *Phys. Rev. Lett.* **2008**, *100*, 173901.

(20) Myalitsin, A.; Urashima, S.-H.; Nihonyanagi, S.; Yamaguchi, S.; Tahara, T.

Water Structure at the Buried Silica/Aqueous Interface Studied by Heterodyne-Detected Vibrational Sum-Frequency Generation. *J. Phys. Chem. C* **2016**, *120*, 9357–9363.

(21) Schaefer, J.; Backus, E. H. G.; Nagata, Y.; Bonn, M. Both Inter- and Intramolecular Coupling of O−H Groups Determine the Vibrational Response of the Water/Air Interface. *J. Phys. Chem. Lett.* **2016**, *7*, 4591–4595.

(22) Tian, C. S.; Shen, Y. R. Comment on "Vibrational Response of Hydrogen-Bonded Interfacial Water Is Dominated by Intramolecular Coupling." *Phys. Rev. Lett.* **2008**, *101*, 139401.

(23) Gragson, D. E.; McCarty, B. M.; Richmond, G. L. Ordering of Interfacial Water Molecules at the Charged Air/Water Interface Observed by Vibrational Sum Frequency Generation. *J. Am. Chem. Soc.* **1997**, *119*, 6144–6152.

(24) Liu, D.; Ma, G.; Levering, L. M.; Allen, H. C. Vibrational Spectroscopy of Aqueous Sodium Halide Solutions and Air−Liquid Interfaces: Observation of Increased Interfacial Depth. *J. Phys. Chem. B* **2004**, *108*, 2252–2260.

(25) Eftekhari-Bafrooei, A.; Borguet, E. Effect of Electric Fields on the Ultrafast Vibrational Relaxation of Water at a Charged Solid-Liquid Interface as Probed by Vibrational Sum Frequency Generation. *J. Phys. Chem. Lett* **2011**, *2*, 1353–1358.

(26) McGuire, J. A.; Shen, Y. R. Ultrafast Vibrational Dynamics at Water Interfaces. *Science.* **2006**, *313*, 1945–1948.

(27) Eftekhari-Bafrooei, A.; Nihonyanagi, S.; Borguet, E. Spectroscopy and

Dynamics of the Multiple Free OH Species at an Aqueous/Hydrophobic Interface. *J. Phys. Chem. C* **2012**, *116*, 21734–21741.

(28) Xiao, S.; Figge, F.; Stirnemann, G.; Laage, D.; McGuire, J. A. Orientational Dynamics of Water at an Extended Hydrophobic Interface. *J. Am. Chem. Soc* **2016**, *138*, 5551–5560.

(29) Stirnemann, G.; Rossky, P. J.; Hynes, J. T.; Laage, D. Water Reorientation, Hydrogen-Bond Dynamics and 2D-IR Spectroscopy next to an Extended Hydrophobic Surface. *Faraday Discuss.* **2010**, *146*, 263–281.

(30) Nihonyanagi, S.; Yamaguchi, S.; Tahara, T. Ultrafast Dynamics at Water Interfaces Studied by Vibrational Sum Frequency Generation Spectroscopy. *Chem. Rev.* 10.1021/acs.chemrev.6b00728.

(31) Hsieh, C. S.; Okuno, M.; Hunger, J.; Backus, E. H. G.; Nagata, Y.; Bonn, M. Aqueous Heterogeneity at the Air/water Interface Revealed by 2D-HD-SFG Spectroscopy. *Angew. Chemie - Int. Ed.* **2014**, *53*, 8146–8149.

(32) Vanselous, H.; Stingel, A. M.; Petersen, P. B. Interferometric 2D Sum Frequency Generation Spectroscopy Reveals Structural Heterogeneity of Catalytic Monolayers on Transparent Materials. *J. Phys. Chem. Lett.* **2017**, *8*, 825–830.

(33) Cervetto, V.; Helbing, J.; Bredenbeck, J.; Hamm, P. Double-Resonance versus Pulsed Fourier Transform Two-Dimensional Infrared Spectroscopy: An Experimental and Theoretical Comparison. *J. Chem. Phys.* **2004**, *121*, 5935–5942.

(34) Shim, S.-H.; Strasfeld, D. B.; Ling, Y. L.; Zanni, M. T. Automated 2D IR Spectroscopy Using a Mid-IR Pulse Shaper and Application of This Technology to the Human Islet Amyloid Polypeptide. *Proc. Natl. Acad. Sci.* **2007**, *104*, 14197–14202.

(35) Shim, S.-H.; Zanni, M. T. How to Turn Your Pump-Probe Instrument into a Multidimensional Spectrometer: 2D IR and Vis Spectroscopies via Pulse Shaping. *Phys. Chem. Chem. Phys.* **2009**, *11*, 748–761.

(36) Barrett, A.; Petersen, P. B. Order of Dry and Wet Mixed-Length Self-Assembled Monolayers. *J. Phys. Chem. C* **2015**, *119*, 23943–23950.

(37) Vanselous, H.; Petersen, P. B. Extending the Capabilities of Heterodyne-Detected Sum-Frequency Generation Spectroscopy : Probing Any Interface in Any Polarization Combination. *J. Phys. Chem. C* **2016**, *120*, 8175–8184.

(38) Shen, Y. R. Phase-Sensitive Sum-Frequency Spectroscopy. *Annu. Rev. Phys. Chem.* **2013**, *64* 129–150.

(39) Nihonyanagi, S.; Mondal, J. A; Yamaguchi, S.; Tahara, T. Structure and Dynamics of Interfacial Water Studied by Heterodyne-Detected Vibrational Sum-Frequency Generation. *Annu. Rev. Phys. Chem.* **2013**, *64*, 579–603.

(40) Ye, S.; Nihonyanagi, S.; Uosaki, K. Sum Frequency Generation (SFG) Study of the pH-Dependent Water Structure on a Fused Quartz Surface Modified by an Octadecyltrichlorosilane (OTS) Monolayer. *Phys. Chem. Chem. Phys.* **2001**, *3*, 3463–3469.

(41) Tyrode, E.; Liljeblad, J. F. D. Water Structure next to Ordered and Disordered

Hydrophobic Silane Monolayers: A Vibrational Sum Frequency Spectroscopy Study. *J. Phys. Chem. C* **2013**, *117*, 1780–1790.

(42) Auer, B. M.; Skinner, J. L. IR and Raman Spectra of Liquid Water: Theory and Interpretation. *J. Chem. Phys.* **2008**, *128*, 224511.

(43) Ni, Y.; Gruenbaum, S. M.; Skinner, J. L. Slow Hydrogen-Bond Switching Dynamics at the Water Surface Revealed by Theoretical Two-Dimensional Sum-Frequency Spectroscopy. *Proc. Natl. Acad. Sci.* **2013**, *110*, 1992–1998.

CHAPTER 7

CONCLUSIONS AND FUTURE DIRECTIONS

7.1 General Summary

Through the development of advanced ultrafast vibrational experiments, the molecular level picture of the catalyst-semiconductor interface has been explored. We have found that the CO_2 reduction catalyst has distinctly different structural and dynamic properties when immobilized on single crystal TiO_2 surfaces as compared to TiO_2 nanoparticles. With the push towards high-surface-area single-crystal structures with controlled facets in many applications, it is increasingly important to understand how these different surface environments alter the molecular properties including the electronic structure, and hence, catalytic activity, of these systems. The metal-carbonyl vibrational modes explored in this dissertation are sensitive probes to the local electronic environment.

Achieving the goal of studying vibrational dynamics and couplings at condensed phase interfaces required a number of different experimental advances. First, heterodyne-detection (HD) was needed to extract purely absorptive spectra and provide information on molecular orientation. While a number of research groups have explored various experimental geometries, our approach built around high phase stability through, in part, the use of common optics between local oscillator generating crystal and sample has provided the first HD SFG spectrum of a buried solvated

monolayer and demonstrated the ability to probe the buried surface in any polarization combination. Water molecules were found to cause an increased degree of disorder in the self-assembled hydrophobic monolayer that was studied.

By combining HD and two interfering excitation pulses, we developed interferometric 2D SFG spectroscopy with an external oscillator. Armed with this method, we were able to acquire the first 2D SFG spectrum of molecules at the surface of a transparent material. We studied the vibrational relaxation and spectral diffusion of $Re(CO)_3$ on nanocrystalline TiO_2 and found a static structural heterogeneity, indicative of multiple different binding geometries on the nanoparticle surface. An extended 2D SFG study of the same catalyst on TiO_2 rutile and anatase single crystal surfaces revealed an entirely different coupling environment and a more ordered, homogeneous system. These results reveal that molecules on single crystal surfaces behave significantly differently than on nanocrystalline surfaces in terms of intra and intermolecular vibrational coupling, vibrational relaxation, and molecular orientation. Therefore, device performance for future CO_2 reduction systems which may be based around high surface area single crystal devices cannot be gleaned from the nanocrystalline system.

The buried water-hydrophobic monolayer interface was also studied with 2D SFG. Preliminary data of this particularly challenging system is consistent with a strongly hydrogen-bonded network with very fast vibrational relaxation, in constrast with the water-air interface which has slower relaxation at the interface than is seen in the bulk. The ability to study this and other biologically relevant interfaces, such as

protein folding in which water molecules are displaced, is an important advancement for the future of the field of SFG.

7.2 Future Directions

7.2.1 Buried TiO_2 Surfaces

With these complex experiments, increasingly difficult to study samples can be further explored. For instance, CO_2 reduction occurs not at a dry surface, but at a TiO_2 – solvent interface. However, probing the buried solvated interface would require transmission of the laser beams through the TiO_2 substrate, which is birefringent. A good starting point would be studying the buried sensitized nanoparticle – solvent interface, at which the transparent TiO_2 nanoparticles can be deposited in a thin layer through spin coating. The presence of solvent and electrolytes will likely have an influence on the vibrational dynamics. For the case of dye-sensitized solar cells, which are structurally similar to the CO_2 reduction catalyst, the presence and composition of electrolyte was found to significantly slow charge injection, to the point of being rate limiting.[1] Through the interfacial specificity, SFG spectroscopy can uniquely probe the molecules at the solvated interface to determine how the solvent and electrolyte alter the molecular catalyst, and thereby determine the influence of the electrolyte on the reaction dynamics.

7.2.2 Visible Excitation

The CO_2 reduction system is, of course, initiated through excitation either photochemically or electrochemically. Therefore, a visible excitation pulse could be used to study the chemical reaction *in situ*. This experiment would involve utilizing the third output from the amplifier, and diverting it to a tunable visible OPA that we already possess. This would be similar to IR pump – SFG probe experiments, except the pump would be a tunable visible pulse that could be on resonance with the electronic transition. Thus, vibrational dynamics of the metal carbonyl, which are highly sensitive to the oxidation state of the metal, can be observed in the electronic ground and excited state. Furthermore, moving electrons generate a broad response in the mid-infrared region[2], potentially providing a signature of electron injection into the semiconductor in the SFG spectrum.

7.2.3 2D of Water at Complex Interfaces

The 2D SFG results presented in Chapter 6 were of pure H_2O at a condensed phase hydrophobic interface. The spectral features provided a different picture of water when compared to previous studies of the water-air interface, which were performed in the scanning narrowband IR pump – SFG probe geometry. It would be interesting to compare these results with our experimental method that contains higher temporal resolution through an interfering pump-pulse pair. Additionally, isotopic dilution studies of bulk water and the water-air interface have revealed both inter and intramolecular couplings. Studying the 2D SFG spectrum of HOD in D_2O and H_2O, in

which intramolecular pathways would be suppressed, would be an informative extension of the work presented in Chapter 6. The experimental design can further be applied to mixed hydrophilic and hydrophobic interfaces, which would mimic complex biological surface.

7.2.4 Biological Systems

Through collaboration with professors Georges Belfort, Mihail Barboiu, and Marc Baaden, we have recently used SFG to study the water structure in transmembrane water transport channels. These channels are believed to self-assemble into a macroscopically chiral structure.[3] We found that the water molecules inside the channel also adopt a chiral structure through polarization controlled SFG experiments that selectively probe chirality. Three channels were studied: S-HC8 (chiral channels), HC8 (achiral channels), and pure phosphatidylcholine/phosphatidylserine (PC/PS) lipid bilayer. The homodyne data collected is shown in Figure 7.1. A manuscript pertaining to these results is currently in preparation.

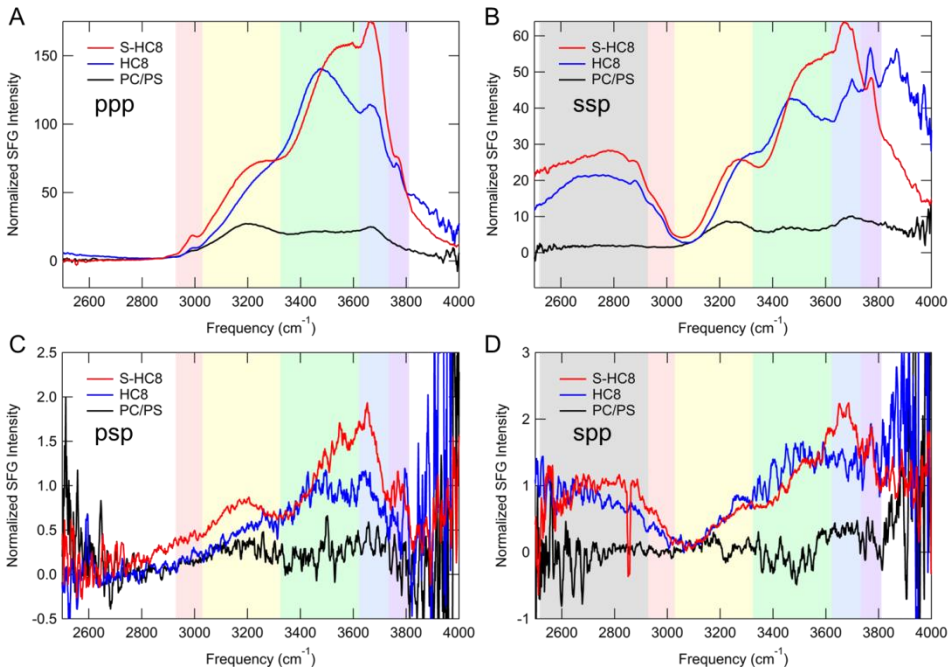

Figure 7.1 Homodyne-detected SFG spectra collected under different polarization conditions (polarization of SFG, visible, and IR pulses, respectively). Pure achiral responses are in A) *ppp* or B) *ssp*, while pure chiral responses are in C) *psp* and D) *spp* polarization combinations.

As discussed in Chapter 6, the cause of discrete features in the water SFG spectrum around 3200 and 3400 cm^{-1} has been debated. For the water-bilayer interface, the two features could be due to the same couplings or Fermi-resonance or could be due to specific sub-populations of bulk-like water molecules oriented in the field of the charged headgroups, and water molecules directly interacting with the lipid headgroups and membrane, respectively. Irrespective of the nature of the two distinct features, the overall distribution of vibrational frequencies and width of the bands reflect the breadth of hydrogen-bonding interactions at the water-bilayer interface. In

addition to these two bands, we observe a band at 3650 cm^{-1} (blue) that has previously been attributed to weakly hydrogen-bonded water molecules interacting with the ester carbonyl groups of the lipid.

For both samples with the artificial channels inserted into the supported lipid bilayer, we observe a large increase in the SFG intensity across the whole spectral region. In particular, the 3450 cm^{-1} band increases, which is consistent with chain-like water molecules inside the channel. In addition to three bands observed for the bilayer, we observed an additional sharp feature at 3750 cm^{-1} (violet) in both *ppp* and *ssp*. This sharp feature is due to a non-hydrogen-bonded OH group, attributed to a sub-populations of the water molecules inside the channel. Furthermore, we observe a broad feature at 2800 cm^{-1} in *ssp* but not in *ppp*. This feature we attribute to the NH_2 groups of the imidazole hydrogen-bonded to the carboxylate headgroups of the lipid giving rise to a very strong hydrogen bond. That the feature is observed in *ssp* but not *ppp* validates that the channels are highly ordered in the direction perpendicular to the lipid bilayer. Overall, the very large increase in the SFG intensity across the OH spectral region confirms that the insertion of the channels do not disrupt the order of the bilayer but rather prove that the hydrogen-bonded structure of the water molecules structure inside the channels is highly orientated with a strong dipolar alignment

Attempts to fit the this data to a sum of Lorentzian functions, thereby extracting out the absorptive lineshape, as is typically performed on SFG data, failed due to inhomogeneous broadening in this particular system. Therefore, these complex inhomogeneous aqueous systems, which exist in nearly all biological environments,

would greatly benefit from heterodyne-detection allowing fitting with an arbitrary line-shape function, while homodyne-detection assumes discrete Lorentzian lineshapes. The experimental advances for HD, presented in Chapter 3, allow this experiment to be performed at the buried interface in each of these polarization combinations and more generally opens up this technique to probing highly complex environments.

7.3 References

(1) Listorti, A.; O'Regan, B.; Durrant, J. R. Electron Transfer Dynamics in Dye-Sensitized Solar Cells. *Chem. Mater.* **2011**, *23*, 3381–3399.

(2) Anderson, N. A.; Lian, T. Ultrafast Electron Injection from Metal Polypyridyl Complexes to Metal-Oxide Nanocrystalline Thin Films. *Coord. Chem. Rev.* **2004**, *248*, 1231–1246.

(3) Licsandru, E.; Kocsis, I.; Shen, Y.-X.; Murail, S.; Legrand, Y.-M.; van der Lee, A.; Tsai, D.; Baaden, M.; Kumar, M.; Barboiu, M. Salt-Excluding Artificial Water Channels Exhibiting Enhanced Dipolar Water and Proton Translocation. *J. Am. Chem. Soc* **2016**, *138*, 5403–5409.